2023

Knowledge discovery on the integrative analysis of electrical and mechanical dyssynchrony to improve cardiac resynchronization therapy

Zhuo He
Michigan Technological University, zhuoh@mtu.edu

KNOWLEDGE DISCOVERY ON THE INTEGRATIVE ANALYSIS OF ELECTRICAL AND MECHANICAL DYSSYNCHRONY TO IMPROVE CARDIAC RESYNCHRONIZATION THERAPY

By

Zhuo He

A DISSERTATION

Submitted in partial fulfillment of the requirements for the degree of

DOCTOR OF PHILOSOPHY

In Computational Science and Engineering

MICHIGAN TECHNOLOGICAL UNIVERSITY

2023

This dissertation has been approved in partial fulfillment of the requirements for the Degree of DOCTOR OF PHILOSOPHY in Computational Science and Engineering.

Department of Applied Computing

Dissertation Advisor:	*Dr. Weihua Zhou*
Committee Member:	*Dr. Guy C. Hembroff*
Committee Member:	*Dr. Jinshan Tang*
Committee Member:	*Dr. Qinghui Chen*
Department Chair:	*Dr. Daniel R. Fuhrmann*

Contents

List of Figures

List of Tables

Preface

Some chapters of this dissertation contain published material. The following list indicates which publications work, were used along with notes on author contributions.

Chapter 1

He Z, Garcia EV, Zhou W*. Chapter 25 – Nuclear imaging guiding cardiac resynchronization therapy in *Nuclear Cardiology: Basic and Advanced Concepts in Clinical Practice*. Springer-Nature. Book chapter. 2021. https://dio:10.1007/978-3-030-62195-7

He Z is the leading researcher in this work. The research was performed under the guidance of Zhou W, and the ideas proposed in the paper stemmed from conversations among all authors. See Appendix A for a copy of the copyright transfer agreement.

Chapter 2

He Z, Fernandes FA, Nascimenta EA, Garcia EV, Mesquita CT, Zhou W. Incremental value of left ventricular shape parameters measured by gated SPECT MPI in predicting CRT super-responders. *Journal of Nuclear Cardiology.* 2021 Jan 27.

He Z is the leading researcher in this work. The research was performed under the guidance of Zhou W, and the ideas proposed in the paper stemmed from conversations among all authors. See Appendix A for a copy of the copyright transfer agreement.

He Z, Li D, Cui C, Qin HY, Zhao Z, Hou X, Zou J, Chen ML, Wang C, Zhou W. Predictive values of left ventricular mechanical dyssynchrony for CRT response in heart failure patients with different pathophysiology. *Journal of Nuclear Cardiology.* 2021 Sep 17:1-2.

He Z is the leading researcher in this work. The research was performed under the guidance of Zhou W, and the ideas proposed in the paper stemmed from conversations among all authors. See Appendix A for a copy of the copyright transfer agreement.

Chapter 3

He Z, Zhang X, Zhao C, Ling X, Qian Z, Wang Y, Hou X, Zou J, Zhou W. A method using deep learning to discover new predictors from left-ventricular mechanical dyssynchrony for CRT response. *Journal of Nuclear Cardiology.* 2022 Aug 1:1-2

He Z is the leading researcher in this work. The research was performed under the guidance of Zhou W, and the ideas proposed in the paper stemmed from conversations among all authors. See Appendix A for a copy of the copyright transfer agreement.

Chapter 4

He Z, Si H, Zhang X, Chen QH, Zou J, Zhou W. A new method using deep transfer learning on ECG to predict the response to cardiac resynchronization therapy. *arXiv preprint* arXiv:2306.01210. 2023 Jun 2.

He Z is the leading researcher in this work. The research was performed under the guidance of Zhou W, and the ideas proposed in the paper stemmed from conversations among all authors. This research, currently under review, has also been made available on the arXiv website, an open-access preprint platform.

Acknowledgments

I am grateful for the opportunity to express my deepest appreciation to those who have helped me in achieving this significant milestone.

First and foremost, I want to thank my dissertation committee chair and advisor, Dr. Weihua Zhou, for providing me with invaluable guidance, feedback, and support throughout my doctoral journey. Your expertise, patience, and encouragement have been instrumental in helping me reach this point. I would also like to express my sincere gratitude to the members of my dissertation committee, Dr. Guy C. Hembroff, Dr. Jinshan Tang, and Dr. Qinghui Chen, for their critical feedback and valuable insights that have helped me refine my research and complete this work.

I am thankful for my family and friends who have supported me in numerous ways throughout this journey. I especially thank Wei, Yuwen, Liange, Fangyao, Yi, Dongyan, Dr. Peng, Li, Tianya, Qingwei, Yiyang, Samantha, Wenli whose unwavering support, encouragement, and sacrifices have made this achievement possible.

I extend my appreciation to my colleagues, collaborators, and mentors, especially Chen, Haipeng, Dr. Joe Zhang, who have provided me with invaluable assistance, insights, and encouragement along the way. Your contributions have enriched my research and inspired me to pursue new avenues of inquiry.

Finally, I would like to express my gratitude to the Graduate School, College of Computing Department and Computational Science and Engineering program that provided me with the resources and support to pursue this degree. I will always cherish the experiences and opportunities that this program has offered me.

List of Abbreviations

This provides information on how to write your MS thesis or PhD dissertation using the LaTeX document preparation system in compliance with Michigan Technological University Graduate School requirements.

AAMI	Association for the Advancement of Medical Instrumentation
AE	Autoencoder
AP	Accessory pathway
AUC	Area under curve
CAD	Coronary artery disease
CNN	Convolutional neural network
CRT	Cardiac resynchronization therapy
CT	Computational tomography
DCM	Dilated cardiomyopathy
DNN	Deep neural network
EAM	Electroanatomic mapping
ECG	Electrocardiograms
EDE	End-diastolic eccentricity
ECTb2	Emory Reconstruction Toolbox
ECTb4	Emory Cardiac Toolbox v4

EDVi	End-diastolic volume index
ERToolbox	Emory reconstruction toolbox
ESE	End-systolic eccentricity
ESVi	End-systolic volume Index
HF	Heart failure
ICD	Implantable cardioverter defibrillator
ICM	Ischemic cardiomyopathy
LBBB	Left bundle-branch block
LV	Left ventricular
LVEF	Left ventricular ejection fraction
LVEDV	Left ventricular end-diastolic volume
LVESV	Left ventricular end-systolic volume
LVDD	Left ventricular diastolic dyssynchrony
LVSD	Left ventricular systolic dyssynchrony
MACE	Major advense cardiac events
MLHFQ	Minnesota Living with Heart Failure Questionnaire
MRI	Magnetic resonance imaging
MPI	Myocardial perfusion imaging
MSE	Mean squared error
NHANES	National Health and Nutrition Examination Survey
NYHA	New York Heart Association

PE	Phase entropy
PBW	Phase histogram bandwidth
PSD	Phase standard deviation
OSEM	Ordered subset expectation maximization
ResNet	Residual neural network
RF	Random forest
RL	Reinforcement learning
ROC	Receiver operator characteristic
RV	Right ventricular
SPECT	Single-photon emission computed tomography
STFT	Short-time Fourier transform
SVM	Support vector machine
VCG	Vectorcardiography

Abstract

Cardiac resynchronization therapy (CRT) is a standard method of treating heart failure by coordinating the function of the left and right ventricles. However, up to 40% of CRT recipients do not experience clinical symptoms or cardiac function improvements. The main reasons for CRT non-response include: (1) suboptimal patient selection based on electrical dyssynchrony measured by electrocardiogram (ECG) in current guidelines; (2) mechanical dyssynchrony has been shown to be effective but has not been fully explored; and (3) inappropriate placement of the CRT left ventricular (LV) lead in a significant number of patients.

In terms of mechanical dyssynchrony, we utilize an autoencoder to extract new predictive features from nuclear medicine images, characterizing local mechanical dyssynchrony and improving the CRT response rate. Although machine learning can identify complex patterns and make accurate predictions from large datasets, the low interpretability of these "black box" methods makes it difficult to integrate them with clinical decisions made by physicians in the healthcare setting. Therefore, we use visualization techniques to enable physicians to understand the physical meaning of new features and the reasoning behind the clinical decisions made by the artificial intelligent model.

For electrical dyssynchrony, we use short-time Fourier transform (STFT) to transform one-dimensional waveforms into two-dimensional frequency-time spectra. And transfer learning is used to leverage the knowledge learned from a large arrhythmia ECG dataset of related medical conditions to improve patient selection for CRT with limited data. This improves prediction accuracy, reduces the time and resources required, and potentially leads to better patient outcomes. Furthermore, an innovative approach is proposed for using three-dimensional spatial VCG information to describe the characteristics of electrical dyssynchrony, locate the latest activation site, and combine it with the latest mechanical contraction site to select the optimal LV lead position.

In addition, we apply deep reinforcement learning to the decision-making problem of CRT patients. We investigate discrete state space/specific action space models to find the best treatment strategy, improve the reward equation based on the physician's experience, and learn the approximation of the best action-value function that can improve the treatment policy used by clinicians and provide interpretability.

Chapter 1

Introduction

About 6.2 million adults in the US have heart failure (HF), and the prevalence of HF will increase by 46% from 2012 to 2030 [5, 6]. Despite the fact that survival after the onset of HF in older adults has improved, HF was the underlying cause of 83,616 deaths in 2018 [7]. The total cost for HR was estimated to be $30.7 billion in 2012 [6]. Cardiac resynchronization therapy (CRT) is a well-established treatment for HF in patients with left ventricular (LV) systolic dysfunction and evidence of cardiac dyssynchrony [8].

Cardiac resynchronization therapy can be achieved by LV stimulation through a lead within a tributary of the coronary sinus. The cardiologist guides the lead into the correct chamber of the heart and checks its position under fluoroscopy guidance. The

lead is then connected to the CRT monitor on the surface of the chest. The appropriate electrical energy and pacing timing are then tested [9]. A CRT positive response includes the alleviation of HF symptoms, improvement of LV function, decreases in hospitalization and morbidity, and increases of exercise capability and quality of life score [9].

However, 30-40% of the CRT patients did not respond to CRT with an improved clinical symptom (assessed by NYHA class, quality-of-life score, and 6-minute walk distance) and/or cardiac function (assessed by LV end-systolic volume [LVESV], LV end-diastolic volume [LVEDV] and left ventricular ejection fraction [LVEF]) [10, 11, 12, 13, 14]. The main reasons for CRT non-response were reviewed in [9, 15, 16] and included: (1) The selection of patients based on electrical dyssynchrony is not optimal; mechanical dyssynchrony is also important. (2) The presence of extensive LV scar tissue (irrespective of the location) may hamper response to CRT [17, 18]. (3) The CRT LV lead may not be placed in an appropriate position in a significant number of patients; pacing at the latest viable contracting site is essential [19, 20, 21].

In this work, we developed novel and clinically interpretable algorithms for knowledge discovery from mechanical dyssynchrony and electrical dyssynchrony for CRT patient selection. This includes the development of novel algorithms for feature extraction and description, evaluation of the algorithms using real-world data sets, and comparison of performance with the clinical guidelines and existing state-of-the-art algorithms.

1.1 Motivation

Motivation in this research endeavor is determined by three critical points. First, the existing clinical guidelines are not effective enough to select patients based on clinical records and electrocardiograms(ECG) alone, and 30-40% of patients who have a pacemaker installed through thoracotomy do not get the corresponding therapeutic benefit. We see an opportunity to reduce patient suffering and reduce healthcare costs. Second, current advances in computing technologies such as computer vision, multi-modality fusion, and data interpretation permit the opportunity to achieve tangible solutions. Third, most machine learning solutions for patient selection are "black boxes", for example, deep learning. In many practical applications, especially in the medical field as an aid tool, it is imperative to have a reasonable explanation that can be understood by physicians; this may include providing information such as what was learned, what is the value of individual sources, why a decision was made, what evidence process was used, and what confidence the system had in its decision. This work introduces methods that help answer these questions, as well as visualizations that help physicians better understand machine learning solutions and their behavior on different data instances.

1.2 Background

1.2.1 Introduction to CRT

1.2.1.1 Heart Failure

As the population ages, the prevalence of heart failure (HF) continues to rise. Over 6 million Americans $\geq$ 20 years of age (2.2%) had heart failure, according to the National Health and Nutrition Examination Survey (NHANES) data from 2013 to 2016. It is worth noting that 5.7 million people had heart failure between 2009 and 2012 [5]. Moreover, it will increase 46% from 2012 to 2030, which means there will be more than 8 million people $\geq$ 18 years of age with HF [5]. From 2004 to 2014, the number of hospital discharges for HF decreased from 1,042,000 to 900,000 [5]. In 2015, there were 2,671,000 physician office visits, and 481,000 emergency room visits due to the HF [5].

Even though the survival in older adults with HF has improved [22], the overall 1-year case-fatality rate after hospitalization for HF remains as high as 22% [**?**]. Compared with 2005 (58,933), the number of the underlying cause of deaths attributable to HF increased by 27.7% in 2015 (75,251) [5]. In 2015, the overall any-mention age-adjusted

death rate for HF was 87.9 per 100,000 [5]. The cost of HF was estimated to be $30.7 billion in 2012, and it will increase to $69.8 billion by 2030 [6].

The cost of treating HF comorbidities and exacerbations in youths totals nearly $1 billion in inpatient costs and maybe rise [16]. The associated cost burden of HF is anticipated to constitute a large portion of total pediatric healthcare costs.

1.2.1.2 What is CRT

Cardiac resynchronization therapy (CRT) is a standard treatment for HF by coordinating the function of the left and right ventricles [23]. The inclusion criteria for CRT have been continually improving. For now, CRT is indicated for patients who have a low LVEF (typically $\geq 35\%$), sinus rhythm, left bundle-branch block (LBBB) pattern, QRS duration $\geq 150ms$ on ECG and New York Heart Association (NYHA) class II, NYHA class III and ambulatory IV symptoms on Guideline Determined Medical Therapy [24, 25].

During the installation of CRT, the doctor installs a pulse generator under the skin of the collarbone and connects it to the insulated wire (lead or electrode) inserted from the subclavian vein, armpit, or cephalic vein. Under the guidance of fluoroscopy, the cardiologist secures each lead to the correct chamber of the heart and appropriate position.

CRT defibrillators (CRT-D) can also terminate dangerously fast heart, life-threatening rhythms, which integrates the function of an implantable cardioverter-defibrillator (ICD). CRT and CRT-D have become increasingly extensive treatment options for HF patients [26].

1.2.1.3 How to evaluate CRT outcomes?

The effectiveness of CRT has been widely demonstrated in many clinical trials [27, 28, 29, 30]. The CRT positive outcomes include improved LV functions, HF symptoms, increased exercise capability and quality of life score, fewer HF hospitalizations, and lower mortality rates [9, 31].

However, $30-40\%$ of the patients, who meet the standard indications, did not show any benefit after CRT installation with an improvement of clinical symptoms (NYHA class, quality of life score, and 6-min walk distance) and/or cardiac function (LVESV, LVEDV, and LVEF)[9].

The reasons for the presence of 'non-responders' are shown below: [9, 15, 32]: (1) The selection of CRT patients relies on only 3 ECG parameters, QRS duration, LBBB, and sinus rhythm, which is not optimal. The QRS duration is less important than mechanical dyssynchrony, which is critical to the CRT response [33, 34, 35]. Also, the left ventricles without mechanical dyssynchrony will not respond and often deteriorate

following CRT [9, 36, 37] (2) A higher overall LV scar burden may also obstruct the response to CRT, particularly transmural scar [18, 38, 39]. (3) Moreover, it is crucial for CRT response that the LV lead should be placed away from the scar area [18, 39, 40] and at or close to the site with the latest activation [41, 42, 43]. (4) During the CRT implantation, guidance is necessary on fluoroscopy venograms to navigate the LV lead to the optimal position. Because even if the implanters knew the accurate latest activating viable site before CRT implantation, it is hard to place the LV lead in the optimal site without the navigation by a coregistration between myocardial images and fluoroscopy venograms [44, 45].

1.2.2 Nuclear imaging to guide CRT

1.2.2.1 Myocardial imaging techniques

Myocardial imaging techniques, including echocardiography, computational tomography (CT), magnetic resonance imaging (MRI), and nuclear imaging, play an important role in improving patient selection and LV lead placement for CRT by detecting scar and the latest activated segment[44, 46, 47].

† **Echocardiography**

Several studies have shown that the dyssynchrony predictors from echocardiography have the potential to guide CRT patient selection [12, 48, 49, 50, 51**?**]and lead position [20, 44, 47, 49, 52]. The TARGET study, a prospective randomized controlled clinical trial, showed a significant improvement in CRT response, clinical status, and lower rates of combined death and heart failure-related hospitalization under the guidance of placing the LV lead to the latest activated segment and away from the scar [44]. However, two prospective multicenter studies (PROMISE-CRT [53] and PROSPECT [27]) showed a modest predictive accuracy for CRT patient selection by any single echocardiographic predictor. Echocardiography is widely available, easy to use, relatively low cost, and away from ionizing radiation or nephrotoxicity [54]. However, it has high inter-operator variability, which is the major limitation of echo-guided CRT and one of the main reasons for the modest accuracy in predicting CRT response in the PROSPECT trial [27].

† **CT**

Computational tomography (CT) can evaluate LV dyssynchrony [55], visualize the coronary veins [56], and detect scar location and burden [57], which can be used to guide left ventricular lead placement in CRT [38, 58]. The prospective DIRECT study showed that the CT-driven dyssynchrony metrics and regional mechanical contraction analysis had the potential to predict 2-year major adverse cardiac events, but not 6-month CRT response [55]. However, the

current single-energy source CT scanners cannot accurately depict extracellular myocardial fibrosis through late contrast enhancement [38]. In a prospective study, using pre-implant dual-source CT in 54 patients scheduled for CRT, Truong et al.[55] measured time-to-maximal wall thickness and inward motion to determine 1) CT global and segmental dyssynchrony and 2) concordance of the lead location to regional LV mechanical contraction; they demonstrated that the wall motion dyssynchrony parameters of both global and opposing anteroseptal-inferolateral walls predicted 2-year major adverse cardiac events (MACE), and LV lead location concordant to regions of maximal wall thickness was associated with less MACE. Due to the small sample size and MACE rate, the results should be explained with caution [55]. Nevertheless, dual-source CT has not been widely used, and the number of studies is very limited.

† **MRI**

Cardiac magnetic resonance imaging has the unique advantage of its ability to accurately and reproducible measure LV function [59, 60], measure myocardial viability [61], and assess mechanical dyssynchrony [62]. Thus cardiac MRI can be an alternative technique for the noninvasive evaluation of LV function and dyssynchrony [54]. However, MRI has security risks for patients with devices, and it is time-consuming and involves significant user interaction [9, 63].

1.2.2.2 Nuclear imaging for guiding CRT

Nuclear imaging is a unique technique for evaluating LV functions, dyssynchrony, and site with the latest contraction due to its ability to characterize myocardial perfusion and mechanical dyssynchrony with high repeatability and reproducibility. Nuclear imaging techniques have great potential in guiding CRT patient selection and LV lead placement. The widespread use of nuclear imaging and its high reproducibility makes it a more attractive approach [9].

Nuclear imaging to detect myocardial viability

Both ^{201}thallium chloride and ^{99}technetium-labeled SPECT tracers have been used to measure myocardial viability in single-photon emission-computed tomography (SPECT). Scar tissue is defined by 50–60% tracer uptake at rest as a threshold for myocardial viability [54].

Studies have found that LV scar burden and location provided by SPECT-MPI have essential predictive values in predicting CRT response [18, 42]. A study showed that a higher scar burden quantified by technetium (^{99m}Tc) tetrofosmin SPECT-MPI negatively impacted CRT response and might inhibit the CRT response in the LV lead region [64]. Adelstein et al.[65] found that in long-term follow-up ischemic cardiomyopathy (ICM) patients with lower scar burden detected by rest–redistribution Tl^{201}

experienced similar positive clinical and LV functional outcomes after CRT. However, Xu et al. [66] found that the mismatch between scar region and LV pacing position could not predict a negative response to CRT; it is worth noting that the lack of association might be due to the small number (n=17) of patients who had poor concordance between LV lead position and scar. A study of CRT recipients with ICM showed that the concordance between LV lead location and scar region or reversible ischemia was an independent predictor of HF hospitalizations and all-cause mortality [67]. Also, Ypenburg et al. [64]found that even if the LV lead was placed in a transmural scar region (¡50% tracer uptake by SPECT with ^{99m}Tc tetrofosmin) with the latest mechanical activation, it would deteriorate CRT response. The main limitation of SPECT-MPI is the low spatial resolution, which may lead to the loss of information or, conversely, overestimation of scarring in thin-walled dilated hearts [54, 68].

Compared with SPECT-MPI, PET has a higher spatial resolution and can more accurately estimate nonviable myocardium with considerable sensitivity and dynamic-imaging capabilities, which has been suggested as a suitable option for LV viability and dyssynchrony measurement [68, 69]. Positron Emission Tomography ^{18}Fluorine-deoxyglucose (^{18}FDG) is a glucose analog and reflects cardiac glucose utilization, which is commonly used as a tracer to assess the viability of myocardium [9].

Lehner et al. [70] found that there was a significantly lower scar burden in positive

CRT responders than in non-responders at 6-month follow-up by ^{18}FDG-PET and echocardiography. Uebleis et al. [71] integrated the gated ^{18}FDG-PET and CT imaging to improve the detection of scar and dyssynchrony, which demonstrated that the global scar burden and the LV pacing site were critical factors referred for predicting CRT response.

Nuclear imaging to detect mechanical dyssynchrony

The phase analysis technique has been well established to measure LV mechanical dyssynchrony from ECG-gated SPECT/PET MPI [72]. First, the gated short-axis slices are reconstructed and reoriented from planar studies. Second, the three-dimensional maximal-count myocardial perfusion distribution is extracted from the short-axis slices by the sampling of the myocardial wall. Third, all the samples are input into the phase analysis algorithm: the LV systolic dyssynchrony (LVSD) phase angles are calculated by the 1-harmonic Fourier approximation, and LV diastolic dyssynchrony (LVDD) phase angles are calculated by the 3-harmonic Fourier approximation. The Fourier approximation measures the change of counts in the left ventricular myocardium throughout 8 or 16 frames in a cardiac cycle; the resulting phase angles start with 0° corresponding to the peak of the R wave and stop at 360° corresponding to one R-R interval, as shown in Figure 1. Finally, the polar map of the LV phase is generated based on the 3D phase angle distribution in the LV myocardium [72, 73].

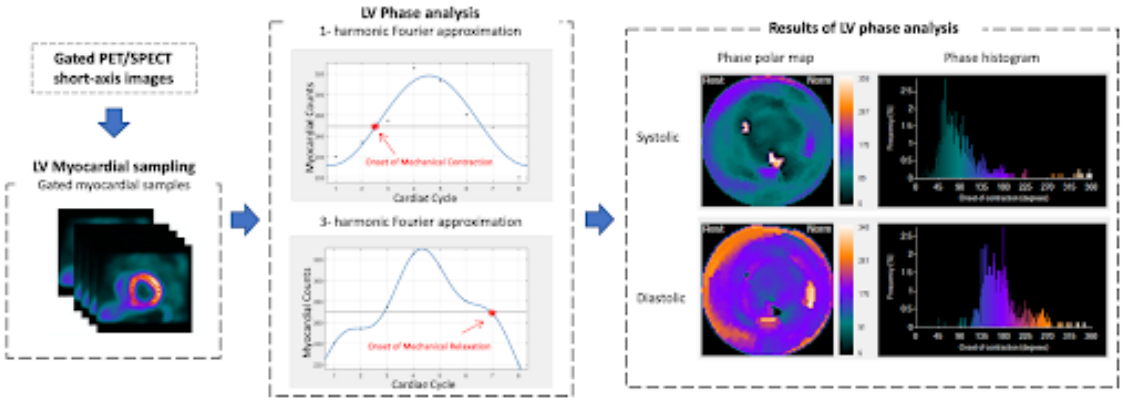

Figure 1.1: Processing steps of the 1-harmonic and 3-harmonic phase analysis to measure the LV systolic and diastolic dyssynchrony. The input is gated PET/SPECT short-axis images. First, the myocardial wall is sampled by detecting the regional maximal count in each slice. The myocardial count curves for each region are approximated by the 1-harmonic function for systolic dyssynchrony and the 3-harmonic function for diastolic dyssynchrony. The phase angles of the systolic and diastolic approximation represent the onset of mechanical contraction and the onset of mechanical relaxation, respectively. Then the systolic and diastolic phase polar map and phase histogram are generated.

Figure 1.1 Processing steps of the 1-harmonic and 3-harmonic phase analysis to measure the LV systolic and diastolic dyssynchrony. The input is gated PET/SPECT short-axis images. First, the myocardial wall is sampled by detecting the regional maximal count in each slice. The myocardial count curves for each region are approximated by the 1-harmonic function for systolic dyssynchrony and the 3-harmonic function for diastolic dyssynchrony. The phase angles of the systolic and diastolic approximation represent the onset of mechanical contraction and the onset of mechanical relaxation, respectively. Then the systolic and diastolic phase polar map and phase histogram are generated.

The phase analysis algorithm is a fully automated method with a sufficient temporal

resolution of 15 ms for a heart rate of 60/min [74], high inter- and intra-observer reproducibility [75], high repeatability [76], and high robustness when dealing with perfusion defects [77, 78].

Six indices from phase analysis have been reported to represent global LV mechanical dyssynchrony commonly [72, 79, 80]:

1. Peak phase, which is the most frequent phase angle among LV myocardium.
2. Phase standard deviation (PSD), which is the standard deviation of the phase distribution.
3. Phase histogram bandwidth (PBW), which includes 95% of the samples in the phase histogram width.
4. Phase histogram skewness, which indicates the symmetry of the histogram.
5. Phase histogram kurtosis, which shows the degree of peakedness of a distribution.
6. Phase entropy (PE) was calculated by the total number of samples and the proportion of the samples with their phase angle over the total number of samples in the phase histogram, which indicates the "disorder" of the histogram.

LV systolic dyssynchrony has been frequently used to select CRT patients and recommend the optimal LV lead positions [9, 81]. Besides LVSD, LVDD also plays an

important role in HF patients [82]. Wang et al. [80] found that the LV systolic and diastolic parameters from gated SPECT MPI, including PSD, PBW, and PE, had great prognostic values for dilated cardiomyopathy patients.

Besides the features of LV dyssynchrony, right ventricular (RV) dyssynchrony might also have great potential for guiding CRT. Wang et al. [11] first evaluated the RV dyssynchrony measured by phase analysis of FDG-PED imaging, and compared the results with the RV dyssynchrony from echocardiography, which showed a great correlation. Zhou et al. developed an RV phase analysis tool that cooperated with LV phase analysis for measuring interventricular mechanical dyssynchrony by gated SPECT MPI. The difference between the LV and RV contraction delays represented the interventricular contraction delay, which was compared with the interventricular conduction delay classified by ECG to validate the concordance of interventricular mechanical and electrical dyssynchrony. In 61 enrolled patients with bundle branch block (BBB), there was an agreement rate of 86.9% [13].

Nuclear imaging to detect wall thickening Gated nuclear MPI is a dynamic imaging modality, which can identify the motion of the LV wall with relative hypoperfusion. Similar to myocardial perfusion, regional myocardial motion and thickening can be quantitative to thickening scores [83]. Cooke et al. [84] developed a count-based method to assess systolic wall thickening from the regional LV count changes during the cardiac cycle from gated SPECT MPI, which had been quantitatively and

clinically evaluated. Several other researchers conducted related clinical validation studies. Nowak et al. found that the quantitative analysis of ^{99m}Tc-MIBI SPECT was significantly affected by heterogeneity in regional myocardial systolic wall thickening. The mean uptake was significantly higher in the lateral wall ($84\% \pm 5\%$) than in the septal wall ($65\% \pm 10\%$), anterior wall ($71\% \pm 11\%$), and posterior wall ($71\% \pm 11\%$) (P¡0.01) [85]. Huang et al. (Huang et al., 2006) proposed a wall motion model to measure mechanical dyssynchrony and identify the maximum delay for guiding LV lead placement in CRT patients. Moreover, Sharir et al. [83] analyzed the relationship between myocardial thickening and LV remodeling by resting gated SPECT MPI in patients with a history of myocardial infarction, and demonstrated that both global and local abnormal thickening were independently correlated to the LV function.

Nuclear imaging to guide CRT patient selection Current guidelines indicate that CRT should be used for patients with LVEF $\leq 35\%$, sinus rhythm, LBBB with a QRS duration greater than or equal to 150 ms, and NYHA class II, III, or ambulatory IV, symptoms on GDMT [25]. In addition to these criteria, several studies have shown that LV myocardial viability and mechanical dyssynchrony from nuclear imaging have significant values in CRT patient selection.

Adelstein et al. [65] analyzed the difference between 190 ICM CRT recipients with scar burden, 380 non-ICM CRT recipients, and 50 CRT patients with unsuccessful

LV lead implementation and found that ICM patients had significantly worse survival and less LVEF improvement than non-ICM patients (P¡0.01). Moreover, the results showed that the ICM patients with low scar burden (summed rest score [SRS] < 27) had better CRT response than ICM patients with a high scar burden (SRS ≥ 27). Therefore, the scar burden assessed by SPECT MPI is useful for guiding CRT patient selection.

The systolic PSD and PBW characterizing global mechanical dyssynchrony has been widely used to select appropriate CRT patients [78]. In a prospectively single-center study, Friehling et al. [37] evaluated the difference in LV synchrony after CRT implementation by phase analysis of gated SPECT MPI. The presence of baseline dyssynchrony, myocardial scar burden, and LV lead concordance was used to predict the change in LV synchrony. After a 9.6±6.8 months follow-up, the patients with a negative CRT response showed significant deterioration in synchrony, compared with patients with a positive CRT response or no change (p=0.003). So, the phase analysis of gated SPECT MPI could be used to predict a change in LV synchrony and CRT response after CRT, which could guide CRT patient selection, as shown in Figure 1.2. Furthermore, in a retrospective study, Henneman et al. [2] found that the baseline PSD and PBW could improve the prediction of CRT response: a cutoff value of 43° for PSD yielded a sensitivity and specificity of 74%, and 135° for PBW yielded a sensitivity and specificity of 70%. Other studies found greater accuracy for predicting CRT response by different baseline threshold levels of dyssynchrony from SPECT-MPI,

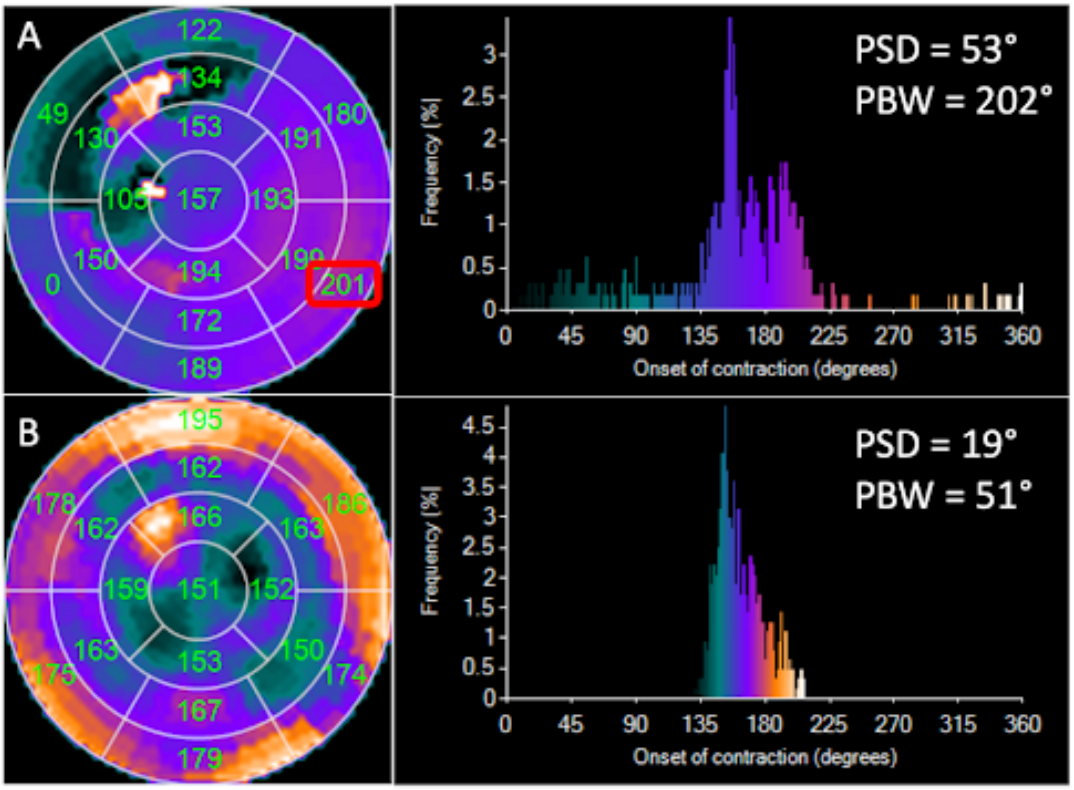

Figure 1.2: An example of mechanical dyssynchrony to guide CRT patient selection and LV lead placement by Emory Cardiac Toolbox V4.0. A: The phase polar map and histogram of a 59-years old patient before CRT implementation. This patient had NYHA class IV, LBBB, QRSd = 160 ms, LVEF = 24%, PSD = 53°, and PBW = 202°. PSD and PBW both meet the cut-off value of CRT patient selection in multiple studies [1, 2, 3]. In addition, the mid-inferolateral segment had the highest mean phase angle (201°) (red square in A), suggesting that the LV lead should be in the mid inferolateral segment. B: The phase polar map and histogram of the same patient after CRT implementation. This patient's lead was placed at the lateral vein under the guidance of mechanical dyssynchrony and had a super response (LVEF = 49%, PSD = 19°, PBW = 51°) after CRT implementation.

such as a cutoff value of 21° for PSD with 90% sensitivity and 74% specificity, and a cutoff value of 112° for PBW with 72% sensitivity and 70% specificity [1]; a cutoff value of 43° for PSD with 86% sensitivity of and 80% specificity, and a cutoff value of 128° for PBW with 86% sensitivity and 80% specificity [3]. However, a prospective

study found that baseline PBW and PSD could not predict LV reverse remodeling [86]. In addition, in a prospective international clinical study, Peix et al. found that the difference between baseline and six months post-CRT dyssynchrony was significantly related to the CRT response, instead of the LV baseline dyssynchrony itself [87].

Nuclear imaging to identify the optimal LV lead position

Current guidelines recommend the LV lead to be located in posterior and lateral walls, which enables the selection of the best pacing site [88, 89]. However, this non-individual recommendation of LV lead positions might cause suboptimal or inappropriate placement in a large number of patients [9].

The LV lead position is essential for CRT response, which should be placed away from the scar and at or near the latest activated site, as shown in Figure 1.2. In a retrospective study, Boogers et al. [41] analyzed the concordance between the site of the latest mechanical activation assessed by SPECT MPI and the LV lead position on fluoroscopy and evaluated this concordance with CRT response, which was defined as a decrease of $\geq 15\%$ in LVESV assessed by echocardiography. Consequently, most of the latest activated sites were in the posterior (42.4%) and lateral (23.3%) walls. LV leads in 52 patients were placed at the latest activated sites, and 79% of them had favorable CRT responses. However, only 26% of 38 patients with discordant LV lead positions had positive CRT responses. This study showed that patients with

a concordant LV lead position had a significantly better CRT response than those without a concordance.

In a prospective study, Friehling et al. [37] found that 96% of patients with an acceptable scar and concordant LV lead position had a favorable CRT response and long-term outcome. Similarly, Uebleis et al. [71] found that the CRT responders had lower phase entropy and myocardial scar burden than non-responders.

Zhou et al. [81] developed an automatic method to identify the latest contracting viable LV segments from ECG-gated SPECT MPI for guiding CRT LV lead placement. The automatic assessment was validated by the percent agreement with the segments visually recommended by two experts from the short-axis images and polar maps of viability and phase. The agreement rate of these two methods could be as high as 97.2% for selecting the optimal LV pacing sites, and the rate of inter-operator reproducibility could achieve 88.8%. Furthermore, because the latest activated segment may not be achieved due to the sparse and personalized anatomy structure of the veins, Zhang et al. [43] proposed a novel hierarchical recommendation method for LV pacing site based on the concordance between the lead position and the latest activated viable site. The apical, septal, and segments with more than 50% scar were excluded first. Afterward, the 1st level of LV pacing site recommendation is the latest contracting viable segment; the 2nd level of recommendation is the late contracting viable segments within 10° of the latest contraction delay; the 3rd level

of recommendation is the viable segments adjacent to the 1st recommendation. According to the results of this hierarchical recommendation method, the CRT response rates were 75.6% in the patients with recommended LV lead locations (n = 41) and 51.9% in the patients with non-recommended LV lead locations (n = 27) (P = 0.043), respectively. The response rates were 66.2% in the patients with LV lead in neither the apex nor scar segments (n = 68) and 27.3% in either apex or scar segments (n = 11) (P = 0.014), respectively. It should be noted that the response rates for 3 recommendation levels were similar (76.9% [1st level, n=13], 76.9% [2nd level, n=13], and 73.3% [3rd level, n=15] [P = 0.967]), which indicated that pacing at any of the three recommendations resulted in a similar CRT response rate. In addition, over a median follow-up of 49 months, the recommendation group had lower all-cause mortality and fewer composite events compared with the non-recommendation group and the apex or scar group.

Nuclear imaging to guide LV lead placement

Integrated multi-modality cardiac imaging can visualize the concordance between LV lead position and the latest activated viable region for navigating CRT LV lead placement [54].

Most CRT implanters use fluoroscopy venograms to visualize coronary venous structures and guide the lead placement during implantation of CRT [90]. The optimal LV pacing site from nuclear imaging may not contain any suitable venous branch for

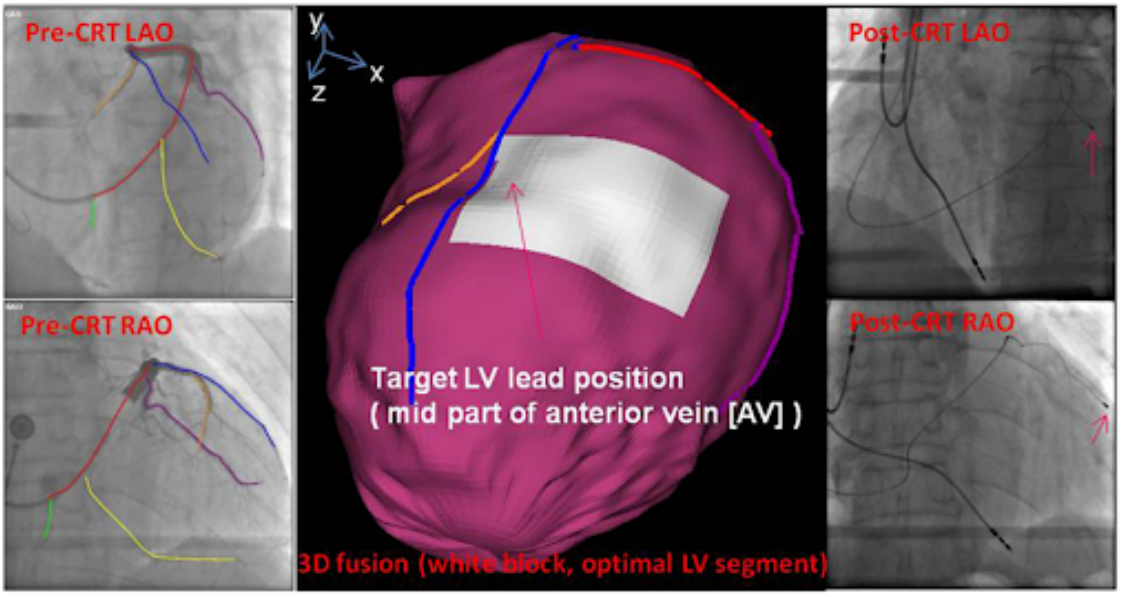

Figure 1.3: 3D SPECT and fluoroscopy image fusion to guide the selection of target venous site and navigate the CRT left-ventricular lead placement [4]. The major veins were manually identified by operators on the pre-CRT fluoroscopic images, reconstructed to a 3D structure, and fused with SPECT MPI epicardial surface. The middle part of the anterior vein was the targeted LV lead position, which overlapped with the recommended LV lead segment (the white segment). The LV lead was placed under the guidance of this 3D fusion model to the target venous site (red arrows), as shown in the post-CRT fluoroscopy images. The QRS duration decreased from 168 to 140 ms immediately after the CRT device was turned on. After a 1-month follow-up, the LVEF increased from 32% to 57% assessed by echocardiography.

the LV lead placement [9]. Moreover, implanters may not be able to accurately combine the venous anatomy with the latest activated viable segment. Such inaccurate correspondence may result in undesired or inappropriate LV lead placement, as a 20 mm difference in the LV lead position may affect the CRT response [91]. As shown in Figure 3, a 3D fusion method was developed to integrate LV venous anatomy reconstructed from fluoroscopy venograms with LV epicardial surface extracted from SPECT MPI for navigating CRT LV lead placement. This method was evaluated

against the manual fusion between SPECT MPI and CT venograms. For each patient, both CT and fluoroscopic veins were rendered on the SPECT LV epicardial surface. The overall distance-based mismatch error between the fluoroscopic and CT veins was 4.6 ± 3.6 mm, and the segment-based kappa agreement rate was 0.87 (95% CI: 0.82-0.93) [4].

Another potentially more direct method to guide CRT lead placement is integrating the venous anatomy from CT venograms with LV epicardial surface from nuclear images. Imaging CRT was the first prospective double-blinded randomized clinical trial to integrate CT venography, ^{99m}Tc SPECT MPI, and speckle-tracking echocardiography radial strain for guiding CRT LV lead placement. It targeted the optimal coronary sinus branch closest to the non-scarred myocardial segment with the latest mechanical activation. It demonstrated that multi-modality imaging-guided LV lead placement could improve the CRT response (74% vs. 58%, p=0.02) (Sommer et al., 2016). Tada et al. proposed a novel method using fusion images between CT venograms and MPI to target LV lead position for the optimal CRT, which was applied in 4 HF patients and evaluated by symptomatic (NYHA) and echocardiographic functional parameters (LVESV and LVEF). All patients were identified as responders to CRT [92].

Larg multi-center nuclear image-guide clinical trials

In a prospective study conducted by Peix et al. [87], 195 sequential patients were enrolled in a non-randomized, multicenter trial titled *Value of intraventricular synchronism assessment by gated-SPECT myocardial perfusion imaging in the management of heart failure patients submitted to cardiac resynchronization therapy (VISION-CRT).* All patients met the standard criteria for CRT: NYHA class II, III or ambulatory IV heart failure for at least three months before enrolment; LVEF $\leq$ 35% from ischemic or non-ischemic causes; QRS duration $\geq$ 120 ms, with the morphology of LBBB; sinus rhythm. The primary outcome was any improvement of the following: $\geq$ 1 NYHA class, LVEF by $\geq$ 5%, reduction in ESV by $\geq$ 15%, and $\geq$ 5 points in Minnesota Living with Heart Failure Questionnaire (MLHFQ). The LV dyssynchrony and viability were quantified from gated SPECT MPI to predict clinical outcomes at 6 months follow-up. It was reported that the baseline dyssynchrony was not associated with the primary outcome in univariable (OR 0.7, 95% CI 0.33-1.5) or multivariable analyses (OR 0.66, 95% CI 0.25-1.76). However, the changes in dyssynchrony showed a significant correlation with the occurrence of the primary outcome (OR 1.04, 95% CI 1.01-1.07, P = .007; OR = 1.04 per 1° decrease in LV PSD). Thus, the change of LV mechanical dyssynchrony measured by PSD from gated SPECT MPI was a valid marker of CRT clinical outcome. Also, the subgroup analysis showed that the patient with on-target (OR 1.55, 95% CI 0.63-3.84) or acceptable lead placement that the lead was placed in segments within 10° of the latest viable contracting segment (OR 1.53, 95% CI 0.71-3.28) was also associated with the primary outcome, but not

significant. The reason for this problem might be that the electrophysiologists involved in the study who were provided the LV lead position, although blinded to the gated SPECT MPI results, had access to scar distribution from echocardiography. Moreover, this clinical trial was not a randomized trial, and even though all patients were analyzed prospectively, the decision as to whether the position of the lead was placed on the target was determined retrospectively.

Zou et al. conducted the other large prospective, multicenter, randomized, controlled study titled *SPECT Guided LV Lead Placement for Incremental Benefits to CRT Efficacy (GUIDE-CRT)* [10]. The GUIDE-CRT trial enrolled 194 consecutive patients with sinus rhythm with QRS duration ≥ 120 ms, LVEF $\leq 35\%$, and NYHA functional class II to IV from 19 centers across China. All patients were randomly assigned to the guided group or control group. In the guided group, the LV lead was placed in the optimal segment that was identified among the middle and basal segments with the largest mean phase angles and scar burden $< 50\%$, assessed by gated SPECT MPI; or in the segments adjacent to the optimal segment and with scar burden $< 50\%$. Then, those segments were displayed on a 3D LV surface and integrated with 2D fluoroscopy venograms to provide the navigation map. In the control group, all patients underwent standard CRT guidelines for LV lead placement. In consequence, the guided group had a significantly higher on-target rate for the LV lead placement (85.5% vs. 62.4%; $p = 0.002$), and the patient with LV lead placed in on-target segments had a better CRT response rate than the patients with LV lead placed in

non-recommended segments (57.1% vs. 35.0%; p = 0.025).

1.2.3 Application of artificial intelligence in guiding CRT

The above clinical studies and trials showed that many clinical parameters were associated with CRT response, including the presence or degree of baseline medical records, ECG parameters, and nuclear test results. Moreover, dichotomizing utilization such as QRS duration may suboptimally stratify response [14, 93].

Traditional statistical analysis methods have extensively investigated predictors contributing to CRT patient selection. However, due to the complexity and the intercorrelation among these predictors, it is a great challenge to build an effective model to interpret them and make clinical decisions.

Machine learning (ML) is a computational discipline designed to recognize complex patterns and make the most accurate predictions from large amounts of data. ML has been applied within cardiology to generate clinical reports and quantitative diagnosis, and predict risk in nuclear cardiology [94, 95]. Motwani et al. [96] employed a LogitBoost algorithm by the open-source Waikato Environment for Knowledge Analysis (WEKA) platform to predict all-caused morality in 10,030 patients with suspected coronary artery disease (CAD) based on 25 clinical features and 44 coronary computed tomographic angiography parameters. The AUC of ML showed significantly

high accuracy. Arsanjani et al. [97] found that compared to the analysis of experts, a boosted ensemble ML algorithm (LogitBoost) (accuracy: 87.3) could significantly improve the diagnostic performance of CAD by computational integration of quantitative perfusion and clinical data in 1,181 SPECT MPI studies.

ML has been used in CRT data analysis in a very limited number of studies. Schmitz et al. [98] established a classification model for CRT patient selection using identified genetic variants and clinical records. Peressutti et al. [99] proposed an ensemble learning classification model to identify CRT 'super-responders' based on LV motion analysis on cardiac MRI. Kalscheur et al. [100] applied ML methods for predicting all-cause mortality and heart failure hospitalization in 595 CRT patients from the COMPANION trial (Comparison of Medical Therapy, Pacing, and Defibrillation in Heart Failure). The authors evaluated several supervised ML models, which were trained from the data with labeled outcomes, based on 49 preimplant features obtained from clinical history, ECG data and basic echocardiographic features. The Random Forest method had the most accurate prediction (AUC 0.74; 95% CI, 0.72–0.76), and the sensitivity, negative predictive, specificity, and positive predictive are 52%, 38%, 80%, and 88%, respectively. In addition, Cikes et al. [101] applied an unsupervised ML method (multiple kernel learning and k-means clustering) without labeled outcomes or classes to categorize subjects by similarities in clinical parameters, LV volume and deformation traces at baseline into four mutually exclusive groups. The treatment effect of CRT-D on the primary outcome (all-cause death or HF event) and on volume

response was compared among these groups. Among the four groups with significant differences in the majority of baseline clinical characteristics, biomarker values, measures of left and right ventricular structure and function, and the primary outcome occurrence, two groups included a higher proportion of known clinical characteristics predictive of CRT response. They were associated with a substantially better treatment effect of CRT-D on the primary outcome than observed in the other groups. This method may provide a clinically meaningful classification of a phenotypically heterogeneous HF cohort.

Deep learning is a more complicated ML method. It has been used to extract information from heterogeneous data and predict information with very high accuracy [102]. Wang et al. [103] employed a V-net-based deep learning method to extract LV myocardial contours and quantify LV functions on gated SPECT MPI. The Dice similarity coefficient (DSC), which was used to measure the performance of image segmentation models, was 0.907 ± 0.039 (endocardium), 0.926 ± 0.021 (myocardium), and 0.965 ± 0.011, respectively. The correlation coefficient of the LV volume between the ground truth and the proposed method was 0.939 ± 0.103. Betancur et al. [104] developed a deep convolutional neural network to predict obstructive disease from SPECT MPI polar maps as compared with the current standard quantitative method (total perfusion deficit) (sensitivity: 82.3% vs. 79.8% [per-patient prediction of obstructive disease], 69.8% vs. 64.4 [per-vessel prediction of obstructive disease]). Compared to ML, deep learning is scalable and performs better with a larger amount

of data [105]. The application of an unsupervised ML method in classifying heterogeneous HF provides a clinically interpretable method to select CRT responders.

1.2.3.1 Reinforcement learning

Reinforcement learning is particularly well suited for complex tasks similar to clinical decision-making because the agents trained in the model can act on training with an incomplete amount of data and perform sequential steps to optimize rewards[106, 107, 108, 109, 110]. However, training a prediction model requires a large amount of correct sample data for supervised learning, which may lead to incorrect decisions even though the prediction task can be accomplished by imputation[111, 112]. Furthermore, reinforcement learning agents' rewards can be sparsely defined based on expert or domain knowledge [108].

1.2.4 Challenges and future of nuclear imaging to guide CRT

Nuclear imaging for guiding CRT has shown great potential in clinical studies, due to its ability to automatically and accurately characterize myocardial perfusion, and mechanical dyssynchrony, and identify the optimal LV lead positions. However, there are still major challenges in nuclear imaging for guiding CRT:

† The technical limitation of low spatial resolution in PET/SPECT MPI makes it difficult to measure non-transmural scars. In addition, the phase analysis technique relies on gated image acquisition. However, during ECG-gated image acquisition, only 8 or 16 frames are commonly detected in a cardiac cycle, which can influence the assessment of regional wall motion and thickening [9, 54].

† It is important to explore better technical/ clinical predictors. The commonly used parameters, PSD and PBW were reported to have significant predictive values in a number of studies; however, a recent large multi-center trial showed that the baseline LV PSD and PBW were not predictive in the CRT response [87].

† Mechanical and electrical dyssynchrony should be analyzed together to improve CRT patient selection. It had been shown that QRSd could be used to differentiate LBBB patients between with or without mechanical dyssynchrony, but LBBB was not always accompanied by mechanical dyssynchrony [113].

1.3 Dissertation Outline and Contributions

This section outlines my work on mechanical dyssynchrony and electrical dyssynchrony for CRT patient selection. A high-level summary of each chapter along with corresponding novel contributions is presented.

Chapter 2 presents LV shape parameters derived from gated SPECT MPI and finds that these parameters have the promise to improve the prediction of the super-response to CRT. Also, the left ventrical mechanical dyssynchrony (LVMD) parameters were compared in patients with ischemic cardiomyopathy(ICM) and dilated cardiomyopathy(DCM) patients, and found that LVMD parameters were better than clinical guidelines for predicting CRT response for different etiologies.

Chapter 3 presents an autoencoder to discover new predictors from LVMD SPECT MPI and has resulted in statistically significant improvement in the performance of the CRT patient selection. The visualization and statistical analysis presented in the chapter further enhance the clinical explainability of the autoencoder-extracted parameters.

Chapter 4 proposes an end-to-end ECG classification framework using a 2D CNN classifier. By utilizing the STFT to transform one-dimensional waveforms into two-dimensional frequency-time spectrograms, our framework integrates a generalized pre-trained two-dimensional CNN model for predicting whether a patient corresponds to CRT. The proposed approach outperforms existing clinical guidelines as well as popular machine learning models.

Chapter 5 introduces a novel approach for determining the latest activation position of the heart using VCG and combining it with the latest contraction position measured by SPECT MPI. This innovative method aims to suggest an optimized position for the

placement of the CRT LV lead through electromechanical dyssynchrony concordance.

Chapter 6 utilizes deep reinforcement learning to tackle the challenge of determining optimal treatment decisions for patients undergoing CRT. We explore models with a discrete state space and specific action space to identify the most effective treatment policy, improve the reward equation based on the insights of experienced physicians, and leverage Deep Q-learning and PPO networks to approximate the best action value function. These efforts aim to improve the treatment policy utilized by clinicians and provide interpretability. Future research should examine the learned policies for each patient and explore alternative modeling approaches, such as model-based reinforcement learning.

Chapter 7

1.4 List of Relevant Publications

The work collected in this dissertation is based on the following publications:

He Z, Zhang X, Zhao C, Ling X, Qian Z, Wang Y, Hou X, Zou J, Zhou W. A method using deep learning to discover new predictors from left-ventricular mechanical dyssynchrony for CRT response. *Journal of Nuclear Cardiology.* 2022 Aug 1:1-2 (IF 5.95)

He Z, Li D, Cui C, Qin HY, Zhao Z, Hou X, Zou J, Chen ML, Wang C, Zhou W. Predictive values of left ventricular mechanical dyssynchrony for CRT response in heart failure patients with different pathophysiology. *Journal of Nuclear Cardiology.* 2021 Sep 17:1-2. (IF 5.95)

He Z, Fernandes FA, Nascimenta EA, Garcia EV, Mesquita CT, Zhou W. Incremental value of left ventricular shape parameters measured by gated SPECT MPI in predicting CRT super-responders. *Journal of Nuclear Cardiology.* 2021 Jan 27. (IF 5.95)

He Z, Garcia EV, Zhou W*. Chapter 24 – Nuclear imaging guiding cardiac resynchronization therapy in Nuclear Cardiology: Basic and Advanced Concepts in Clinical Practice. Springer-Nature. Book chapter. 2021. https://dio:10.1007/978-3-030-62195-7

He Z, Tang H, McGonigle D, Zhang C, Jiang Z, Zhou W. A Deep-Learning-Based Segmentation Method for Left Ventricle on Gated SPECT Myocardial Perfusion Images. *Conference of Midsouth Computational Biology Bioinformatics Society (MCBIOS' 2019).* (Student travel stipend) (Poster)

Hung GU, Zou J, **He Z**, Zhang X, Tsai SC, Wang CY, Chiang KF, Tang H, Garcia EV, Zhou W, Huang JL. Left-ventricular dyssynchrony in viable myocardium by myocardial perfusion SPECT is predictive of mechanical response to CRT. *Annals of*

Nuclear Medicine. 2021 May 21:1-8. (IF 2.61)

Wang CY, Hung GU, Lo HC, Tsai SC, **He Z**, Zhang X, Chiang KF, Zou J, Zhou W, Huang JL, Chen SA. Clinical impacts of scar reduction on gated myocardial perfusion SPECT after cardiac resynchronization therapy. *Journal of Nuclear Cardiology*. 2021 Aug 19:1-9. (IF 5.95)

Jiang W, Liu Y, **He Z**, Zhou Y, Wang C, Jiang Z, Zhou W. Prognostic value of left ventricular mechanical dyssynchrony in hypertrophic cardiomyopathy patients with low risk of sudden cardiac death. *Nuclear medicine communications*. 2021 Feb 1;42(2):182-189.

Zhou Y, **He Z**, Liao S, Liu Y, Zhang L, Zhu X, Cheang I, Zhang H, Yao W, Li X, Zhou W. Prognostic value of integrative analysis of electrical and mechanical dyssynchrony in patients with acute heart failure. *Journal of Nuclear Cardiology*. 2020 Nov 4. (IF 5.95)

Hua X, Han J, Zhao C, Tang H, **He Z**, Chen Q, Tang S, Tang J, Zhou W. A novel method for ECG signal classification via one-dimensional convolutional neural network. *Multimedia Systems*. 2020 Nov 11:1-3.

Wang C, Shi J, Ge J, Tang H, **He Z**, Liu Y, Zhao Z, Li C, Gu K, Hou X, Chen M. Left ventricular systolic and diastolic dyssynchrony to improve cardiac resynchronization

therapy response in heart failure patients with dilated cardiomyopathy. *Journal of Nuclear Cardiology.* 2020 May 13. (IF 5.95)

Zhang F, Wang J, Shao X, Yang M, Qian Y, Yang X, Wu Z, Li S, Xin W, Shi Y, Liu B, Yu W, **He Z**, Zhou W, Wang Y. Incremental value of myocardial wall motion and thickening to perfusion alone by gated SPECT myocardial perfusion imaging for viability assessment in patients with ischemic heart failure. *Journal of Nuclear Cardiology.* 2020 Feb 14:1-2. (IF 5.95)

Wang T, Lei Y, Tang H, **He Z**, Castillo R, Wang C, Li D, Higgins K, Liu T, Curran WJ, Zhou W. A learning-based automatic segmentation and quantification method on left ventricle in gated myocardial perfusion SPECT imaging: A feasibility study. *Journal of Nuclear Cardiology.* 2019 Jan 28:1-2. (IF 5.95)

Tang H, Bober R, Zhang C, **He Z**, Zou J, Zhou W. Scale ratio ICP for 3D registration of coronary venous anatomy with left ventricular epicardial surface to guide CRT lead placement. InMedical Imaging 2019: Image-Guided Procedures, Robotic Interventions, and Modeling 2019 Mar 8 (Vol. 10951, p. 1095123). *International Society for Optics and Photonics*

McGonigle D, Zhao D, Tang H, Zhang C, **He Z**, Bober R, Zhou W. Deep Learning to Extract Coronary Arteries from Fluoroscopy Angiography. *Conference of Midsouth Computational Biology Bioinformatics Society (MCBIOS '2019).* (Student

travel stipend) (Poster)

Jiang Z, **He Z**, Zhu F, Tang H, Li D, Zhang C, Zhou W. Machine learning to diagnose CAD from SPECT MPI: a preliminary study. *American Society of Nuclear Cardiology Scientific Session 2018*. (Poster)

Chapter 2

Mechanical dyssynchrony from gated SPECT MPI for CRT patient selection

2.1 Introduction

Existing clinical guidelines for determining whether CRT is feasible and effective are based on very few medical characteristics. For now, CRT is indicated for patients who have a low LVEF (typically $\geq 35\%$), sinus rhythm, left bundle-branch block (LBBB) pattern, QRS duration $\geq 150ms$ on ECG and New York Heart Association (NYHA)

class II, NYHA class III and ambulatory IV symptoms on Guideline Determined Medical Therapy [24, 25].

This chapter demonstrated four new shape parameters for CRT patient selection, of which end-systolic eccentricity (ESE) provides incremental value over existing clinical and nuclear imaging variables [114]; compared the predictive and prognostic values of left ventricular mechanical dyssynchrony (LVMD) measured by gated SPECT MPI and the concordance of LV lead with the sites of the latest contraction or relaxation position in dilated cardiomyopathy (DCM) and ischemic cardiomyopathy (ICM) patients [115].

2.2 Shape parameters for CRT patient selection

2.2.1 Introduction

Ventricular remodeling is characterized by a group of molecular, cellular, and interstitial changes, which occurs after cardiac injury and is clinically manifested by changes in size, shape, and function [116, 117, 118]. In addition, a remodeled ventricle is associated with the development and progression of ventricular dysfunction, arrhythmias, and poor prognosis [119]. Studies have found that LV shape is related to cardiac function; the normal elliptical LV shape would change to a spherical

shape due to the development of eccentric hypertrophy or post-myocardial infarction (MI)[120, 121]. Some shape parameters, such as LV shape index, eccentricity, and elongation, have been reported to have predictive value for congestive heart failure, diabetes, and patients with significant cardiac structural and functional abnormalities [120, 122, 123, 124].

ECG-gated single-photon emission computer tomography (SPECT) myocardial perfusion imaging (MPI) can assess LV structure by the tracer counts of myocardial perfusion, instead of geometric changes in the myocardium, which is more objective and reproducible. Gimelli et al. [125] found that the LV eccentricity measured by gated SPECT MPI predicted the presence of multivessel coronary artery disease (CAD). The left ventricular shape parameters also have a close relationship with LV volumes and function in HF patients [126, 127], even in healthy subjects [123]. Moreover, the LV shape index has been applied to detect the presence of adverse LV remodeling in patients with structural and functional cardiac alterations due to diabetes mellitus [122]. However, very few works have been proposed in the literature for CRT considering LV shape measured by gated SPECT MPI [128].

Super-responders are the patients who have a significant improvement in functional capacity, quality of life, HF symptoms, left ventricular function, and reverse remodeling after CRT [129]. Several studies found that LV shape characteristics, such as smaller LV, less LV end-diastolic diameter, and greater LV strain, measured by

echocardiography, were associated with super-response to CRT [129, 130]. Gated SPECT MPI, which is widely accepted in the clinic, has been validated to effectively access LV shape, due to its high repeatability and reproducibility in the evaluation of myocardial perfusion, global and regional ventricular function, and mechanical dyssynchrony for patients with CRT. This study is a post hoc retrospective analysis of the shape variables in patients obtained from the IAEA VISION-CRT trial. It is aimed to evaluate the clinical role of LV eccentricity measured by gated SPECT MPI in the prediction of super-response to CRT.

2.2.2 Methods

2.2.2.1 Patient Population

The VISION-CRT trial was a prospective multicenter trial that enrolled subjects from 10 cardiological centers in 8 countries (Brazil, Chile, Colombia, Cuba, India, Mexico, Pakistan, and Spain). The complete study design and primary results of VISION-CRT were previously published[87, 128, 131]. The inclusion criteria were as follows: symptomatic HF patients over 18 years old with NYHA functional class II, III or ambulatory IV HF for at least 3 months before enrollment, despite optimal medical treatment according to the current guidelines; LVEF $\leq 35\%$ from ischemic or non-ischemic causes, measured according to the usual procedure at the participating

center for inclusion, whereas LVEFs used for analysis came from the nuclear core lab; sinus rhythm with LBBB configuration defined as a wide QRSd ($\geq$ 120 ms). Exclusion criteria were as follows: right bundle branch block, pregnancy or breast-feeding, acute coronary syndromes, coronary artery bypass grafting, or percutaneous coronary intervention in the last 3 months before enrolment and within 6 months of CRT implantation. The CRT devices were implanted by standard procedures. The LV lead was implanted in the posterolateral coronary vein, depending on vein availability.

Definitions of all clinical variables were outlined before the start of VISION-CRT. Subjects underwent a detailed clinical and gated SPECT MPI evaluation just before recruitment to the study. All patients provided written informed consent, and all procedures were done according to the Declaration of Helsinki.

Clinical parameters and gated SPECT MPI were assessed before CRT (baseline) and at 6 ± 1 month after (follow-up). The patients were classified as "super-responders" to CRT if they had a relative increase of LVEF $\geq 15\%$ as measured by gated SPECT MPI at follow-up. Others were classified as non-super-responders.

2.2.2.2 SPECT MPI Assessment

Gated SPECT MPI was performed around 30 min post injection using 20 to 30 mCi of ^{99m}Tc-sestamibi or tetrofosmin of 740 to 1110 MBq. All the images were acquired in gamma cameras using 180° orbits with a complimentary 8 or 16 frames ECG gating. Image reconstruction and reorientation were completed by Emory Reconstruction Toolbox (ERToolbox; Atlanta, GA) using the ordered subset expectation maximization (OSEM) method with three iterations and ten subsets and filtered by a Butterworth filter with a power of 10 and a cut-off frequency of 0.3 cycles/mm. The resulting short-axis images were sent to Emory Cardiac Toolbox (ECTb4, Atlanta, GA) for automatized accessing of LV function, including LVEF, left ventricular end-systolic volume (LVESV), left ventricular end-diastolic volume (LVEDV), LV shape; end-systolic eccentricity (ESE) and end-diastolic eccentricity (EDE), and LV mechanical dyssynchrony; and phase standard deviation (PSD) and phase bandwidth (PBW). End-systolic volume index (ESVi) and end-diastolic volume index (EDVi) (in milliliters per square meter) are obtained by dividing LVESV and LVEDV by the body surface area (BSA), respectively. Moreover, the latest contracting viable sites could be identified by Emory Cardiac Toolbox as a recommendation of the optimal LV lead position [41]. Concordance is defined as the agreement between CRT LV lead position recorded and the recommended site.

2.2.2.3 Shape Parameters Measured by Gated SPECT MPI

Measurement techniques of myocardial shape variables have been well established. They calculate the 3-dimensional LV shape parameters from gated SPECT MPI [127]. Eccentricity is a measure of the elongation of LV, which is derived from an ellipsoid fitted from the LV endocardial surface according to Eq. 2.1, where x and y are the minor axes, and z is the major axis of the ellipsoid [125].

$$Eccentricity = \sqrt{1 - \frac{x \times y}{Z^2}} \tag{2.1}$$

Based on the assumption that the minor axes have the same length (x = y), the ellipsoid can be considered as a spheroid, as shown in Figure 2.1. The LV eccentricity is closer to 0 if the shape of LV is closer to a sphere and closer to 1 if the shape of LV is closer to a line.

Statistical Analysis

Differences between the super-responders and nonsuper-responders were compared by the Student t test for continuous variables, expressed as mean ± standard deviation, and Pearson χ^2 test for categorical variables, expressed in number and percentage. The univariate binary logistic regression analysis was applied to estimate potential

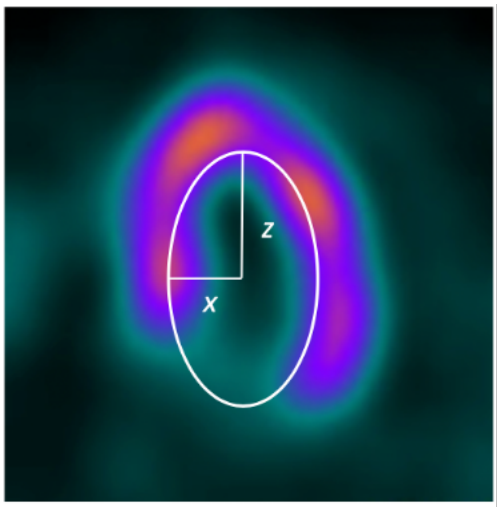

Figure 2.1: The best-fitted ellipsoid based on the LV endocardial surface from a gated SPECT MPI study measured by Emory Cardiac Toolbox (ECTb4, Atlanta, GA).

predictors for super-responders. The multivariable binary logistic regression was performed to analyze the independent predictors of super-responders, and the variables with $P < 0.05$ in the univariate analysis were included. Moreover, the incremental values of shape parameters were evaluated by comparing the receiver operator characteristic (ROC) curve of binary logistic regression from the clinical variables alone, from the combination of clinical variables with ESE or EDE, and from the combination of clinical variables with all shape parameters. $P < 0.05$ was considered to be statistically significant. Statistical analysis was performed by the Python Statsmodels package [132].

2.2.3 Results

2.2.3.1 Baseline Characteristics

A total of 199 patients underwent CRT, but complete data of clinical assessment, baseline SPECT MPI, and clinical 6-month follow-up data were obtained in 177 patients. Among these patients, 11 of them died before the follow-up, and one patient had an extremely small ESV (8 mL), which was an outlier caused by the low resolution of gated SPECT MPI when measuring a small heart. Finally, 165 patients were included in the statistic analysis in this research (Figure 2.2).

The baseline characteristics of the study population are shown in Table 2.1. For all the patients, the age was 60.3 ± 10.9 years, and 98 (59.4%) patients were male. Fifty-one (30.9%) patients had a previous history of CAD. Hypertension (58.8%), smoking (16.4%), and diabetes (24.8%) were also shown in the baseline data.

After 6-month follow-up, 72 of the 165 patients (43.6%) were considered as a super-responder to CRT, and 93 of the 165 patients (56.4%) were considered as non-super-responders. Significant differences of ESE and EDE (0.6 ± 0.1 vs. 0.5 ± 0.2, P = .014; 0.5 ± 0.2 vs. 0.6 ± 0.2, P = .045) were noted between the two groups, as well as other clinical variables, including ACE inhibitors or ARB (65 patients [90.3%] vs. 71

Table 2.1
Baseline characteristics and left ventricular parameters of the enrolled patients

Variables	All (n=142)	DCM (n=92, 64.8%)	ICM (n=50, 35.2%)	P value
ACEI/ARB	136 (82.4%)	65 (93%)	71 (76.3%)	.034
Age	60.3 ± 10.9	61.2 ± 9.9	59.6 ± 11.6	.354
BSA	1.8 ± 0.2	1.8 ± 0.2	1.8 ± 0.2	.984
CAD	51 (30.9%)	14 (19.4%)	37 (39.8%)	.008
Diabetes mellitus	41(24.8%)	16 (22.2%)	25 (26.9%)	.613
Gender	98 (59.4%)	40 (55.6%)	58 (62.4%)	.469
Hypertension	97 (58.8%)	39 (54.2%)	58 (62.4%)	.367
MI	35 (21.2%)	7 (9.7%)	28 (30.1%)	.003
NYHA				.014
II	46 (27.9%)	27 (37.5%)	19 (20.4%)	
III	101 (61.2%)	35 (48.6%)	66 (71.0%)	
IV	18 (10.9%)	10 (13.9%)	8 (8.6%)	
Race				.362
African	17 (10.3%)	8 (11.1%)	9 (9.7%)	
Asian	6 (3.6%)	1 (1.4%)	5 (5.4%)	
Caucasian	23 (13.9%)	10 (13.9%)	13 (14%)	
Hispanic	87 (52.7%)	35 (48.6%)	52 (55.9%)	
Indian	32 (19.4%)	18 (25.0%)	14 (15.1%)	
QRS duration	160.9 ± 25.1	162.9 ± 22.5	159.4 ± 26.9	.378
Smoking	27 (16.4%)	14 (19.4%)	13 (14.0%)	.466
SPECT variables				
Concordance	40 (24.2%)	15 (20.8%)	25 (26.9%)	.474
EDVi	143.1 ± 56.7	132.4 ± 54.5	151.4 ± 57.0	.034
ESVi	106.9 ± 52.4	101.6 ± 52.8	111.0 ± 51.7	.252
EDE	0.5 ± 0.2	0.6 ± 0.2	0.5 ± 0.2	.085
ESE	0.6 ± 0.2	0.6 ± 0.1	0.5 ± 0.2	.014
LVEF	27.7 ± 10.3	25.8 ± 10.3	29.2 ± 10.1	.035
LVEDV	257.6 ± 104.7	239.6 ± 103.7	271.6 ± 103.4	.052
LVESV	192.7 ± 96.2	184.3 ± 98.9	199.2 ± 93.6	.330
PBW	152.4 ± 73.5	145.7 ± 74.4	157.6 ± 72.4	.306
PSD	48.8 ± 19.7	47.6 ± 20.6	49.6 ± 19.9	.520
Scar	24.5 ± 14.4	20.0 ± 11.6	27.9 ± 15.4	$< .001$

Data are expressed as mean ± SD or number (percentage)

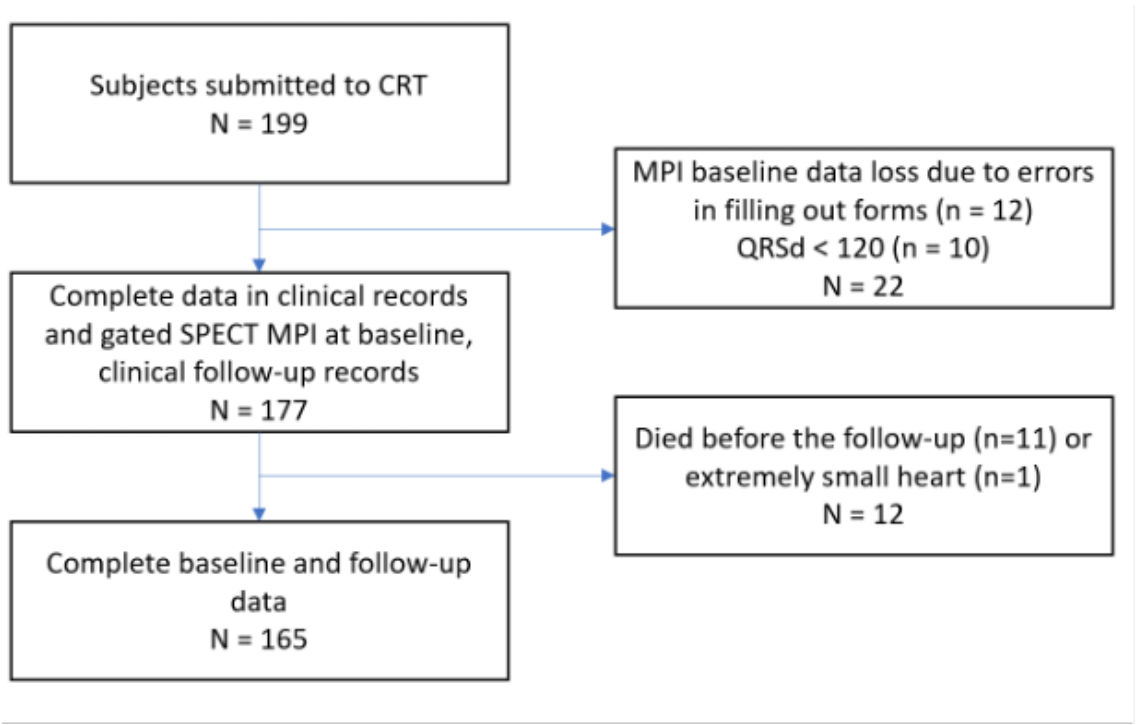

Figure 2.2: Study flow chart. CRT cardiac resynchronization therapy, SPECT gated single-photon emission-computed tomography, MPI myocardium perfusion imaging.

[76.3%], P = .034), CAD (14 [19.4%] vs. 37 [39.8%], P = .008), myocardial infarction (7 [9.7%] vs. 28 [30.1%], P = .003), EDVi (132.4 ± 54.5 vs. 151.4 ± 57.0, P = .034), NYHA (P = .014), LVEF (25.8 ± 10.3 vs. 29.2 ± 10.1, P = .035), and myocardial scar (20.0% ± 11.6% vs. 27.9% ± 15.4%, P < .001). However, the concordance was not statistically significant to distinguish super-response and non-superresponse (P = .474). If the significance level was set at 0.1, EDE (0.6 ± 0.2 vs. 0.5 ± 0.2, P = .085) could also be statistically significant. Representative examples of super-responders and non-super-responders are depicted in Figure 2.3.

Prediction of Super-Response to CRT

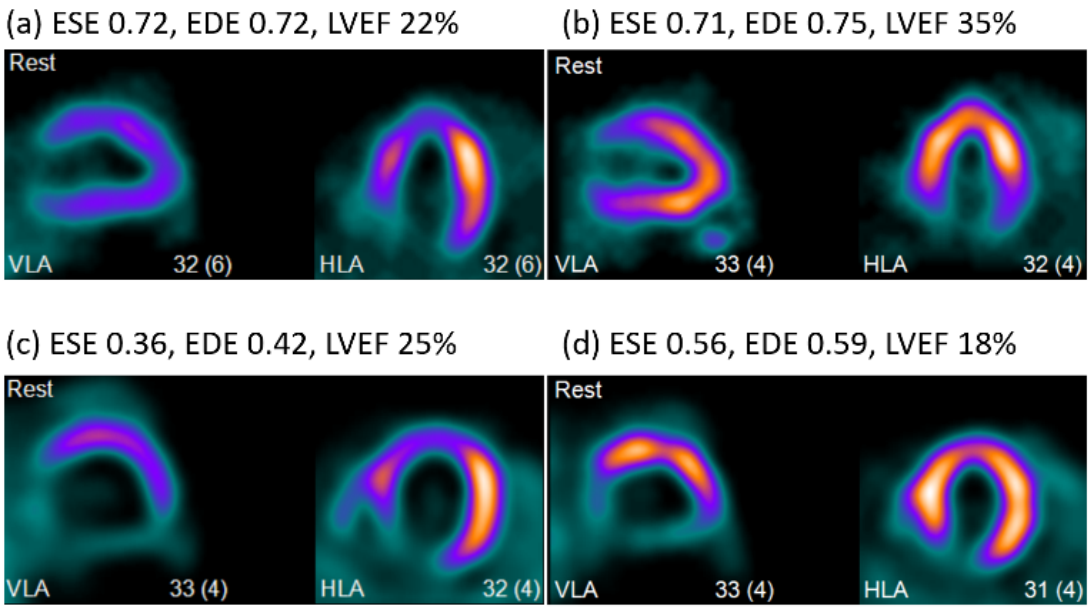

Figure 2.3: Illustrations of the end-systolic frames of a super-responder and a non-super-responder. (**a**, **b**) are the baseline and follow-up vertical long axis (VLA) and horizontal long axis (HLA) images of a 57-year-old male as an example of a super-responder. (**c**, **d**) are the baseline and follow-up VLA and HLA images of a 54-year-old male as an example of a non-super-responder.

In the univariate analysis, ACEI or ARB (OR 2.88, 95% CI 1.15–7.18, P = .024), CAD (OR 0.37, 95% CI 0.18–0.75, P = .006), EDVi (OR 0.99, 95% CI 0.99-1.0, P = .036), myocardial scar (OR 0.96, 95% CI 0.94–0.98, P .001), myocardial ischemia (OR 0.25, 95% CI 0.10–0.61, P = .002), LVEF (OR 0.97, 95% CI 0.941.00, P = .037), and ESE (OR 12.59, 95% CI 1.56101.35, P = .017) were associated with super-response. However, the baseline mechanical dyssynchrony (PSD, P = .518; PBW, P = .304) and concordance (P = .369) were not significantly associated with super-response. In the multivariate analysis, ESE was also an independent predictor (OR 35.71; 95% CI, 1.66–766.03; P = .006). The results of the univariate and multivariate analysis are

Table 2.2
Univariate and multivariate logistic regression analyses of super-responders defined by a relative increase in LVEF $\geq 15\%$

	Univariate analysis			Multivariate analysis		
Variables	**OR**	**95% CI**	***P* value**	**OR**	**95% CI**	***P* value**
ACEI/ARB	2.88	1.15-7.18	.024	5.27	1.73-16.00	.003
CAD	0.37	0.18-0.75	.006	0.83	0.28-2.45	.730
Concordance	0.72	0.35-1.49	.369			
EDVi	0.994	0.99-1.00	.036	0.98	0.98-0.99	.001
ESVi	1.00	0.99-1.00	.252			
EDE	4.89	0.79-30.44	.089			
ESE	12.59	1.56-101.34	.017	35.71	1.66-766.03	.001
Gender	0.75	0.40-1.41	.377			
LVEF	0.97	0.94-1.00	.037	0.87	0.83-0.92	<.001
LVEDV	1.00	0.99-1.00	.055			
LVESV	1.00	0.99-1.00	.329			
MI	0.25	0.10-0.61	.002	0.25	0.07-0.91	.036
NYHA	0.72	0.43-1.20	.212			
PSD	1.00	0.98-1.01	.518			
PBW	1.00	0.99-1.00	.304			
QRS duration	1.01	0.99-1.02	.376			
Scar	0.96	0.94-0.98	.001	0.97	0.94-1.00	.005

shown in Table 2.2.

In the ROC analysis of LV shape parameters, the area under the curve (AUC) of clinical variables alone (sensitivity 0.65, specificity 0.78, AUC 0.8), the combination of clinical variables with EDE (sensitivity 0.65, specificity 0.8, AUC 0.8), the combination of clinical variables with ESE (sensitivity 0.68, specificity 0.82, AUC 0.82), and the combination of clinical variables with both ESE and EDE (sensitivity 0.67, specificity 0.81, AUC 0.83) increased sequentially, as shown in Figure 2.4.

Furthermore, sequential models indicated that the addition of ESE (likelihood 6.41,

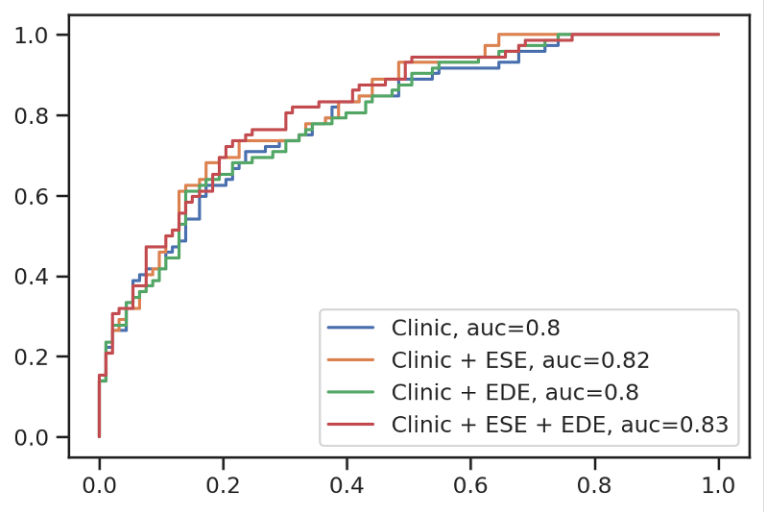

Figure 2.4: Receiver operating characteristic curves of clinical characteristic with or without ESE and EDE.

P = .011) was more strongly associated with CRT super-responders. However, the addition of EDE to a model of clinical characteristics did not provide a significant improvement in association with CRT super-responders. Moreover, due to the collinearity of ESE and EDE (Pearson's correlation coefficient 0.81, P < .001), EDE reduces the performance of the model of ESE plus clinical characteristics (LH 1.55, P = .213), as shown in Figure 2.5.

2.2.3.2 Discussion

This study demonstrates that the LV shape parameter ESE is a promising variable derived automatically from gated SPECT MPI to predict super-responders of CRT. Moreover, it provides incremental value over clinical and nuclear imaging variables. In patients treated with CRT, presenting a super-response is associated with excellent

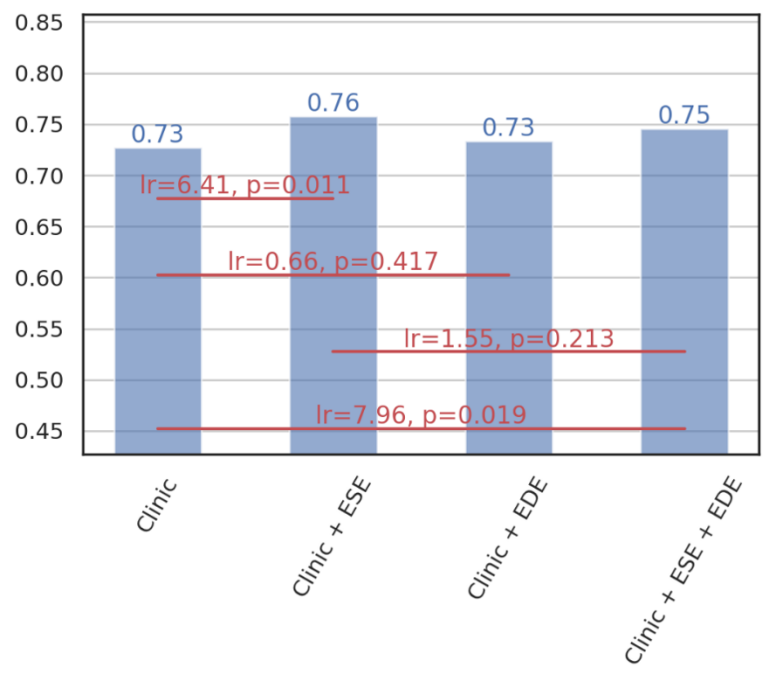

Figure 2.5: Incremental adjusted additive value of eccentricity in the prediction of super-responders of CRT.

long-term outcomes [133]. The identification of these patients can improve our understanding of pathophysiologic mechanisms linked to reverse remodeling and provide better tools to select the best candidates for CRT.

LV remodeling is associated with progressive worsening of LV function and increased cardiovascular morbidity and mortality in various cardiovascular diseases [116, 118]. The most common causes are represented by conditions with an elevated LV hemodynamic load or after myocardial infarction, resulting in an increase in LV chamber volume, muscle mass, and fibrous tissue contents [121, 123]. Several reports have suggested that descriptors of LV shape enhance the ability to discriminate normal from pathological LV because the occurrence of abnormal LV eccentricity takes place

even before the change in LV systolic function becomes apparent [134, 135].

The degree of LV enlargement and dysfunction is known to be directly related to the risk of death [136]. However, in gated SPECT and echocardiography, the measurement method of sphericity is different. In two-dimensional echocardiography, LV geometry is calculated from manual measurements, which is subject to variability and depends on the experience of the operator. The three-dimensional measurement of ventricular shape by gated SPECT MPI derives automatically and it has been demonstrated to be highly reproducible [127]. Two similar shape variables, end-systolic shape index (ESSI) and end-diastolic shape index (EDSI), were also tested in our research. The left ventricle shape index, defined as the ratio of the maximum 3D short- and long-axis dimensions of the left ventricle at the end-systolic or end-diastolic frame, is measured by gated SPECT MPI and has a great correlation with ESE (Pearson correlation coefficient, 0.98) and EDE (Pearson correlation coefficient, 0.99), respectively. ESSI was a significant independent predictor of CRT super-responders (OR, 0.036, 95% CI 0.00–0.77, P = .033). EDSI could also predict CRT super-responders (OR, 0.063, 95% CI 0.00–1.70, P = .10). In addition, ESSI had an incremental value to predict CRT responders, but EDSI did not. Therefore, no matter how the LV shape is defined, it has great potential to predict CRT super responders.

The improvements in LVEF and the reductions in LVEDV are generally modest for

patients with heart failure who undergo CRT. But some part of patients had a dramatic response to CRT (super-responders). Bulava et al. [137] were the first to describe this phenomenon in a 72-year-old woman with ischemic cardiomyopathy, whose LVEF increased from 15% to 60% at 1-year follow-up after CRT. Rickard et al. [138] identified the super-responders as an absolute LVEF improved by $\geq$ 20%. Killu et al. [139] defined the patients with an absolute change in LVEF of $>$ 15% as super-responders. Ypenburg et al. [140] used the decrease in LVESV $\geq$ 30% as the definition of super-responders. Both of them seem reasonable because LVESV, as a volumetric assessment, is an objective measure that provides information on LV reverse remodeling and predicts long-term clinical outcomes [129]; compared to the improvement in LVESV, LVEF is the most widely used variable in echocardiography and can present the LV function while providing prognostic benefit. Antonio et al. [129] proposed a definition of super-responders: if patients have a reduction of one or more NYHA functional classes, a two-fold increment or an absolute change in LVEF of $>$ 45%, and decrease in the LVESV $>$ 15%. However, this definition of super-responder has limitations, because (1) reduction of one NYHA functional class is a subjective evaluation of the improvement of CRT, which might have a placebo effect in our non-randomized clinical trial; (2) two-fold increment or absolute change in LVEF of $>$ 45% might be too strict to the super-responders.

In our study, the super-response was defined as a relative increase in the LVEF $\geq$ 15%. In general responders (an increase in LVEF $\geq$ 5%), the ESE (0.6 ± 0.1 vs. 0.5

$\pm$ 0.2, P $<$ .001) and EDE (0.6 $\pm$ 0.2 vs. 0.5 $\pm$ 0.2, P = .025) also had differences between responders and non-responders. Both of them were independent predictors for general CRT responders in univariate analysis, but not significant in multivariate analysis. Additionally, a combination of a relative increase in LVEF $\geq$ 15% or a decrease in LVESV $\geq$ 30% was analyzed. In our study, 74 (44.8%) patients had the combined outcome and were classified into super-responders. Significant differences were found between all end-systolic and end-diastolic eccentricity (ESE: 0.6 $\pm$ 0.1 vs. 0.5 $\pm$ 0.2, P = .005; EDE: 0.6 $\pm$ 0.2 vs. 0.5 $\pm$ 0.2, P = .037). Both of them were independent predictors of super-responders in univariate analysis (ESE: OR 18.07, 95% CI 2.14–152.32, P = .008; EDE: OR 6.94, 95% CI 1.08–44.83, P = .042). Due to the collinearity of ESE and EDE, we preferred multivariate analysis in separate models and got a similar result of ESE (OR 12.16, 95% CI 0.95–156.32, P = .055), as shown in Table 3. Although the P value was greater than 0.05, the OR was large, which means a strong association between ESE and super-responders. Moreover, the lead concordance had no predictive value between super-responders (P = .369) and general responders (P = .895).

We also found that scar percentage has a moderate correlation with ESE (Pearson correlation coefficient, -0.36); other clinical characteristics and nuclear imaging variables had a weak correlation with ESE. The relationship between LV shape and LV size is probably complicated, and LV shape may also depend on other factors. All findings have demonstrated that ESE has incremental value over significant clinical

and nuclear imaging variables, including angiotensin-converting enzyme inhibitors (ACEI) or angiotensin II receptor blocker (ARB), CAD, MI, LVEF, and scar burden in predicting CRT super-responders.

There were several limitations in this study. First, this was a post hoc analysis of the VISION-CRT trial that was not a randomized trial. Second, the information provided by the short follow-up period was limited; the prognostic value of LV shape parameters needs further investigation. Third, this study enrolled a relatively small number of patients from multi centers with the inherent limitation of such a study design. Fourth, in the design of the VISION-CRT trial, some variables were not included in the data acquisition, such as heart rate that can influence LVEF [141]. Further investigation with a longer follow-up period is needed to assess LV shape parameters in CRT super-responders.

2.3 Predictive values of left ventricular mechanical dyssynchrony for CRT response in heart failure patients with different pathophysiology

2.3.1 Introduction

There are 30% to 40% of cardiac resynchronization therapy (CRT) recipients who do not benefit from CRT [9, 142]. LV mechanical dyssynchrony (LVMD) parameters measured by phase analysis from gated single-photon emission computed tomography (SPECT) myocardial perfusion imaging (MPI) provide repeatable and reproducible information about the presence of intraventricular synchronism [75, 76]. They have been found to be independent predictors for CRT patient selection [2, 143] and have been proven to have prognostic value [144, 145]. Moreover, the concordance of LV lead on or adjacent to the late contracting viable segments measured by gated SPECT MPI was associated with CRT response, heart failure rehospitalization, and all-cause mortality [43]. In dilated cardiomyopathy (DCM) patients, systolic and diastolic LVMD were independent predictors for CRT response, and pacing the LV lead in the segments with the latest contraction and relaxation would improve the CRT response rate [146]. For ischemic cardiomyopathy (ICM) patients, the systolic phase

bandwidth (PBW) as an LVMD parameter has been identified as an independent predictor of ventricular arrhythmia after CRT implantation [143]. However, comparative studies on the predictive value of LVMD for CRT in HF patients with different pathophysiology are still limited. This study aimed to compare the predictive and prognostic values of LVMD measured by gated SPECT MPI and the concordance of LV lead with the sites of the latest contraction or relaxation position in DCM and ICM patients.

2.3.2 Methods

2.3.2.1 Patient population

CRT recipients were consecutively enrolled in a retrospective database at the First Affiliated Nanjing Medical University Hospital from May 2009 to August 2020. Study subjects selected retrospectively had DCM: a presence of LV dilation and LV systolic dysfunction in the absence of other etiological factors that might cause LV dysfunction by echocardiography according to the recent criteria or CAD that causes global systolic dysfunction [147]; or ICM: epicardial coronary artery stenosis greater than 50% or previous history of coronary revascularization or myocardial infarction [67]. A total of 92 DCM and 50 ICM patients who met the above criteria were included in the study as shown in Figure 2.6. All patients met standard indications for CRT at

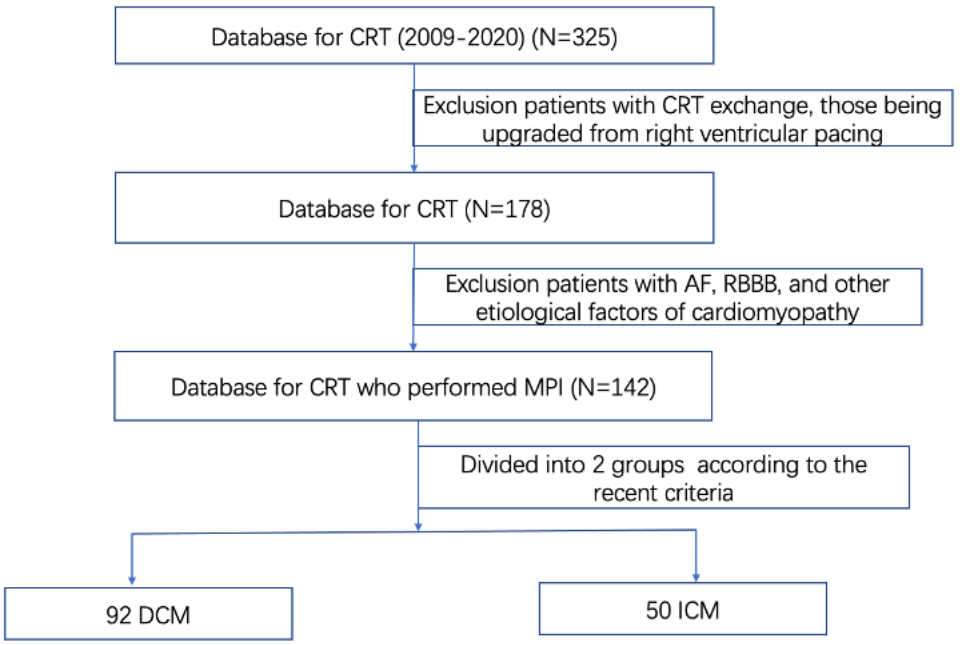

Figure 2.6: Study flow chart. CRT, cardiac resynchronization therapy; AF, atrial fibrillation; RBBB, right bundle branch block; MPI, myocardial Perfusion Imaging; DCM, dilated cardiomyopathy; ICM, ischemic cardiomyopathy.

the time of implantation: LVEF $< 35\%$, QRS duration 120 milliseconds with sinus rhythm, NYHA functional class greater or equal to II, and optimal medical therapy for at least three months before CRT implantation. Exclusion criteria were as follows: atrial fibrillation, right bundle branch block, pregnancy or breastfeeding, and those being upgraded from right ventricular pacing. This study was approved by the Institutional Ethical Committee of the First Affiliated Hospital of Nanjing Medical University.

2.3.2.2 Echocardiography

Echocardiography was performed at baseline before CRT implantation and at the 6-month CRT clinical follow-up. LV function was assessed twice by two experienced ultrasound experts, who were blinded to the clinical data before and six months after CRT implantation, and the mean value was used as the final record. LVEF was calculated using the 2-dimensional modified biplane Simpson method. Echocardiographic response to CRT was defined as an increase in LVEF by 5% or more.

2.3.2.3 SPECT MPI assessment

Gated SPECT MPI was performed around 60 minutes after injection using 20-30mCi of ^{99}mTc-sestamibi. All the images were acquired in a dual-headed camera (CardioMD, Philips Medical Systems) with a standard protocol with 20% energy window around 140 KeV,180° orbit, 32 steps with 25 seconds per step, 8-bin gating, and 64 planar projections per gate. Image reconstruction and reorientation were performed by Emory Reconstruction Toolbox (ERToolbox; Atlanta, GA) using the ordered subset expectation maximization (OSEM) method with three iterations and ten subsets and filtered by a Butterworth low-pass filter with an order of 10 subsets and a cutoff frequency of 0.3 cycles/cm.

The resulting short-axis images were sent to an interactive tool for automatized accessing LV contour parameters by an automatic myocardial sampling algorithm that searched the maximal count circumferential profiles in each cardiac frame. Furthermore, the onset of mechanical contraction and relaxation throughout the cardiac cycle were obtained by multi-harmonic Fourier approximations [148]. Then, the LVMD was represented by phase distribution of systolic and diastolic dyssynchrony for the entire left ventricle, and quantitative parameters of LVMD were calculated as PSD and PBW [72, 148].

2.3.2.4 CRT implantation and LV lead position

The right atrial and ventricular leads were positioned under fluoroscopic guidance by a transvenous approach. The LV lead location was determined by coronary venous angiography cine images in the left anterior oblique (LAO) and right anterior oblique (RAO), and then correlated to the 13-segment polar map of the systolic and diastolic dyssynchrony [67, 90]. LV lead located on or adjacent segment of the latest contraction or relaxation segment was classified as being concordant to the systolic phase or diastolic phase (one-match), respectively, as depicted in two ICM examples in Figure 2.8.

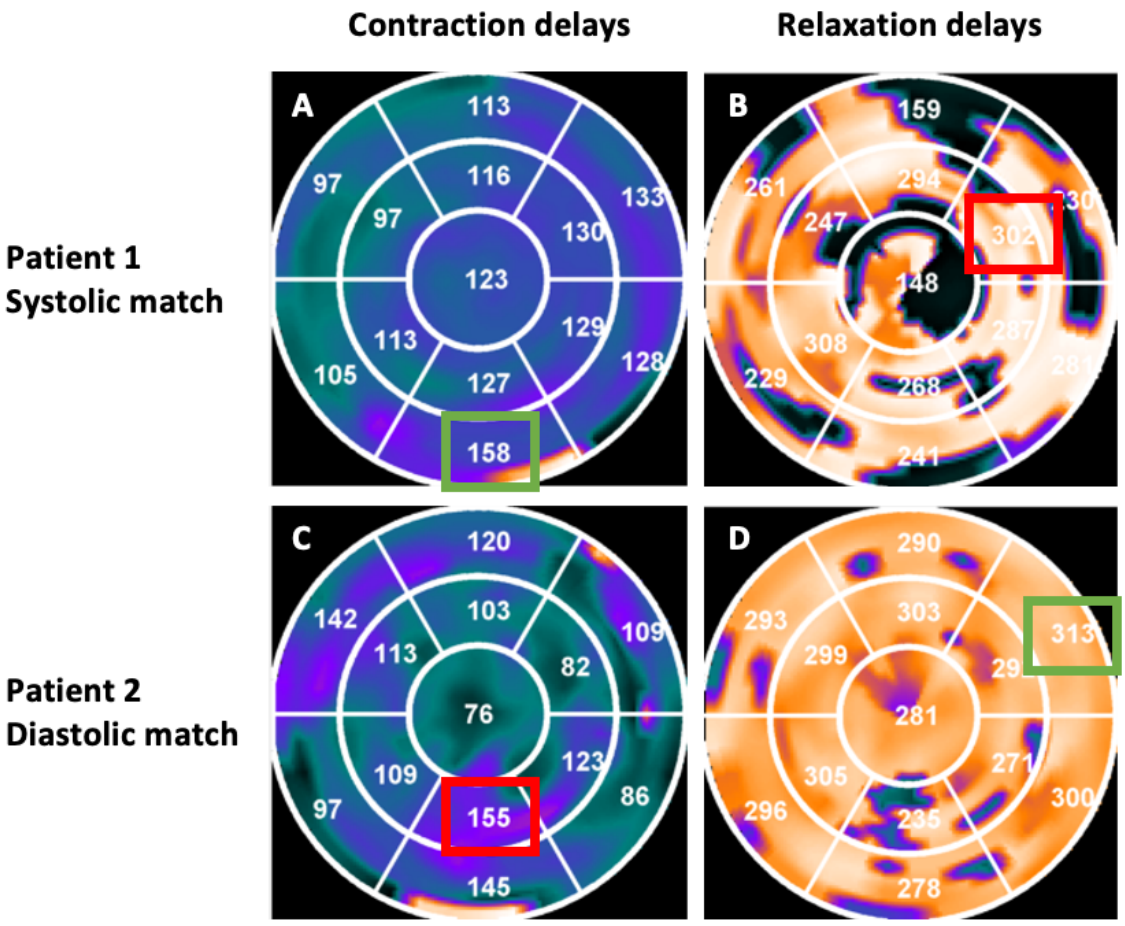

Figure 2.7: Illustrative examples of the systolic match and diastolic match. Polar maps of patient 1 with ICM showing the LV lead located on the latest contraction segment (green in **A**), not on or adjacent to the latest relaxation segment (red box in **B**). This patient is classified as a systolic match. The LV lead of Patient 2 is located on the latest relaxation segment (green box in **D**) and not on or adjacent to the latest contraction segment (red box in **C**).

2.3.2.5 Statistical analysis

The differences between the DCM and ICM were compared by the unpaired t-test for continuous variables, expressed as mean ± standard deviation, and χ^2 test for categorical variables expressed in number and percentage. The systolic and diastolic

LVMD within all patients, DCM patients, and ICM patients were compared by paired t-test. Univariate binary logistic regression analysis was performed on all clinically relevant variables to estimate potential predictors for CRT response. Due to the collinearity between LVMD parameters, and in order to avoid model overfitting, they were entered one by one with those selected variables that were found significant in the univariate analysis in a stepwise fashion into the multivariate logistic regression to obtain the optimal models. Kruskal-Wallis H-test was used to analyze the difference in CRT response rate among three groups in DCM and ICM patients, respectively. Differences in survival over time were analyzed by the log-rank Kaplan-Meier survival analysis. $P < 0.05$ was considered to be statistically significant. Statistical analysis was performed by the Python Statsmodels package [132] and IBM SPSS Statistics software version 26 (SPSS Inc, Chicago, Illinois).

2.3.3 Results

A total of 142 patients (DCM, 92; ICM, 50) who underwent SPECT MPI before CRT implantation were included in this study. The baseline characteristics of the included patients were shown in Table 2.3. For all patients, the age was 64.6 ± 14.5 years, and 71.1% (n=101) patients were male. The baseline QRS duration (157.9 ± 23.3), medical therapy records, and LV functions were also shown in the baseline table. The differences between systolic and diastolic LVMD in all patients, DCM patients, and

Table 2.3
Baseline characteristics and left-ventricular parameters of the enrolled patients.

Variables	All (n=142)	DCM (n=92, 64.8%)	ICM (n=50, 35.2%)	P value
Age	64.6 ± 14.5	60.3 ± 11.9	72.5 ± 15.3	<.001
Male	101 (71.1%)	68 (73.9%)	33 (66.0%)	.424
Hypertension	65 (45.8%)	33 (35.9%)	32 (64.0%)	.002
DM	38 (26.8%)	20 (21.7%)	18 (36.0%)	.102
QRS duration	157.9 ± 23.3	155.6 ± 24.3	162.0 ± 20.7	.124
NT-proBNP	3841.6 ± 4441.7	3765.2 ± 3761.2	3982.2 ± 5474.4	.783
NS-VT	85 (59.9%)	56 (60.9%)	29 (58.0%)	.878
NYHA				0.319
II	60 (42.3%)	38 (41.3%)	22 (44.0%)	
III	66 (46.5%)	46 (50.0%)	20 (40.0%)	
IV	16 (11.3%)	8 (8.7%)	8 (16.0%)	
Medication				
ACE inhibitors	79 (55.6%)	57 (62.0%)	22 (44.0%)	.06
ARB	28 (19.7%)	20 (21.7%)	8 (16.0%)	.548
Diuretics	134 (94.4%)	88 (95.7%)	46 (92.0%)	.603
β-blocker	135 (95.1%)	89 (96.7%)	46 (92.0%)	.401
LVEF by echo	29.2 ± 7.2	28.8 ± 6.9	30.0 ± 7.7	.348
LVEDV	289.8 ± 129.6	310.8 ± 139.7	251.1 ± 97.4	.008
LVESV	238.7 ± 118.9	259.0 ± 126.6	201.5 ± 92.2	.006
Scar burden	27.7 ± 13.6	26.4 ± 12.0	30.1 ± 15.9	.128
Systolic PSD	43.8 ± 22.4	42.5 ± 21.9	46.2 ± 23.1	.356
Systolic PBW	163.9 ± 91.8	152.0 ± 87.0	185.8 ± 96.2	.036
Diastolic PSD	54.4 ± 23.2	53.3 ± 23.9	56.3 ± 21.9	.458
Diastolic PBW	191.4 ± 90.0	179.3 ± 89.7	213.6 ± 86.1	.03
LV lead in scarred myocardium	1.8 ± 0.4	1.8 ± 0.4	1.9 ± 0.3	.027
Diastolic match	103 (72.5%)	63 (68.5%)	40 (80.0%)	.203
Systolic match	60 (42.3%)	30 (32.6%)	30 (60.0%)	.003
LVMD concordance				.004
both-match	42 (29.6%)	18 (19.6%)	24 (48.0%)	
one-match	79 (55.7%)	57 (61.9%)	22 (44.0%)	
neither match	21 (14.8%)	17 (18.5%)	4 (8.0%)	

ICM patients were all significant (all P<0.001).

In the univariate analysis for DCM patients, QRS duration (95%CI, 1.0-1.05,

P=0.014), NT-proBNP (95%CI, 0.0-0.61, P=0.026), non-sustained ventricular tachycardia (NS-VT) (95%CI, 0.1-0.64, P=0.004), Scar burden (95%CI, 0.93-1.0, P=0.029), all LVMD parameters (systolic PSD, 95%CI, 0.96-1.0, P=0.017; systolic PBW, 95%CI, 0.99-1.0, P=0.009; diastolic PSD, 95%CI, 0.95-0.99, P=0.003; diastolic PBW, 95%CI, 0.99-1.0, P=0.003), LVMD concordance (95%CI, 0.13-0.5, P<0.001), and LV lead in scarred myocardium (95%CI, 1.09-8.18, P=0.033) were statistically significant predictors of CRT response. However, for ICM patients, only diabetes mellitus (DM) (95%CI, 0.05-0.62, P=0.007), QRS duration (95%CI, 1.0-1.07, P=0.044), NS-VT (95%CI, 0.08-0.94, P=0.039), LVEDV (95%CI, 0.98-1.0, P=0.009), LVESV (95%CI, 0.98-1.0, P=0.009) were statistically significant predictors of CRT response, as shown in Table 2.4.

In the multivariate models for DCM patients, QRS duration, NT-proBNP, 3 LVMD parameters (systolic PBW: 95% CI, 0.98-1.00, P=0.041; diastolic PSD: 95% CI, 0.94-1.00, P = 0.041; diastolic PBW: 95% CI, 0.98-1.00, P = 0.028) and LVMD concordance (P<0.003 for all) were significant independent predictors of CRT response. For ICM patients, DM and LVESV were significant independent predictors of CRT response; however, all LVMD parameters and LVMD concordance were not significant. The results of the multivariate analysis were shown in Table 2.5, Table 2.6, Table 2.7, and Table 2.8.

Patients were divided into three groups based on the latest contraction or relaxation

Table 2.4
Univariate logistic regression analyses of DCM and ICM patients

	DCM			ICM		
Variables	**OR**	**95% CI**	***P* value**	**OR**	**95% CI**	***P* value**
Age	1	0.96-1.03	.962	1.03	0.97-1.1	.294
Male	0.81	0.31-2.1	.66	1.07	0.33-3.45	.914
Hypertension	0.77	0.32-1.82	.546	0.44	0.13-1.47	.182
DM	1.07	0.39-2.94	.894	0.17	0.05-0.62	.007
QRS duration	1.02	1.0-1.05	.014	1.03	1.0-1.07	.044
NT-proBNP	0.02	0.0-0.61	.026	0.15	0.0-9.53	.371
NS-VT	0.25	0.1-0.64	.004	0.28	0.08-0.94	.039
NYHA						
II			.037			.191
III	1.68	0.34-8.35	.526	2.14	0.41-11.16	.366
IV	0.504	0.108-2.361	.385	0.66	0.13-3.47	.630
LVEF by Echo	0.97	0.92-1.04	.404	1.02	0.94-1.09	.678
LVEDV	1	1.0-1.0	.438	0.99	0.98-1.0	.009
LVESV	1	1.0-1.0	.422	0.99	0.98-1.0	.009
Scar burden	0.96	0.93-1.0	.029	0.97	0.93-1.0	.075
Systolic PSD	0.98	0.96-1.0	.017	0.98	0.95-1.0	.064
Systolic PBW	0.99	0.99-1.0	.009	1	0.99-1.0	.107
Diastolic PSD	0.97	0.95-0.99	.003	0.97	0.95-1.0	.056
Diastolic PBW	0.99	0.99-1.0	.003	1	0.99-1.0	.171
LVMD concordance						
both-match			.000			.364
one-match	127.50	10.48-1551.48	.000	5.00	0.45-55.63	.190
neither match	11.93	2.49-57.28	.002	3.00	0.27-33.49	.372
LV lead in scarred myocardium	2.99	1.09-8.18	.033	3.9	0.38-40.37	.254

segment at the LV lead location: patients whose LV lead was concordant or adjacent to the latest contraction and relaxation segment (both-match: DCM, n=18; ICM, n=24), and patients whose LV lead was concordant or adjacent to the latest contraction or relaxation segment (one-match: DCM, n=57; ICM, n=22), and patients whose LV lead was neither concordant nor adjacent to the latest contraction or relaxation segment (neither: DCM, n=17; ICM, n=4). The intra-group comparison

Table 2.5
Stepwise multivariate analysis for DCM and ICM patients including systolic PSD

	DCM			ICM		
Variables	**OR**	**95% CI**	***P* value**	**OR**	**95% CI**	***P* value**
DM				0.17	0.04-0.73	.017
QRS duration	1.03	1.00-1.06	.049			
NS-VT	0.48	0.13-1.77	.272			
NT-proBNP	1.00	1.00-1.00	.0			
LVESV				0.99	0.98-1.00	.019
NYHA (II)			.388			
NYHA (III)	1.40	0.15-12.70	.765			
NYHA (IV)	0.53	0.08-3.88	.539			
LVMD concordance						
both-match			.001			
one-match	531.97	12.73-22233	.001			
neither match	19.34	3.07-121.85	.020			
LV lead in scarred myocardium	2.54	0.53-12.09	.243			
Systolic PSD	0.97	0.94-1.00	.063	1.00	0.97-1.03	.990

revealed that the CRT response rate of DCM patients (94%, n=18) was much higher than ICM patients (62%, n=24) in the both-match group (P=0.016). There was no significant difference in the one-match group (P=0.363) and neither group (P=0.521) between DCM and ICM patients, as shown in Figure 2.8. For the inter-group comparison, Kruskal-Wallis H-test revealed that CRT response was significantly different in the three groups of DCM patients (P <0.001) but not in ICM patients (P = 0.383).

During the mean follow-up time of 39±24 months (IQR 19-55), 10 (10.87%) DCM patients and 9 (18%) ICM patients died. Kaplan-Meier survival curves showed significantly longer survival in DCM patients with the concordance between LV lead with the latest contraction and relaxation position (P = 0.050), as shown in Figure 2.9.

Table 2.6
Stepwise multivariate analysis for DCM and ICM patients including systolic PBW

	DCM			ICM		
Variables	**OR**	**95% CI**	***P* value**	**OR**	**95% CI**	***P* value**
DM				0.16	0.04-0.69	.014
QRS duration	1.03	1.00-1.06	.043			
NS-VT	0.55	0.15-2.04	.371			
NT-proBNP	1.00	1.00-1.00	.011			
LVESV				0.98	0.98-1.00	.014
NYHA (II)			.403			
NYHA (III)	1.38	0.15-12.72	.776			
NYHA (IV)	0.54	0.07-3.98	.547			
LVMD concordance						
both-match			.001			
one-match	635.05	12.08-28642	.001			
neither match	20.76	3.23-133.30	.001			
LV lead in scarred myocardium	2.48	0.50-12.40	.268			
Systolic PBW	0.99	0.98-1.00	.041	1.00	0.99-1.01	.689

However, there is no significant difference of survival time in ICM patients based on the concordance between LV lead and the latest contraction or relaxation position, as shown in Figure 2.10.

2.3.4 Discussion

The main finding of the present study was that systolic PBW, diastolic PSD and PBW were strong predictors of CRT response only in DCM patients. Furthermore, Kaplan-Meier analysis showed that the concordance of LV lead to the latest contraction and relaxation position were independent predictors of death from any cause and had

Table 2.7
Stepwise multivariate analysis for DCM and ICM patients including diastolic PSD

	DCM			ICM		
Variables	**OR**	**95% CI**	***P* value**	**OR**	**95% CI**	***P* value**
DM				0.18	0.04-0.80	.024
QRS duration	1.07	1.00-1.05	.068			
NS-VT	0.45	0.12-1.66	.231			
NT-proBNP	1.00	1.00-1.00	.013			
LVESV				0.99	0.98-1.00	.017
NYHA (II)			.373			
NYHA (III)	1.69	0.19-14.98	.638			
NYHA (IV)	0.61	0.08-4.26	.622			
LVMD concordance						
both-match			.001			
one-match	571.74	11.57-28252	.001			
neither match	18.07	2.88-113.28	.002			
LV lead in scarred myocardium	2.49	0.51-12.9	.257			
Diastolic PSD	0.97	0.94-1.00	.041	1.00	0.97-1.03	.882

Table 2.8
Stepwise multivariate analysis for DCM patients including diastolic PBW

	DCM			ICM		
Variables	**OR**	**95% CI**	***P* value**	**OR**	**95% CI**	***P* value**
DM				0.16	0.04-0.67	.013
QRS duration	1.03	1.00-1.06	.051			
NS-VT	0.50	0.13-1.86	.304			
NT-proBNP	1.00	1.00-1.00	.013			
LVESV				0.99	0.98-1.00	.013
NYHA (II)			.460			
NYHA (III)	1.59	0.17-14.81	.683			
NYHA (IV)	0.64	0.09-4.79	.666			
LVMD concordance						
both-match			.001			
one-match	659.19	13.59-31972	.001			
neither match	19.85	3.14-125.31	.011			
LV lead in scarred myocardium	2.07	0.41-10.54	.380			
Diastolic PSD	0.99	0.98-1.00	.028	1.00	0.99-1.01	.621

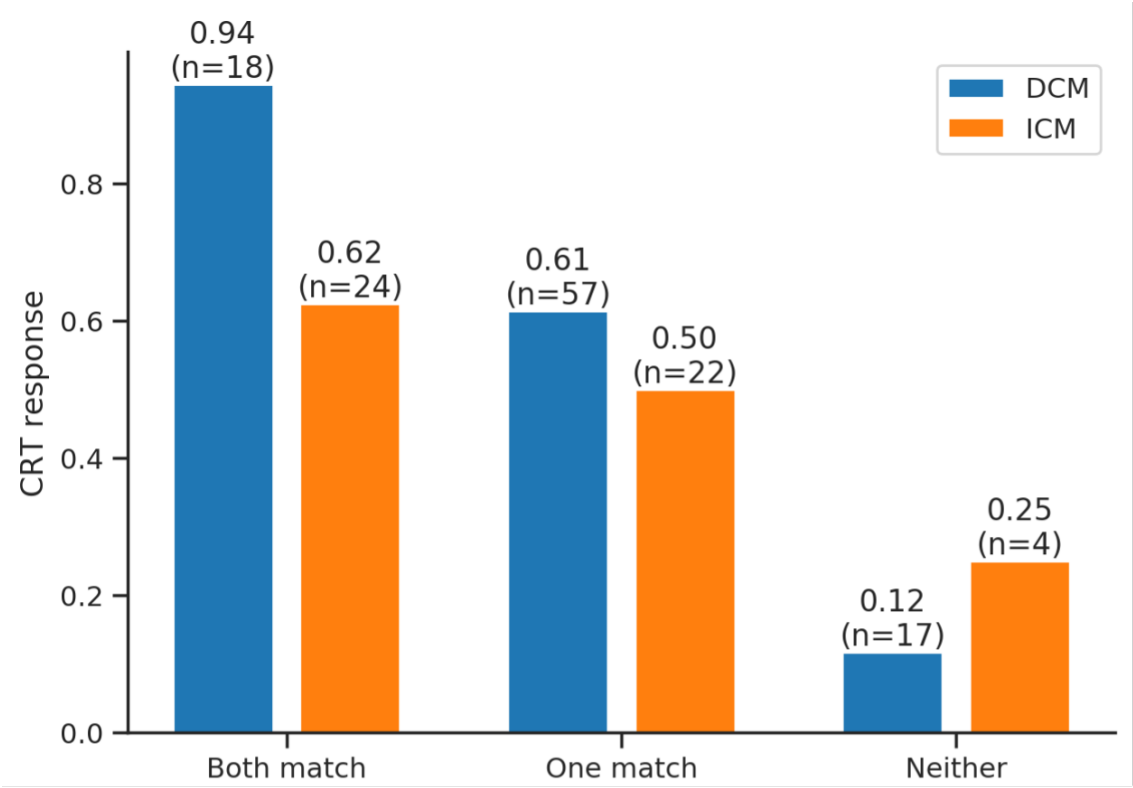

Figure 2.8: The CRT response rate in DCM or ICM patients among different groups.

significantly longer survival than LV lead only located in one latest position or none in DCM patients. Whether it is DCM or ICM, it is necessary to avoid placing the LV lead in a non-latest contraction or relaxation position whenever possible.

2.3.4.1 Predictive value of LVMD for CRT patient selection

Research on selecting appropriate patients for CRT with LVMD measured by gated SPECT MPI has been widely studied. In a study of 42 CRT patients, the receiver operating characteristic curve analysis showed that the optimal cutoff value of PSD and

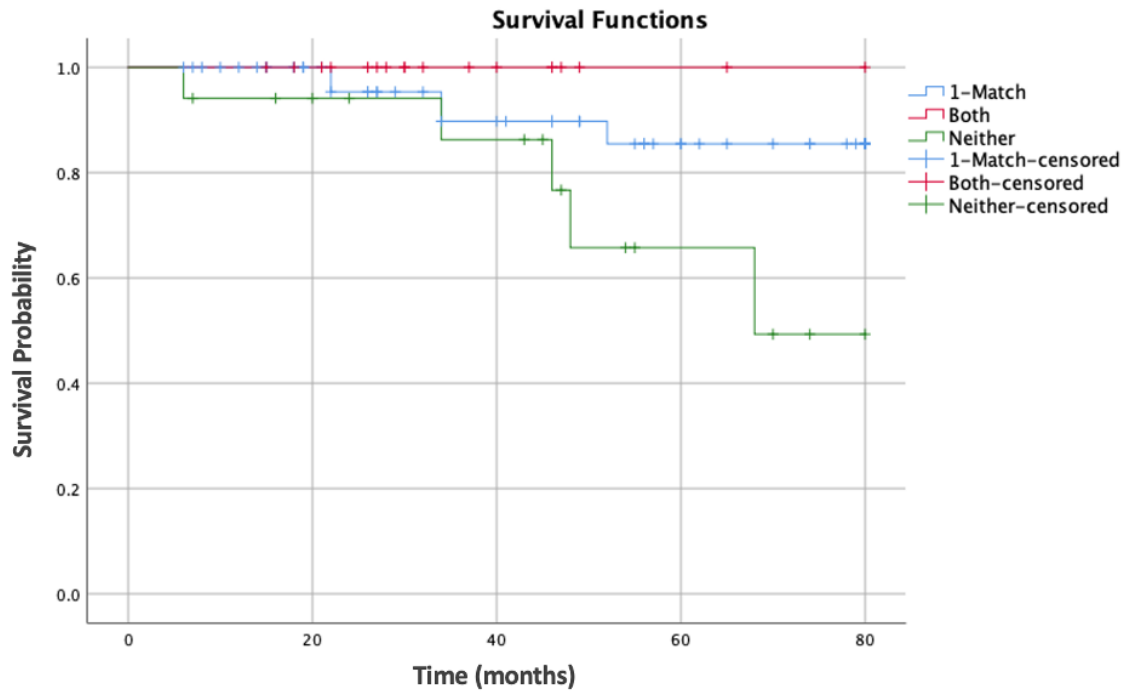

Figure 2.9: The Kaplan-Meier event-free survival curve of DCM patients (log-rank Chi-Square = 5.98, P = 0.050).

PBW were 43° (sensitivity and specificity of 70%) and 135°(sensitivity and specificity of 74%), respectively [2]. In a study with 324 consecutive patients with non-ICM CRT patients, it was demonstrated that systolic PSD, adjusted to age, hypertension, diabetes, aspirin, beta-blockers, diuretics, QRS, and EF, was an independent predictor of all-cause mortality (HR: 1.97, 95% CI: 1.06 – 3.66, P = 0.033) [149]. However, in a multi-center VISION-CRT clinical trial (n=195), it was found that the systolic LVMD did not have a predictive value for CRT response, but they did not discuss it based on different pathology [87]. Peix et al. [150] further analyzed part of the data from this clinical trial and found that CRT recipients with more dyssynchronous at baseline had significantly improved in non-ischemic patients with non-compaction

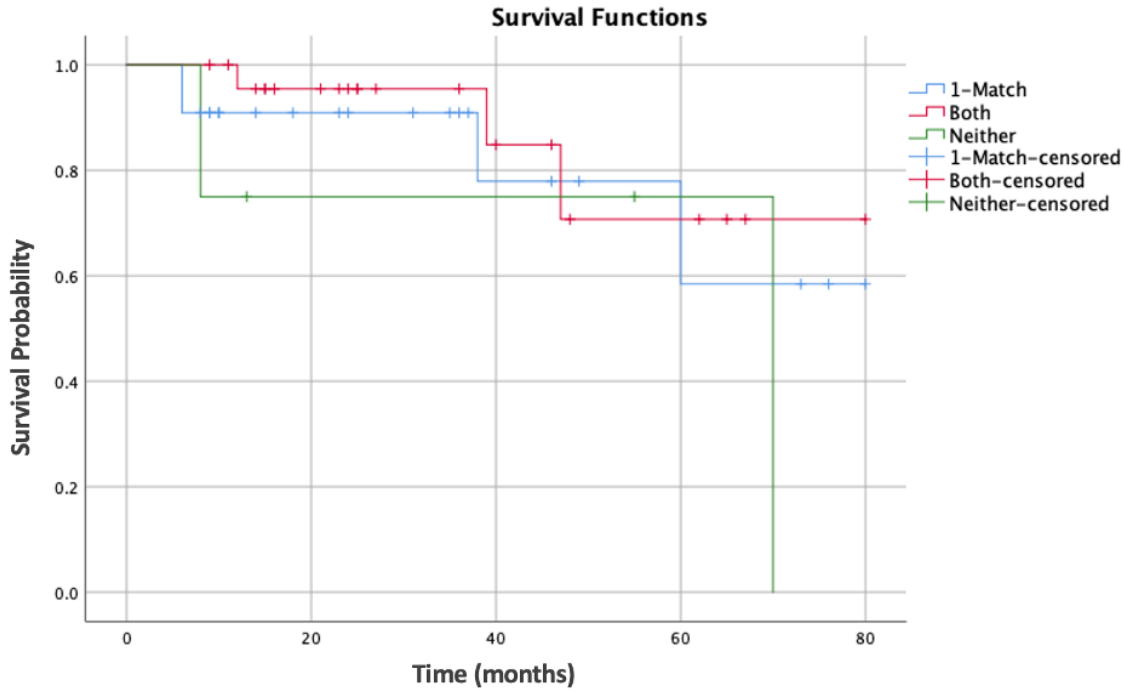

Figure 2.10: The Kaplan-Meier event-free survival curve of ICM patients (log-rank Chi-Square = 1.33, P = 0.514).

myocardium, whose PSD was reduced from $89.5 \pm 14.2°$ to $63.7 \pm 20.5°$ (P = 0.028).

For DCM patients, Henneman et al. [2] demonstrated that baseline systolic LVMD could be used to predict CRT response by the cutoff value of 43° for PSD with 74% sensitivity and specificity and 135° for PBW with 70% sensitivity and specificity. Wang et al. [146] found that systolic and diastolic LVMD both have predictive value for CRT patient selection in 84 DCM patients (systolic PSD: 95% CI 0.92-1.00, P = 0.043; systolic PBW: 95% CI 0.99-1.00, P=0.038; diastolic PSD: 95% CI 0.94 – 1.00, P=0.032; diastolic PBW: 95% CI 0.99 – 1.00, P=0.024). Similar results were found in our study that systolic PBW (95% CI 0.98-1.00, P=0.041), diastolic PBW (95% CI 0.98-1.00, P=0.028), and diastolic PSD (95% CI 0.94-1.00, P=0.041) were

independent significant predictors for CRT patient selection, except for systolic PSD (95% CI 0.94-1.00, P=0.063), but its P-value is still very close to 0.05.

For ICM patients, the presence of transmural scar tissue, which may affect the measurement of LVMD [151], often resulted in nonresponse to CRT [152]. However, few studies have been done on the predictive value of LVMD for CRT in ICM patients. A study found that the difference between stress LVMD and rest LVMD was an independent predictor instead of rest LVMD for all-cause mortality in ICM patients [153]; however, not all CRT patients receive stress gated SPECT MPI. Our study demonstrated that both systolic and diastolic LVMD were not independent predictive factors for CRT response. This might be due to the presence of hibernating myocardium or severely scarred and dysfunctional myocardium, which requires further evaluation [153].

2.3.4.2 LVMD to guide CRT lead placement

The optimal LV lead position has been suggested to be the latest or adjacent to the latest segment mechanical activation [43]. In a study with 90 CRT patients, the patients with a concordant LV lead position (the LV lead placed in the site of the latest mechanical activation measured by SPECT MPI) had significant improvement in LV volumes and LV systolic function than the patients with a discordant LV lead position (79% vs. 26%, P<0.01) [41].

For DCM patients, the CRT response could be increased when the LV lead is placed in the latest contraction and relaxation segment [146], which was proved in our study among 92 DCM patients. For ICM patients, a study with 64 CRT patients found that systolic PSD and PBW were significant factors to differentiate wide QRS duration ($\geq$ 150ms) with narrow QRS duration (120$-$150ms) among 47 DCM patients, and there were no similar results in ICM patients (n=17) [42]. In our study, both systolic and diastolic LVMD concordance between the latest activation segments and LV lead position was not independent predictive factors for CRT response. This finding was not surprising because the scar location might affect the latest mechanical activation due to the delayed electrical activation/conduction that might interfere with myocardial scar [42]. Furthermore, It showed a weak predictive value for CRT response in ICM patients by the concordance of the LV lead with the latest contraction or relaxation position, which was totally different compared with DCM.

2.3.4.3 LVMD in different pathophysiology of heart failure

Compared with DCM patients, poor predictive performance in ICM patients is due to the global scar burden, multiple scar segments, and regional ischemia, which may affect the remodeling response to biventricular pacing [67]. The contractility of myocardial scar tissue is impaired. Due to its electrophysiological inertia, it destroys the depolarizing waves from the adjacent myocardium, thereby prolonging the activation

time of the ventricles [67]. In addition, the presence of scar tissue means that the availability of recruitable contractile cardiomyocytes is reduced to bolster myocardial pump and LV hemodynamics [67]. Therefore, placing the LV lead on or adjacent to a scar or ischemia may have a poor effect. These results indicate that routine ischemia assessment before CRT device implantation may help identify CRT responders and help guide the placement of LV lead.

2.3.4.4 Study limitations

The main study limitation was the small number of retrospective patients, which limited our findings' statistical analysis and generalizability. Using two different imaging modalities to identify the latest contraction or relaxation segments by SPECT MPI and the location of LV lead by coronary venography limited the granularity that can describe the location and consistency of LV lead. However, this definition method has gained wide acceptance [64, 65, 67].

2.4 Conclusion

The role of MPI in heart failure is already known in light of the functional and phase analysis parameters. This chapter demonstrates that LV remodeling can be assessed

by shape parameters obtained with gated SPECT. In particular, in our sample, ESE was confirmed to be an independent predictive variable for CRT super-response and provides incremental value over existing clinical and nuclear imaging variables.

This study demonstrates that systolic and diastolic LVMD, and concordance between LV lead with the latest contraction or relaxation segment were independent predictive variables for CRT patient selection. Compared with ICM patients, systolic PBW, diastolic PBW and PSD have better predictive and prognostic values for the CRT response in DCM patients. Placing the LV lead on or adjacent to the latest contraction and relaxation position can improve the clinical outcomes of DCM patients, but it does not apply to ICM patients.

Chapter 3

Clinically explainable new mechanical dyssynchrony parameters by autoencoder

3.1 Introduction

Left ventricular mechanical dyssynchrony (LVMD) of gated single-photon emission computed tomography (SPECT) myocardial perfusion imaging (MPI) has shown significant value for CRT patient selection and prognosis [1, 2, 3, 37, 143]. However, existing statistical predictors characterizing LVMD such as phase standard deviation

(PSD) and phase bandwidth (PBW) are easily affected by the outliers of phase measurement and have been reported to have significant limitations, which may influence the assessment of clinical values of LVMD [154, 155, 156], and therefore could not predict the response to CRT in several studies [43, 86, 87].

Machine learning enables computers to learn and develop rules without having to be instructed by human programmers at every step of the way [157]. Deep learning as a powerful new tool combines many linear and nonlinear transformations to obtain a more comprehensive and useful representation of data [158]. It has achieved breakthrough applications in lesion detection and disease classification by absorbing the image measurement engineering directly into a learning step while processing the data in its natural form [158, 159, 160, 161]. Betancur et al. [104] presented the effectiveness of using deep neural networks for feature extraction in gated SPECT MPI and prediction of obstructive CAD. Xu et al. [162] demonstrated that unsupervised feature extraction by deep learning (single-layer network of K-means centroids, accuracy 93.65%) was as effective as a supervised method (fully convolution neural network, accuracy 94.52%) in the classification of histopathology images. In this study, we aimed to discover new predictors by deep learning from LVMD measured on gated SPECT MPI for CRT patient selection.

3.2 Methods

3.2.1 Patient population for training

One hundred and fifty-seven CRT patients with gated resting SPECT MPI were enrolled at nine medical centers in China from July 2008 to July 2020. The enrollment criteria included (1) LVEF measured by echocardiography $\leq 35\%$; (2) QRS duration ≥ 120 ms; (3) New York Heart Association (NYHA) functional class from II to IV; and (4) optimal medical therapy for at least 3 months before CRT implantation. Patients with atrial fibrillation or right bundle branch block were excluded.

All the patients had baseline characteristics, pre-CRT echocardiography, pre-CRT resting gated SPECT MPI, and 6 months follow-up echocardiography. The study was approved by the Institutional Ethical Committee of the First Affiliated Hospital of Nanjing Medical University, and informed consent was obtained from all patients.

3.2.2 Evaluation of LV function by echocardiography

Echocardiography data of all patients were assessed by experienced ultrasound experts blinded to any clinical data and MPI data before and 6 months after CRT. LVEF

was measured by the 2-dimensional modified biplane Simpson method. An increase in LVEF $> 5\%$ at 6-month follow-up echocardiography is considered as a positive mechanical response to CRT [19, 163].

3.2.3 Gated SPECT MPI acquisition and quantification

Gated SPECT MPI was performed by SPECT systems with a low-energy, general-purpose collimator within seven days before CRT implantation. Resting gated SPECT scan was performed 60-90 minutes after injection of 25-30 mCi of ^{99m}Tc-MIBI. Images were acquired by 1-day resting gated SPECT MPI protocol with a dual-headed or triple-head camera by 180° orbits with a complimentary 8 frames ECG-gating, according to the current guideline [164]. When the gated SPECT MPI was acquired, the photoelectric window of ^{99m}Tc was set to a 20% energy window centered over 140 keV. All the images were reconstructed by the OSEM method from Emory Reconstruction Toolbox (ERTb2, Atlanta, GA) with 3 iterations, 10 subsets, power 10, and a cutoff frequency of 0.3 cycles/mm. Short-axis images were generated by Emory Cardiac Toolbox (ECTb4, Atlanta, GA) for automated measurement of LV function and LVMD.

LVMD is measured by a phase analysis technique with the following three steps: (1) extracting three-dimensional maximal count myocardial perfusion from the short axis

slices by sampling the myocardial wall; (2) calculating the systolic phase angles by the 1harmonic Fourier approximation, which measures the change of counts in LV myocardium in an R-R cardiac cycle; and (3) generating polarmaps based on the LV phase angles in the LV myocardium [72, 148].

3.2.4 Extraction of new parameters by autoencoder techniques

Autoencoder (AE) is an unsupervised learning technique in which we use neural networks to accomplish the task of representation learning [165]. Specifically, the AE architecture forces the compressed knowledge to represent the original by copying the input to the output, compressing the input to a latent space representation and then reconstructing the output from this representation [165]. It has an input layer, an output layer, and one or more hidden layers connecting them. The input layer and the output layer have the same number of nodes. During the training process, AE sets the target value equal to the input value and adjusts the model parameters by applying backpropagation [166]. The network is arranged in two stages, the encoder and the decoder. The encoder connects directly to the pixels of inputted images through a linear layer and compresses the high-dimensional input images into the hidden layer, which has a lower dimension than the input images and can be used as features of the input images. The decoder attempts to reconstruct the input images

from the generated features. The AE model learns to recognize key image features and reconstruct the input by minimizing the error between the reconstructed output and input image.

In this study, a multi-layer AE with one input layer, five fully connected hidden layers, and one output layer was used to train the model, and the middle-most hidden layer was used to represent the features of LVMD polarmaps. The overall process of the AE model training, including the detailed architecture of our AE model, and the process of predicting CRT response with AE-extracted parameters is illustrated in Figure 3.1. The gradient is calculated through a mean squared error loss function, and the parameters are updated by an Adam optimizer. Early stopping is used to avoid overfitting when the loss stops decreasing. The AE model was implemented in the Python programming language by the PyTorch deep learning toolkit (version 1.3.1) [167]. Model training was performed on graphical processor units (TITAN Xp, NVIDIA, Santa Clara, California).

3.2.5 Statistical analysis

Discrete variables of the baseline characteristics were expressed in number and percentage and tested with the χ^2 test. Continuous variables were expressed as mean $\pm$ standard deviation and tested with the Student t-test. The univariate logistic

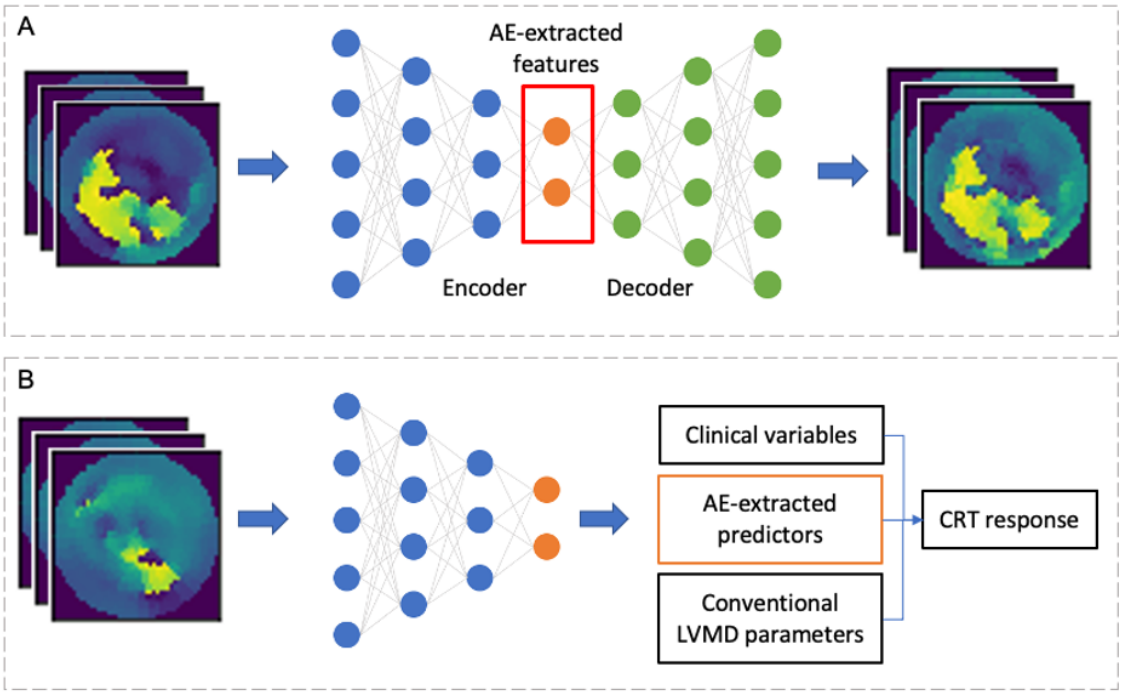

Figure 3.1: Training an autoencoder (AE) model from left-ventricular mechanical dyssynchrony (LVMD) (**A**) and building a prediction model (**B**) for CRT response. In (**A**), the multi-layer AE model is applied to the systolic phase polarmaps to extract compressed features and reduce the dimensions. In (**B**), clinical variables, AE-extracted predictors, and conventional LVMD parameters (phase standard deviation and bandwidth) are used to build the prediction model for CRT response.

regression analysis was applied to estimate the predictive values of baseline clinical variables, conventional LVMD parameters (PSD and PBW), and 32 AE-extracted LVMD parameters for CRT response. To overcome the curse of dimensionality and collinearity, only significant features in the univariate analysis were selected, and the Pearson correlation coefficient (PCC) analysis was further applied to exclude the variables that were highly correlated with each other. Subsequent multivariate analysis was performed to identify the predictive values for CRT response. Variables with $P < .05$ were considered statistically significant. PCC was also used to determine whether

there were significant correlations between the selected AE-extracted predictors and clinical parameters, i.e., LVMD parameters (PSD and PBW), as well as to rank the importance of all variables in the prediction of the CRT response. The Akaike information criterion (AIC) and likelihood ratio (LR) test were used to determine whether the prediction model with AE-extracted predictors is statistically significantly favored over the model with significant clinical parameters. The predictive performances of all significant variables were evaluated by the area under the curve (AUC) of the receiver operating characteristic (ROC) of binary logistic regression. Statistical analysis was performed by IBM SPSS Statistics software version 26 (SPSS Inc, Chicago, Illinois) and Python Statsmodels package [132].

3.2.6 External validation

In order to confirm the generalizability of the method proposed in this paper, the data from the multicenter VISION-CRT trial was used for external validation. The complete study design and preliminary results of VISION-CRT were previously published [87, 114, 131]. Because of the data error (n = 22), death of patients before follow-up (n = 11), and extremely small heart (ESV = 8ml) as outliner (n = 1), 165 of 199 patients were selected as the external validation dataset for this study, which was processed in the same way as in [114]. However, because of the mismatch of patient IDs in the clinical records and SPECT MPI (n = 17), an external validation dataset

of 148 cases (responders: n = 66, 44.6%) containing the complete records and SPECT MPIs was finally obtained. Due to the lack of pre- and post-CRT echocardiographic data, the CRT response in the external validation dataset was defined as a $> 5\%$ increase in LVEF measured by gated SPECT MPI at 6-month follow-up compared to pre-CRT SPECT MPI. This definition of CRT response was calculated in the same way as the definition in the training dataset, except for the modality used to measure LVEF (training dataset: echo, external validation dataset: gated SPECT MPI). Clinical variables (e.g., gender, age, NYHA), ECG parameters (QRS duration, LBBB), and LV measurements from gated SPECT MPI at baseline and 6-month follow-up (e.g., LVEF, ESV) were included in this study.

3.2.7 Interpretability of AE-extracted feature

To determine the attributes' contribution in the original systolic phase polarmap image to the value of the AE-extracted LVMD predictors, a heatmap of weights was used to map directly from the input LVMD polarmap to each AE feature extracted from the hidden layers.

We inputted an image into our AE network and visualized the network diagram by "unrolling" the pixel into a single column of neurons, as shown in Figure 3.1. The AE model "forces" the network to learn the features of the image itself. The weights

of each neuron in the input layer are connected to each AE feature through multiple hidden layers. We can explain these weights as forming templates of the output features. If an image is largely sympathetic to a filter, the image will generate high activation in a particular neuron in the input layer. Thus, the neurons in the hidden layer reflect the presence of those features in the original image. In the output layer, a single neuron, corresponding to the different AE features, is a weighted combination of those previously hidden activations. Therefore, we visualized the weights in the input layer corresponding to the neurons in the hidden layer that were selected as AE-extracted features.

3.3 Results

A total of 157 patients underwent CRT, but complete clinical assessment data, baseline SPECT MPI, and 6-month follow-up data were obtained in 130 patients. The baseline characteristics are shown in Table 3.1. The average age was 62.3 ± 12.1 years, 91 (70.0%) patients were male, and 67 (51.9%) patients were classified as NYHA functional class III. After a 6-month follow-up, 89 of the 130 patients (68.5%) were considered CRT responders, and the rest were considered non-responders to CRT. Significant differences between EDV (286.0 ± 102.5 vs 349.0 ± 156.8, P = .008) and ESV (228.3 ± 97.3 vs 282.0 ± 147.6, P = .016) were noted between responders and non-responders. However, the two groups had no significant differences in baseline

Table 3.1
Baseline characteristics of the enrolled patients

Variables	All (n=130)	Response (n=89, 68.5%)	Non-response (n=41, 31.5%)	P value
Age	62.3 ± 12.1	63.4 ± 11.0	59.9 ± 13.8	.128
CKD	9 (6.9%)	6 (6.7%)	3 (7.3%)	.801
DM	28 (21.5%)	18 (20.2%)	10 (24.2%)	.759
QRS duration	151.5 ± 21.2	153.7 ± 19.7	146.7 ± 23.4	.084
LVEDV	305.9 ± 126.4	286.0 ± 102.5	349.0 ± 158.6	.008
LVESV	245.2 ± 118.2	228.3 ± 97.3	282.0 ± 147.6	.016
LVEF	21.5 ± 7.8	21.7 ± 7.5	21.1 ± 8.3	.680
Gender	91 (70.0%)	62 (69.7%)	29 (70.7%)	.934
NYHA				
II	43 (33.1%)	33 (37.1%)	10 (24.4%)	
III	67 (51.5%)	46 (51.7%)	21 (51.2%)	
IV	20 (15.4%)	10 (11.2%)	10 (24.4%)	
SRS	18.4 ± 9.8	17.4 ± 8.8	20.5 ± 11.2	.090
PBW	203.5 ± 73.9	205.4 ± 73.7	199.4 ± 74.2	.666
PSD	60.1 ± 18.5	60.2 ± 17.7	59.8 ± 19.9	.913

Data are expressed as mean ± SD or number (percentage)

PSD and PBW.

All 157 pre-CRT LVMD polarmaps were used to train the AE model for feature extraction. After the training, 32 features of LVMD were extracted from the hidden layers of the autoencoder model as the AE-extracted LVMD predictors.

Twenty-seven of the 157 subjects did not have a follow-up on their CRT response, so the AE-extracted predictors from phase polarmaps of the remaining 130 patients were analyzed. Only 4 of the 32 AE-extracted features showed statistical significance in the univariate analysis. As shown in Figure 3.2, these four AE-extracted LVMD

predictors had a strong correlation with each other (all PCC > 0.99, P values < .05), but they were not correlated with any clinical variables and conventional LVMD parameters (PSD and PBW). Only one AE-extracted LVMD predictor, which has the highest Pearson correlation with the CRT response (PCC = 0.20), was selected for the subsequent statistical analysis to characterize the polarmaps of LVMD.

In the univariate analysis, LVEDV (OR 1, 95% CI 0.99-1.00, P = .013), LVESV (OR 1, 95% CI 0.99-1.00, P = .023), NYHA (OR 0.56, 95% CI 0.32-0.99, P = .045), and the AE-extracted LVMD predictor (OR 2.00, 95% CI 1.08-3.67, P = .026) had significantly predictive values to CRT response, as shown in Table 3.2. Since there was a strong correlation between LVEDV and LVESV (PCC = 0.98, P values = .032), only the LVESV had a stronger correlation with CRT response than LVEDV (PCC = 0.51 vs PCC = 0.47) was included in the multivariate analysis. In the multivariate analysis, LVESV (OR 1.00, 95% CI 1.0-1.0, P = .013) and AE-extracted LVMD predictor (OR 1.11, 95% CI 1.02-1.23, P = .021) had significant predictive values for CRT response, as shown in Table 3.2.

In Figure 3.3, the fitting performance of the predictive model with the AE-extracted LVMD predictor (AIC 162.04) was better than the model with PBW (AIC 164.68). The AE-extracted LVMD predictor took incremental value over clinical variables (LR 5.52, P = .019) and clinical variables with PBW (LR 7.33, P = .007). In addition, the

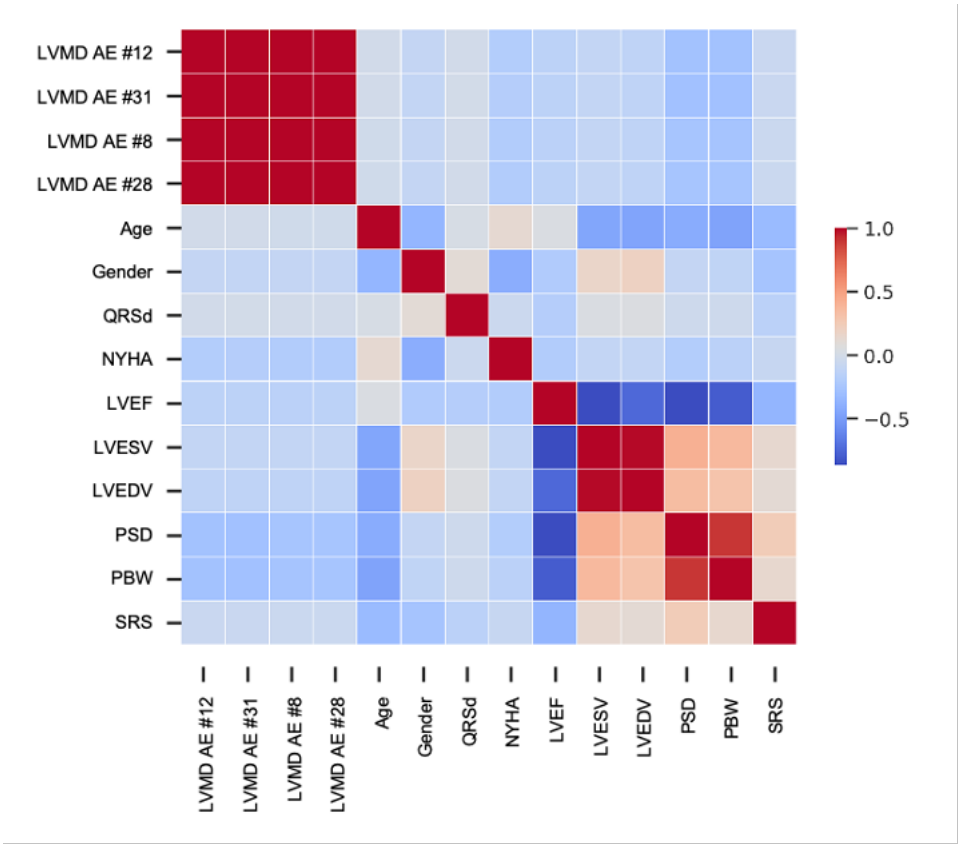

Figure 3.2: Pearson's correlations between clinical variables, phase standard deviation (PSD), phase bandwidth (PBW), and AE-extracted left ventricular mechanical dyssynchrony (LVMD) parameters. Only the AE-extracted LVMD parameters, which were significant in the univariate analysis, are displayed. There are strong correlations between these AE-extracted LVMD parameters (all Pearson correlation coefficient [PCC] > 0.99, P values $< .05$), so PCC between the significant AE-extracted LVMD parameters and the CRT response is further applied to select only one AE-extracted LVMD predictor (LVMD AE # 31), which has the highest correlation (PCC $= 0.20$) with the CRT response. This AE-extracted LVMD predictor is used in the subsequent statistical analysis.

AUCs of the clinical variables (95% CI 0.57-0.78, AUC 0.66), clinical variables combined with PBW (95% CI 0.60-0.80, AUC 0.69), clinical variables combined with the AE-extracted LVMD predictor (95% CI 0.61-0.81, AUC 0.72), and clinical variables combined with both PBW and the AE-extracted LVMD predictor (95% CI 0.64-0.83,

Table 3.2
Univariate and multivariate logistic regression analysis

	Univariate analysis			Multivariate analysis (AE #30)		
Variables	**OR**	**95% CI**	***P* value**	**OR**	**95% CI**	***P* value**
Age	1.02	0.99 - 1.06	.131			
CKD	0.92	0.22 - 3.86	.904			
DM	0.79	0.22 - 1.90	.592			
LVEDV	1	0.99 - 1.00	.013			
LVESV	1	0.99 - 1.00	.023	1.00	1.00 - 1.00	.013
Gender	0.95	0.42 - 2.14	.902			
NYHA	0.56	0.32 - 0.99	.045	0.89	0.80 - 1.00	0.052
PBW	1	1.0 - 1.01	.664			
PSD	1	0.98 - 1.02	.912			
QRSd	1.02	1.0 - 1.04	.086			
SRS	0.97	0.93 - 1.01	.091			
LVMD AE #12	2.00	1.08 - 3.67	.026	1.11	1.02 - 1.23	.021
LVMD AE #31	1.77	1.07 - 2.94	.026			
LVMD AE #8	1.38	1.04 - 1.84	.028			
LVMD AE #28	1.31	1.03 - 1.68	.028			

AUC 0.74) increased sequentially, as shown in Figure 3.4.

The well-trained model was also used in the external validation group to test the performance of the AE-extracted LVMD predictor. The baseline characteristic and statistical results have been previously published.35 It is worth noting that there is a big difference in the distribution of patient features between the external validation dataset and the training set. Examples include QRS duration (training set: response [n=89, 68.5%] vs. non-response[n=41, 31.5%]: 153.7±19.7 vs. 146.7±23.4; external validation set: response [n=66, 44.6%] vs. non-response [n=82, 55.4%]: 161.7±22.4, 160.0±27.4), PSD (training set: 60.2±17.7 vs. 59.8±.9; external validation set:

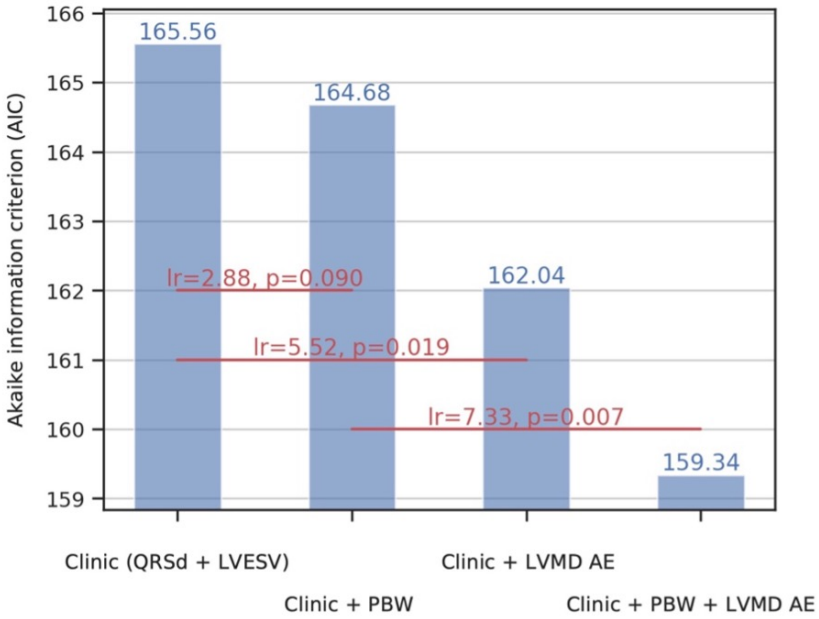

Figure 3.3: Fitting performance and incremental values of the AE-extracted LVMD predictor in the prediction of CRT response. Akaike information criterion (AIC) reflected the fitting performance of the model. The larger the value, the better the fitting performance of the model. The likelihood ratio test compared the goodness of fit of two nested models (two models were connected by a red line) and reflected the incremental predictive value of the newly added variables. AE-extracted LVMD had incremental predictive value over both the clinic parameters (LR = 5.52, P = .019) and the combination of clinical variables and PBW (LR = 7.33, P = .007).

46.8±21.0 vs. 50.6±19.6), and PBW (training set: 205.4±73.7 vs. 199.4±74.2; external validation set: 142.4±76.0 vs. 159.9±73.0). In the univariate analysis, MI (OR 0.2, 95% CI 0.07-0.55, P=0.002), CAD (OR 0.3, 95% CI 0.14 – 0.65, P=0.002), EDV (OR 1, 95% CI 0.99 - 1.00, P=0.013), ACEI or ARB (OR 3.44, 95% CI 1.3 – 9.13, P=0.013), scar score (OR 0.96, 95% CI 0.94 – 0.99, P=0.016) showed significant predictive values to CRT response. The AE-extracted predictor showed significant predictive value at the significance level of 0.1 (95% CI 0.95-2.12, P=0.092), and it alone achieved an AUC of 0.57 (95% CI 0.48-0.66).

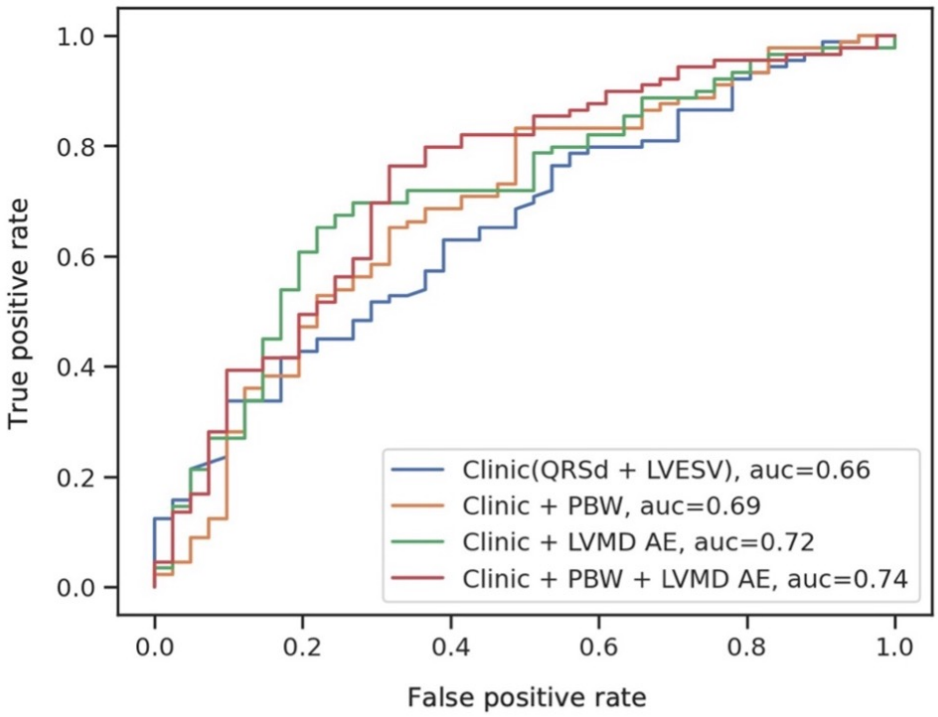

Figure 3.4: Receiver-operating characteristic curves to predict the CRT response.

Figure 3.5 illustrates four patient examples. According to the conventional LVMD parameters (PSD $> 21°$ and PBW $> 112°$; 6 PSD$> 43°$ and PBW $> 128°$; 7 PSD $> 43°$ and PBW $> 135°$[10]), A and C might be responders to CRT, and B and D might be non-responders to CRT. However, post-CRT follow-ups showed that A and B were CRT responders, and C and D were CRT non-responders; the AE-extracted feature successfully predicted the CRT response for these patients.

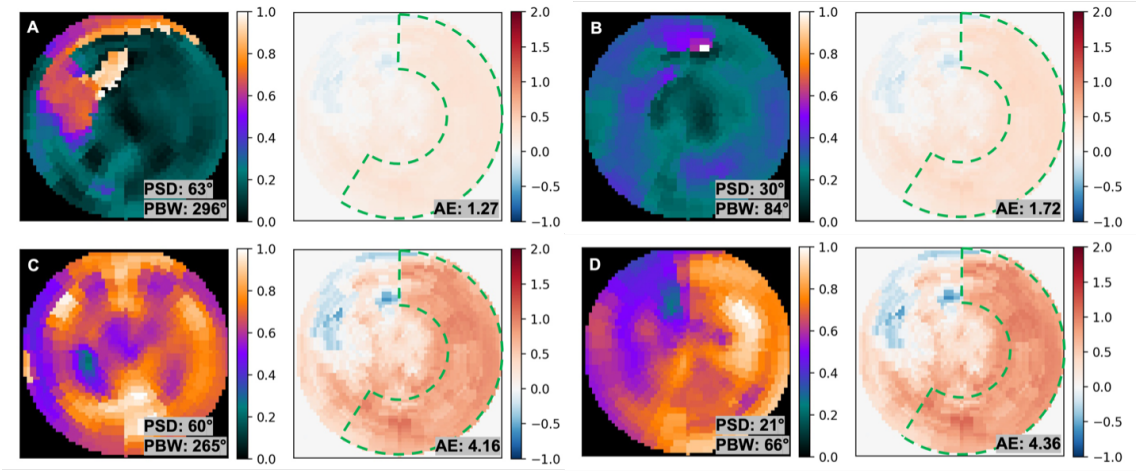

Figure 3.5: Illustrations of PSD and PBW vs AE-extracted LVMD predictor for 4 patients (Patients A and B: CRT non-responders; Patient C and D: CRT responders). The left graph for each patient is the systolic phase polarmap and the right graph is the weight heatmap. For the weight heatmap, the higher saturation of the color indicates the higher absolute value of the weights in the deep neural networks. Red and blue colors indicate positive and negative values, respectively. The green dashed box indicates the half-moon-shaped region, including part of the anterior wall, and the complete lateral and inferior walls, excluding the septum and the apex.

3.4 Discussion

3.4.1 Limitations of conventional LVMD parameters

Early retrospective studies suggested a significant association between baseline LVMD and CRT response[1, 2, 3, 37, 168]. Three studies proposed three different PBW thresholds (112° vs. 128° vs. 135°) for the prediction of CRT response, and they all claimed to have good prediction results (sensitivity, 72% vs. 86% vs. 70%, specificity, 70% vs. 80% vs. 70%); it is worth noting that these thresholds were all defined from

small sample populations (n=30, 32, 42, respectively) [1, 2, 3]. PSD had similar results in these three articles. However, the data from GUIDE-CRT clinical trial showed that PSD and PBW were not associated with volumetric CRT response, referred to as a reduction of ≥15% in LVESV [14, 43]. Another multicenter trial (VISION-CRT) showed that baseline PSD and PBW were not associated with the CRT response, which was defined by any improvement in one or more of the following: decrease of ≥ 1 in NYHA class, an increase of $\geq 5\%$ in LVEF, a decrease of $\geq 15\%$ in left ventricular end-systolic volume (LVESV), or decrease of ≥ 5 points in Minnesota Living With Heart Failure Questionnaire [87]. Gendre et al. [86] demonstrated that baseline LVMD parameters, including PSD and PBW, could not predict the response to CRT defined by a reduction of LVESV $\geq 15\%$ or improve peak VO2 $\geq 10\%$, even though the study was a single-center study with a small number of patients (n = 42). Zhang et al. [43] also found similar results in a multicenter study with 79 CRT patients, in which a reduction of LVESV $\geq 15\%$ was used to define the volumetric response to CRT. Existing global parameters (PSD and PBW) characterizing LVMD are easily affected by the outliers of phase measurement [154, 155, 156]. PSD may be deceptive for characterizing the widely distributed and multi-modal distributions in phase histograms; PBW includes almost the entire distribution range of the histogram (95%) [78, 156]. The statistical analysis relies heavily on pre-assumed relationships between factors, and there are problems related to identifying appropriate data, processing interconnected rather than independent factors, and even violating assumptions [169].

A method that comprehensively considers the relationship between variables and extracts potential, new and more predictive features for CRT is needed.

3.4.2 Advantages and interpretability of AE model for feature learning

Compared with conventional statistical methods, data-driven feature learning through deep learning has higher performance. The advantage of deep learning for feature learning is a layered architecture similar to the human brain [170]. Through deep learning, simple features are extracted from the raw data, and then more complex features are learned through multiple layers. Finally, a considerable number of robust features are generated through multiple iterations of learning. Specifically, feature learning is classified into two categories, supervised learning and unsupervised learning.

In supervised learning, labeled data are forwarded from the input to the output for prediction. Backpropagation is used to optimize the parameters of the deep learning model by minimizing the cost function between the target value and the predicted value. Betancur et al. [104] proposed a deep convolutional neural network for predicting the probability of obstructive coronary artery disease in the left anterior descending artery, left circumflex artery, and right coronary artery that had

better per-patient sensitivity (from 79.8% to 82.3%, $p<0.05$) and per-vessel sensitivity (from 64.4% to 69.8%, $p<0.01$) than total perfusion deficit. Such end-to-end supervised learning neural network avoids the tricky problem of determining which components are needed to perform a learning task and how those components interact, but also brings a lack of interpretability and requires a significant amount of data. In unsupervised learning, unlabeled data are used to learn new features and find new patterns on their own, which can yield undiscovered information that might require human intervention to understand the hidden patterns and correlate them with the domain knowledge. Cikes et al. [101] proposed an unsupervised approach to analyze the phenotype of heterogeneous HF by integrating clinical variables and eight echocardiographic descriptors (traces) extracted from full cardiac cycle echocardiographic images. They emphasized that their unsupervised method was not trained based on a priori knowledge, and the interpretability of their model was based on the distribution of existing prior variables in different phenogroups.

Interpretable machine learning approaches based on complex mathematical formulas are rendered black boxes by the complexity and scale of their structures [165, 171]. Some state-of-the-art models, including deep learning and ensemble models, limit the clinical actionability of model predictions due to the "black box" structure, which further undermines their usefulness to clinicians [172]. Heatmap of the weights used in this paper is a straightforwardly interpretable method that shows the relationship from the input LVMD polarmap, mapped to each AE-extracted predictor from

the hidden layer. The brightness signifies the weights associated with single filters' activations (a specific template) from the hidden layer.

Typically, LV lead of the CRT is implanted in the lateral wall or a region adjacent to the lateral wall, which can encompass the anterior or inferior walls of the left ventricle (depending on coronary sinus venous anatomy). Thus, the ideal site for LV lead placement could be in a half-moon-shaped region of the polar map, encompassing anterior, lateral, and inferior walls, while excluding the septum. Studies have indicated that LV lead placement in the apex is associated with increased risk of HF and death [4, 90, 173], and thus that is also excluded from this half-moon of the polar map. Therefore, ideal AE-extracted predictors of positive CRT response would align on the half-moon-shaped of the polar map.

As shown in Figure 3.5, this weight heatmap is "responsible" for classifying the half-moon shaped phase polarmap (roughly two thirds of a circle without the apex of the LV), and its goal is to output a high value for half-moon shaped polarmap and a low value for non-half-moon shaped polarmap. Suppose that we receive an input phase polarmap like Figure 3.5-D, we can anticipate that the neurons responsible for classifying half-moon shaped polarmap should have high values, because their weights are such that high weights tend to align with pixels tending to be high in half-moon shaped polarmap. For other non-half-moon shaped phase polarmap, such as Figure 3.5-A, most of the pixels would not line up with a half-moon shaped polar

map, so less overlap would negate high-valued pixels in those images by low weights. The better the input image matches this half-moon shaped template, the higher the AE score obtained. It can be observed that this half-moon shaped polarmap template has higher weights in the bright anterior, lateral, and inferior myocardial walls, and lower weights in the dark apical, septal, and anteroseptal walls, which is consistent to clinical experience. Accordingly, when we design the CRT predictor based on LVMD, we should put more focus on the anterior, lateral, and inferior myocardial walls.

3.5 Conclusion and future work

In this chapter, we proposed and externally validated the use of an unsupervised learning algorithm, autoencoder, for feature learning from SPECT MPI to predict CRT response. Our new AE-extracted predictor in this study is significantly different from conventional LVMD parameters. This data-driven approach of unsupervised learning requires only unlabeled training images, is able to learn non-linear relationships and avoids the loss of important information in feature extraction. The model has been tested in an external validation dataset, and the results seen here are reproducible and have significant predictive value for CRT response. The performance of AE-extracted predictors can be improved with increase of the patient sample size. More importantly, unlike the global variables PSD and PBW, AE-extracted feature assigns higher weights to anterior, lateral, and inferior myocardial walls of interest,

which are consistent with the recommended pacing sites of the LV lead in clinical practice.

Several limitations of this study should be acknowledged. First, this study enrolled a relatively small number of patients from multiple medical centers with the inherent limitation of such a study design. The performance and feasibility of the data-driven system may be affected by the quality of the data. Second, the lack of post-CRT SPECT MPI in the training set and the lack of pre- and post-CRT echocardiography in the external validation dataset led us to use the same threshold (a $>$ 5% increase LVEF) but by different imaging modalities (training: echo vs external validation: gated SPECT MPI) to define the CRT response. Although many studies demonstrated a good correlation between LVEF measured by gated SPECT MPI and echocardiography [174, 175, 176, 177], the different definitions of CRT response between the two trials may introduce bias in the prediction performance. Moreover, some clinical parameters in the training dataset were not available in the external validation dataset (e.g., CKD), and the distributions of the patient characteristics (e.g., QRS morphology, QRS duration, PSD, and PBW) were substantially different between the training and external validation dataset. Therefore, the performances of the AE-extracted predictor were different between the two datasets.

Chapter 4

Knowledge discovery in electrical dyssynchrony from gated SPECT MPI for CRT patient selection

chezhao@mtu.edu

4.1 Introduction

The current CRT guidelines for CRT patient selection primarily rely on ECG-based criteria, namely QRS duration and morphology [178]. While QRS duration has

demonstrated clinical value in predicting CRT response, it lacks the finesse to predict response on a patient-specific level accurately [178]. Multiple QRS cutoff values have been considered in different trials and studies, and the electrical LBBB pattern is widely accepted as a strong predictor of CRT response. Among LBBB patients, CRT response improves as QRS duration increases; on the other hand, the benefit of CRT starts to emerge in non-LBBB patients when QRS duration is $\geq$ 160 ms [178, 179]. However, ECG is not always effective in measuring the presence or severity of electrical dyssynchrony in all ventricular segments; and only significant myocardial masses can affect QRS morphology and duration [180]. Moreover, QRS duration alone is not specific enough to characterize exact electrical and mechanical activation patterns [181]. Even in cases of LBBB, different and heterogeneous electrical and mechanical activation patterns can exist despite similar QRS morphology and duration [182, 183]. Therefore, researchers are seeking more accurate and patient-specific predictors beyond QRS duration and morphology.

Transfer learning is a powerful technique that leverages empirical knowledge gained from solving one problem to solve a related but different problem. In medical research, transfer learning has been widely adopted due to the limited availability of annotated medical images and the high cost of obtaining annotations [**?**]. The general process of transfer learning involves pre-training a deep neural network on a large dataset and then fine-tuning the network on a smaller target dataset. This approach enables the transfer of knowledge learned from the source dataset to the target dataset, resulting

in improved performance with less data [**?**]. This allows the data of arrhythmia patients in large public databases to be better generalized and used for CRT patient selection.

In this chapter, we first represent the ECG signals obtained from the MIT-BIH dataset with two-dimensional images by the short-time Fourier transform (STFT) technique, using a transfer learning approach to extract the input image features from the convolutional neural network (CNN) model (ResNet). Next, we fine-tuned the pre-trained models to extract features from the ECG of CRT data. We used them as inputs to classifiers such as logistic regression, support vector machine (SVM), and random forest (RF) to classify CRT patients based on ECG data, respectively.

4.2 Methods

In this study, the 1-D ECG signal was reconstructed as a 2-D time-frequency spectrogram image for obtaining information on time, frequency and energy of the heartbeats. Figure 4.1 shows the flowchart of the proposed method.

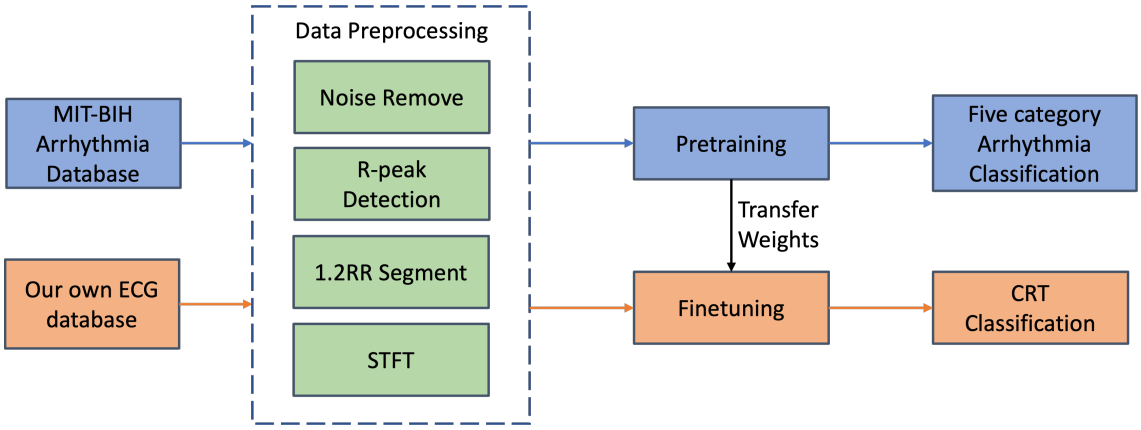

Figure 4.1: Visualization of transfer learning in this work. The process is divided into 4 steps: (1) Data preprocessing for both MIT-BIH arrhythmia database and our own dataset to convert 1D ECG signals to 2D images (2) deep convolutional neural network (CNN) is pretrained on the MIT-BIH arrhythmia database for a selected pretraining objective, e.g. classification of arrhythmia; (3) the pretrained weights are used as initial weights of a new CNN; (4) this CNN is finetuned on our own database to predict CRT response.

4.2.1 Data

The data used in this study is sourced from two separate databases. The first database is the MIT-BIH Arrhythmia Database, which contains over 109,000 annotated ECG recordings of 47 subjects at 360 Hz between 1975 and 1979 [184, 185]. Heartbeats are annotated by two or more cardiologists independently. Fourteen original heartbeat types are consolidated into five groups according to the Association for the Advancement of Medical Instrumentation (AAMI) recommendation. This database is widely used in the research community and is considered a benchmark for arrhythmia detection algorithms. The data from the MIT-BIH database was used to pre-train the deep learning models for transfer learning. Specifically, the weights of a pre-trained

model on the MIT-BIH dataset were used to initialize the weights of the model for training on our own dataset.

The second database used in this study was a record of 71 CRT patients from 9 Chinese medical centers. All the patients had an LV ejection fraction (LVEF) $\leq 35\%$, QRS duration > 120 ms, New York Heart Association (NYHA) functional class II to IV symptoms, and optimal medical therapy at least 3 months before CRT. All the patients underwent resting gated SPECT MPI, echocardiography, and NYHA function classification at baseline and 6 months after CRT. This data was used to fine-tune and evaluate the performance of the deep learning models on new, unseen data. This study complied with the Declaration of Helsinki and was approved by local ethics committees. All patients gave written informed consent.

4.2.2 Evaluation of LV function by echocardiography

Echocardiography data of all patients were assessed by experienced ultrasound experts blinded to any clinical data and MPI data before and 6 months after CRT. LVEF was measured by the 2-dimensional modified biplane Simpson method. The present study adopted a reduction of $\geq 15\%$ in LVESV to define volumetric response to CRT, which has been widely accepted as the boundary between responders and non-responders [27, 44, 186].

4.2.3 Preprocessing

Preprocessing of the MIT-BIH dataset and our own dataset is an essential step towards achieving accurate results when training machine learning models for ECG signal analysis. In this study, several preprocessing techniques were applied to the raw ECG data to improve the quality of the data and extract relevant features.

The raw ECG data underwent several preprocessing steps, including a high-pass filter to remove the baseline constant signal, and R-peak detection using a Chebyshev type I fourth-order filter and Shannon energy filter [187, 188]. The ECG data were then segmented into 1.2 RR intervals.

Next, the 1D ECG signals representing HF were transformed into 2D time-frequency spectrograms using a short-time Fourier transform (STFT) with a Hamming window[189, 190]. ECG signals are non-stationary data whose instantaneous frequency varies over time, and the properties of these changes cannot be fully described by using only frequency domain information. The STFT is an improved mathematical method derived from the discrete Fourier transform and used to explore the instantaneous frequency and amplitude of localized waves with time-varying characteristics. When analyzing a non-stationary signal, it is assumed to be approximately stationary within the duration of the temporal window of finite support[191, 192].

The time-frequency spectrogram is given as follows:

$$X(\tau, w) = \int_{-\infty}^{\infty} x(t)w(t-\tau)e^{-jwt}dt \tag{4.1}$$

where $x(t)$ is the ECG signal which is sampled at 360 Hz, and $w(t)$ is the Hanning window function with 512 window size that helps to smooth the signal at the edges of each time segment, reducing spectral leakage and improving the frequency resolution of the transform. The signal preprocessing is performed by the Python library Scipy [193]. A sample of some leads' spectrogram is shown in Figure 4.2.

4.2.4 Resnet and Transfer Learning

This study used three CNN models, ResNet18, ResNet50, and ResNet101, to perform transfer learning on the preprocessed MIT-BIH dataset. The ResNet models are deep neural networks that use residual connections to address the problem of vanishing gradients during training [194].

ResNet is a deep neural network architecture that was introduced by He et al. in 2015 [194]. It is a variant of the traditional CNN that addresses the problem of vanishing gradients in deep networks. The ResNet architecture consists of residual blocks, enabling the network to learn a residual mapping instead of a direct one. The input to a ResNet block is a feature map $\boldsymbol{x}$ with dimensions $H \times W \times C$, where H

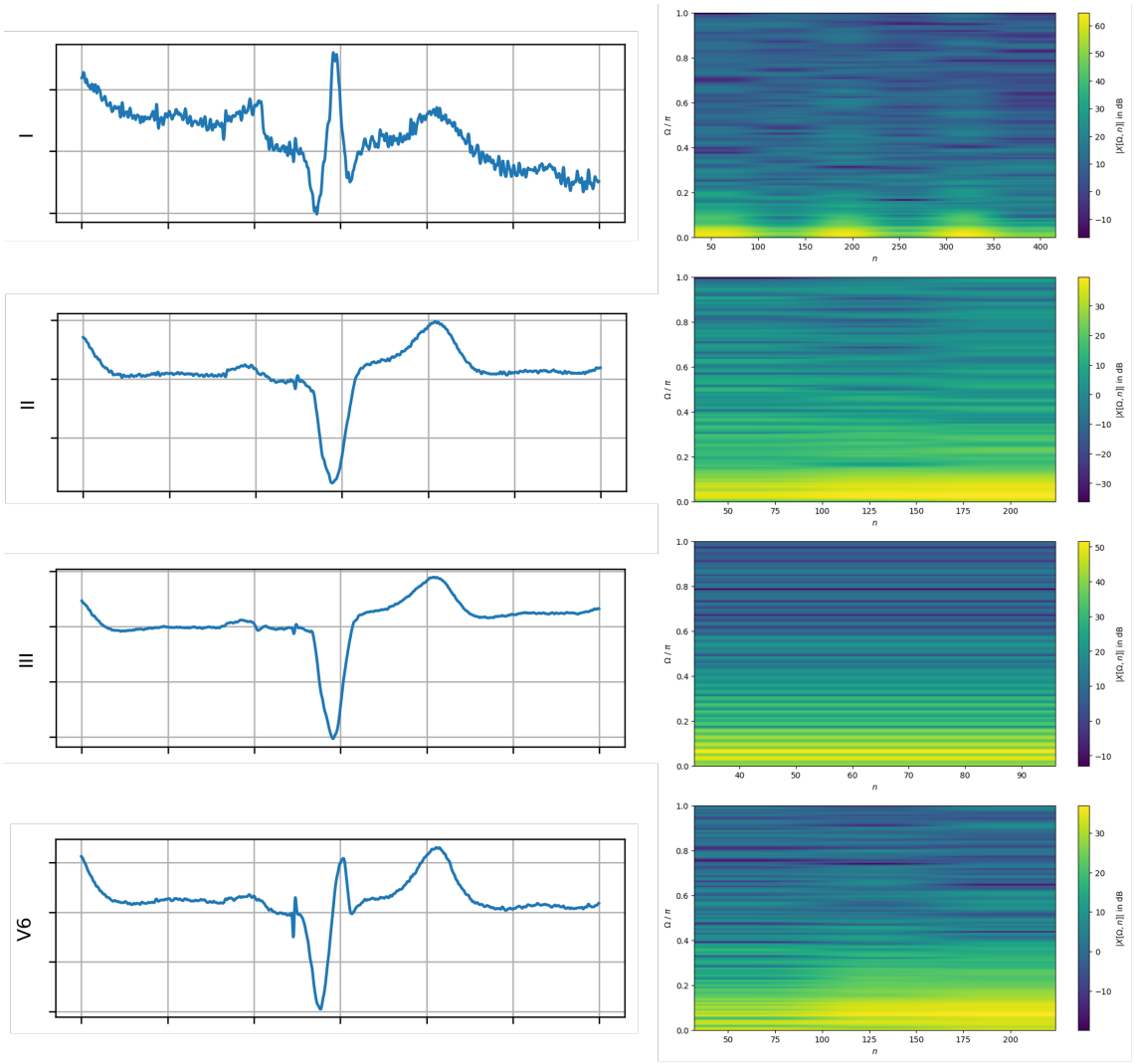

Figure 4.2: ECG spectrogram of sample data

and W are the spatial dimensions and C is the number of channels. The output of the block is also a feature map $\boldsymbol{y}$ with the same dimensions. The residual function $\mathcal{F}$ can be expressed as:

$$\mathcal{F}(\boldsymbol{x};\boldsymbol{\theta}) = \mathcal{H}(\boldsymbol{x};\boldsymbol{\theta}) - \boldsymbol{x}$$

where $\boldsymbol{\theta}$ are the learnable parameters of the residual function, and $\mathcal{H}$ is a set of convolutional layers followed by batch normalization and ReLU activation.

The output of the block is then computed as:

$$\boldsymbol{y} = \sigma(\mathcal{F}(\boldsymbol{x}; \boldsymbol{\theta}) + \boldsymbol{x})$$

where σ is an element-wise activation function (e.g., ReLU or sigmoid). This formulation allows the network to learn residual mappings that are easier to optimize than the original mappings.

Transfer learning is a powerful technique in deep learning that enables us to leverage pre-trained models to solve new tasks with limited data. In transfer learning, we start by pre-training a model on a large dataset, typically using a supervised learning approach. We then use this pre-trained model as a starting point for a new task with a different input and output domain. The pre-trained model is fine-tuned on the new task using a smaller dataset, which typically leads to better performance than training a new model from scratch. In transfer learning, the pre-trained model acts as a feature extractor, and the final layers of the model are modified to adapt it to the new task. We can also freeze some or all of the layers in the pre-trained model to prevent overfitting on the new dataset. This approach allows us to achieve state-of-the-art performance on new tasks with limited labeled data.

4.3 Results

The baseline characteristics of our are shown in Table 4.1. In order to evaluate the performance of a prediction model, it is important to use appropriate evaluation metrics. One commonly used metric is accuracy, which measures the percentage of correct predictions over the total number of predictions made. Sensitivity measures the proportion of true positives (i.e., correctly identified positive cases) among all actual positive cases, while specificity measures the proportion of true negatives (i.e., correctly identified negative cases) among all actual negative cases. Mathematically, these metrics can be defined as follows:

$$\begin{aligned} Accuracy &= \frac{TP + TN}{TP + FP + TN + FN} \\ Sensitivity &= \frac{TP}{TP + FN} \\ Specificity &= \frac{TN}{TN + FP} \end{aligned} \tag{4.2}$$

where TP represents true positives, FN represents false negatives, TN represents true negatives, and FP represents false positives. Sensitivity and specificity can provide insights into how well a model is able to detect positive and negative cases, respectively. A high sensitivity indicates that the model can identify most positive cases, while a high specificity indicates that the model can correctly identify most negative

Table 4.1
Baseline characteristics of the enrolled patients

Variables	All (n=71)	Response (n=46, 64.8%)	Non-response (n=25, 35.2%)	P value
ACEI/ARB	58 (81.7%)	36 (78.3%)	22 (88%)	.318
Age	61.8 ± 12.6	61 ± 13.1	63.2 ± 11.7	.487
Gender	56 (78.9%)	34 (73.9%)	22 (88.0%)	.170
Height(cm)	167.1 ± 7.1	167.0 ± 6.7	167.4 ± 8	.832
Weight(kg)	67.8 ± 14.7	67.0 ± 13.6	69.4 ± 16.8	.505
CKD	5 (7.0%)	2 (4.3%)	3 (12.0%)	.235
DM	15 (21.1%)	6 (13.0%)	9 (36.0%)	.024
Hypertension	33 (46.5%)	22 (47.8%)	11 (44.0%)	.762
Smoking	30 (42.3%)	20 (43.5%)	10 (40.0%)	.781
Beta blocker	64 (90.1%)	40 (87.0%)	24 (96.0%)	.228
Spironolactone	61 (86%)	38 (82.6%)	23 (92.0%)	.284
Digoxin	14 (19.7%)	8 (17.4%)	6 (24.0%)	.511
Diuretic	61 (86.0%)	40 (87.0%)	21 (84.0%)	.737
QRS duration	172.0 ± 23.4	179.4 ± 19.8	158.4 ± 23.7	.000
LBBB	57 (80.2%)	44 (95.7%)	13 (52.0%)	.000
LVEF(%)	26.9 ± 5.1	27.8 ± 5.1	25.2 ± 4.7	.035
LVEDV	286.1 ± 85.2	272.9 ± 86.4	310.4 ± 78.9	.076
LVESV	211.4 ± 74.5	199.1 ± 74.9	234.2 ± 69.6	.057
Scar	26.3 ± 12.1	23.2 ± 11.2	32.0 ± 11.8	.003

Data are expressed as mean ± SD or number (percentage)

cases. However, these metrics can be influenced by the threshold for classifying predictions as positive or negative. It is important to choose an appropriate threshold that balances sensitivity and specificity for the specific application.

The results presented in Table 4.2 were obtained through 5-fold cross-validation in our own ECG database. It can be observed that the prediction performance of various models using only the small ECG database is not satisfactory when compared to clinical guidelines, with the highest accuracy of 0.629, a sensitivity of 0.531, and a

Table 4.2
Performance comparison of deep learning models

	General methods			Pretrained methods (transfer learning)		
Models	**Accuracy**	**Sensitivity**	**Specificity**	**Accuracy**	**Sensitivity**	**Specificity**
Guideline	.6	.93	.038			
SVM	.58 (±.014)	.8 (±.016)	.333 (±.011)			
Random Forest	.58 (±.014)	.91 (±.017)	.125 (±.015)			
ResNet-18	.613 (±.012)	.529 (±.016)	.71 (±.014)	.684 (±.012)	.6 (±.015)	.778 (±.018)
ResNet-50	.612 (±.012)	.53 (±.015)	.73 (±.012)	**.721** (±.015)	**.783** (±.011)	**.792** (±.017)
ResNet-101	.629 (±.012)	.531 (±.016)	.732 (±.013)	.693 (±.015)	.674 (±.011)	.748 (±.013)

specificity of 0.732. However, when transfer learning is utilized to learn from a large-scale public database, significant improvements are observed in the performance of the models with an accuracy of 0.721, a sensitivity of 0.783, and a specificity of 0.792.

4.4 Discussion

Recently, deep learning approaches have been widely used to improve the diagnosis of ECG. Attia et al. [195] proposed a CNN model to identify patients with ventricular dysfunction based on 12-lead ECG (AUC 0.93, accuracy 85.7%). In our work [196], we proposed an end-to-end ECG signal classification method based on a CNN model for the automatic identification of QRS morphology (five classes: normal beat, LBBB, RBBB, ventricular ectopic beat, and paced beat) using the MIT-BIH arrhythmia database [197]. Our CNN model achieved a classification accuracy of 0.9745, a sensitivity of 0.97, and an F1-score of 0.97 in identifying five classes recommended by the Association for Advancement of Medical Instrumentation.

Transfer learning has proven to be a valuable technique to handle the insufficient amount of annotated data that plagues trained classification models of ECG records, particularly for the detection of cardiac arrhythmias and abnormalities. Van [198] innovatively proposed transfer learning from the human ECG dataset to the equine ECG database for classifying four types: normal, premature ventricular contraction, premature atrial contraction, and noise. In the study by Weimann [199], different ResNet models pre-trained on the Icentia11K5 data set with 11,000 patients, were fine-tuned on the PhysioNet/CinC Challenge 2017 data set consisting of 8528 labeled episodes to classify ECG signals into normal sinus rhythm, atrial fibrillation, and noise (too noisy to classify). And the ResNet-34v2 model in the pre-training task for beat classification achieved a performance of .794($\pm$.018) in the final test. Similarly, in the study by Srinivasan et al. (2020), a pre-trained Inception-v3 model was fine-tuned to classify ECG signals into six different arrhythmia classes.

In medical image analysis, the STFT is often used to transform ECG signals into 2D images for input into deep learning models. This allows the model to learn spatial patterns in the signal in addition to temporal patterns [200, 201]. Moreover, it has been shown that without additional manual preprocessing of ECG signals, the accuracy of converting ECG signals into time-frequency spectrograms by short-time Fourier transform as input to 2D-CNN (99.00%) to predict the type of ECG arrhythmias is better than that of 1D-CNN (90.93%) [192].

In this chapter, we present a method for screening CRT patients based on deep learning techniques, demonstrating that pre-training from a large database of ECG arrhythmias and subsequently fine-tuning it on a small local database of CRT patients can significantly improve the performance of the target task, effectively reducing the inability to obtain knowledge of the ECG signal of the arrhythmia due to the small amount of data, and using this prior knowledge to help us to screen CRT patients quickly and efficiently. In the process of the proposed method, the time-domain ECG signal was transformed into a two-dimensional time-frequency ECG spectrum by a short-time Fourier transform. The resulting ECG spectrogram is used as the input to the proposed method. ECG arrhythmias were identified and classified using ResNet. The results show that the average accuracy of the ECG signal based on the 2D convolutional neural network can reach 72.1% for the selection of CRT patients. In addition, we did a series of comparison experiments to achieve the best classification performance with different parameter sets and structures of ResNet models. We found that the classifier based on the proposed 2D-ResNet50 model has the highest accuracy and the lowest loss when the learning rate is 0.001, and the batch size is 2000.

4.5 Conclusion

In this study, we propose an end-to-end ECG classification framework using a 2D CNN classifier. Using the STFT to transform one-dimensional waveforms into two-dimensional frequency-time spectrograms, our framework integrates a generalized pre-trained two-dimensional CNN model for predicting whether a patient corresponds to CRT. The proposed approach outperforms existing clinical guidelines and popular machine learning models.

Chapter 5

Electromechanical dyssynchrony concordance for guiding CRT LV lead position

5.1 Introduction

Cardiac resynchronization therapy (CRT) is an established treatment for heart failure patients with reduced left ventricular (LV) ejection fraction and electrical dyssynchrony [25, 202]. The placement of the LV lead, a crucial component of CRT, is known to affect the response to therapy [4, 90, 203]. The traditional method of LV

lead placement relies on anatomical landmarks and visual inspection, which is one of the reasons that may lead to sub-optimal outcomes in up to 30% of patients [9].

Electroanatomic mapping (EAM) has been proposed as a tool to guide LV lead positioning with detailed and accurate information about the spatial distribution of electrical dyssynchrony [204]. However, EAM is an invasive procedure requiring catheter insertion into the heart, and can be time-consuming, cumbersome, and may carry some morbidity [205]. ECG is a non-invasive and widely available method for assessing electrical dyssynchrony. While it may not provide as detailed information as EAM, ECG is still a valuable tool for identifying patients who may benefit from CRT and guiding the placement of CRT devices. Mechanical dyssynchrony assessed by phase analysis of gated single-photon emission computed tomography (SPECT) myocardial perfusion imaging (MPI) has shown promising results in predicting response to CRT, but its integration with electrical dyssynchrony has not been fully explored [72, 90, 206].

Vectorcardiograms (VCG) record the magnitude and direction of the electrical forces generated by the heart over time; that is, the electricity at each time point is described by a vector. Connecting the arrowheads of all the vectors together constitutes a vector loop. Compared to 1D ECG, 3D VCG provides more intuitive 3D spatial electrical signal information and presents a higher accuracy in determining and localizing ventricular preexcitation in cases where intraventricular electrical conduction

disturbances and regional mobility are relevant [207]. Even though the number of leads has been reduced from 12 in ECG to 3 in VCG, which causes some information loss, it provides the orthonormality of the three leads and the availability of the spatial and temporal relationships of these leads [208].

This chapter presents a novel method for identifying the latest electrical activation position of the heart using a 3D VCG derived from a 1D ECG signal. This approach is then combined with the latest mechanical contraction position of the heart, which is measured using SPECT MPI, to determine the optimal position for placing the LV lead in CRT.

5.2 Methods

5.2.1 Patient population

Seventy-one CRT patients from 9 Chinese medical centers. All the patients had an LV ejection fraction (LVEF) $\leq 35\%$, QRS duration > 120 ms, New York Heart Association (NYHA) functional class II to IV symptoms, and optimal medical therapy at least 3 months before CRT. All the patients underwent resting gated SPECT MPI, echocardiography, and NYHA function classification at baseline and 6 months after CRT. This data was used to fine-tune and evaluate the performance of the deep

learning models on new, unseen data. This study complied with the Declaration of Helsinki and was approved by local ethics committees. All patients gave written informed consent.

5.2.2 Evaluation of LV function by echocardiography

Echocardiography data of all patients were assessed by experienced ultrasound experts blinded to any clinical data and MPI data before and 6 months after CRT. LVEF was measured by the 2-dimensional modified biplane Simpson method. The present study adopted a reduction of $\geq 15\%$ in LVESV to define volumetric response to CRT, which has been widely accepted as the boundary between responders and non-responders [27, 44, 186].

5.2.3 Mechanical dyssynchrony

5.2.3.1 Measurement of mechanical dyssynchrony from SPECT MPI

Technetium-99 m methoxyisobutylisonitrile (99mTc-MIBI) was used to acquire resting ECG-gated SPECT MPI images. The gated SPECT scan was conducted after 60-90 minutes of injection with 25-30 mCi of 99mTc-MIBI at rest. The imaging

process was carried out according to a one-day resting gated SPECT MPI protocol, using a dual-head or triple-head camera system equipped with a low-energy, general-purpose collimator. The pixel size was set to a 64×64 matrix, and the zoom factor was 1.0. The gated images were obtained with a photopeak window of the 99mTc set as a 20% energy window centered over 140 keV. The electrocardiographic R-R interval was divided into 8 frames per cardiac cycle, utilizing a 50% beat acceptance window. For the 180° acquisition, a total of 60 or 64 planar projections of more than 20 seconds/projection were acquired from right anterior oblique 45° to left posterior oblique 45°. SPECT image reconstruction and reorientation were uniformly carried out using the Emory Reconstruction Toolbox (ERToolbox; Atlanta, GA).

An automatic sampling algorithm was utilized to input ungated short-axis images by searching for maximal count circumferential profiles in 3D to represent the regional perfusion level. The polar map displayed the percentage of tracer uptake using a 13-segment model comprising one apical segment, six mid-segments, and six basal segments. The apical segments include all five apical segments in the standard 17-segment model, i.e., the anterior apical segment, the septal apical segment, the inferior apical segment, the lateral apical segment, and the apex. A region with LV sample uptake of less than 50% of maximum was defined as a myocardial scar, while regions with $> 50\%$ scar were identified as scarred segments. A phase analysis technique based on the 1-harmonic Fourier function was employed to approximate the regional uptake count changes over the cardiac cycle and calculate the regional onset of mechanical

contraction represented as a phase angle. The phase distribution polar map was accordingly generated to visualize LV mechanical dyssynchrony.

5.2.3.2 The latest contraction position

The appropriate LV lead position is determined based on the polar maps of myocardial viability and mechanical dyssynchrony. Regions including apical segments, septal segments, and those with more than 50% scar (defined as regions below 50% of the maximum resting perfusion on the viability polar map) are excluded. The recommended area for LV lead placement is the segments where the top 4 phase angles are within 10 degrees of the maximum phase angle, except for the excluded segments [81].

5.2.4 Electrical dyssynchrony

5.2.4.1 Reconstruction of VCG

VCG can be derived from standard 12-lead ECG data based on the multiplication of matrices according to $V = M \cdot E$, where V is a VCG matrix whose lines correspond to

3 VCG leads, M is a transformation matrix, and E is a matrix whose lines are the individual ECG leads. Kors regression transformation [209], inverse Dower transformation [210], Kors quasi-orthogonal transformation and linear regression-based transformation are the most popular transformation methods for deriving VCG from standard 12-lead ECG. Kors regression transformation is a statistical method of mathematical regression based on a large number of patients' data. Inverse Dower transformation is based on the mathematical pseudo-inversion of Dower's method of deriving ECG from VCG. Kors quasi-orthogonal transformation assumes that the X, Y, and Z leads of VCG are similar to the V6, II, and the negative half of V2 leads of ECG, respectively. The linear regression-based transformation uses least squares to obtain the transformation coefficients by minimizing the MSE. Jaros et al. [211] compared these methods and found that Kors regression transformation has the highest accuracy than the other methods.

Differences between the CRT response and non-response group will be compared by the Student t-test for continuous variables and Pearson χ^2 test for categorical variables. The univariate analysis will be applied to estimate potential predictors for CRT response. The multivariable will be performed to analyze the independent predictors and the variables with $P < 0.10$ in the univariate analysis will be included. The predictive value of VCG parameters and their combination will be evaluated by the receiver operator characteristic (ROC) curve analysis. $P < 0.05$ will be considered to be statistically significant. In addition to traditional statistical methods, machine

learning methods such as tree feature selection, support vector machines, and random forests will also be used for feature selection, classification, model, and feature verification.

5.2.4.2 The last activation position by electrical dyssynchrony

Reconstructed 3D VCG data were used to localize the LV latest electrical activating site. As shown in Figure 5.1, the end of the red line represents the maximal T vector, which indicates the end of the ventricular repolarization phase. Accordingly, the location of the latest activating area can be represented as the direction of the maximal T vector. The direction of the maximal T vector suggests the location of the latest activating area at the end of the systolic, which can be used to recommend the optimal LV lead positions for CRT. The rough activating area (anterior, lateral, inferior, and septal) of the latest action potential can be inferred according to the corresponding position relationship between the VCG and the 3D anatomy image of the heart, as illustrated in Figure 5.2.

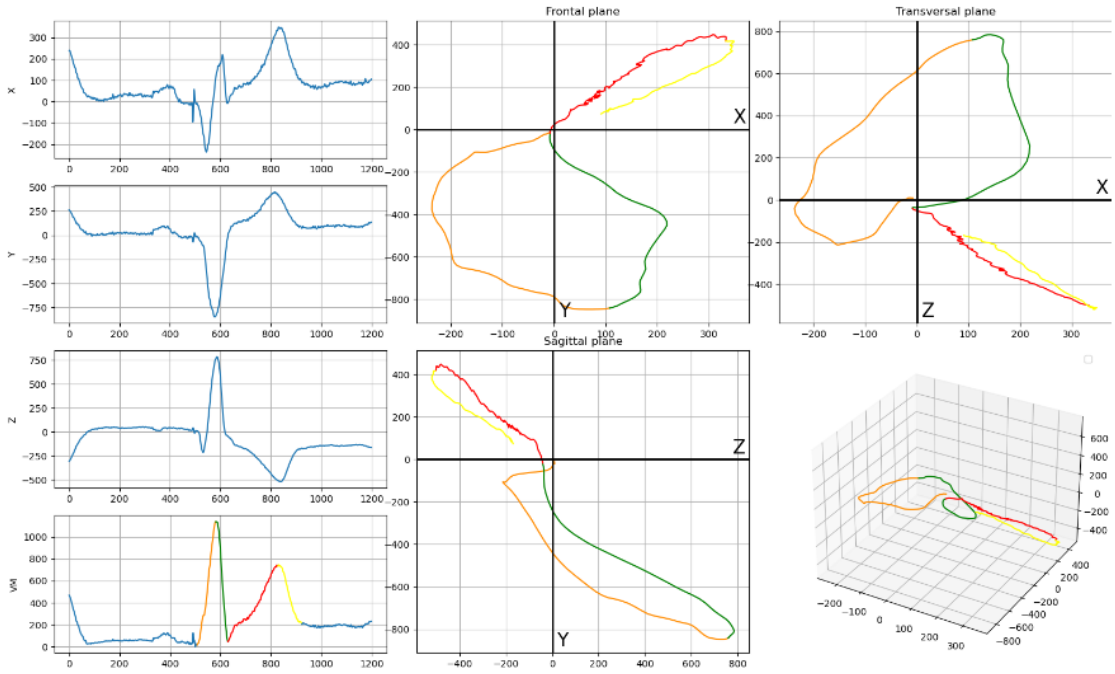

Figure 5.1: Vectorcardiogram (VCG) illustration. Left panels, from top to bottom: scalar representations of the X, Y, and Z leads and of the vector magnitude (VM). Middle and upper right panels: 2D vector loops in the frontal, transverse, and sagittal planes. Lower right panel: 3D vector loop. Calibration: 0.5 mV/division. Colors mark the intervals between characteristic time instants in the ECG. Orange: onset QRS–instant of maximal QRS vector; green: instant of maximal QRS vector–end of QRS; red: end of QRS–instant of maximal T vector; yellow: instant of maximal T vector–end of T; blue: ECG signal outside the QRS-T complex.

5.2.5 Electromechanical dyssynchrony to guide LV lead position for CRT

The latest activating area (4 segments) from VCG and the latest contracting position (17 segments) can be obtained from VCG and gated SPECT MPI, respectively. The hierarchical recommendation strategies in our previous publications [80] and [43] will

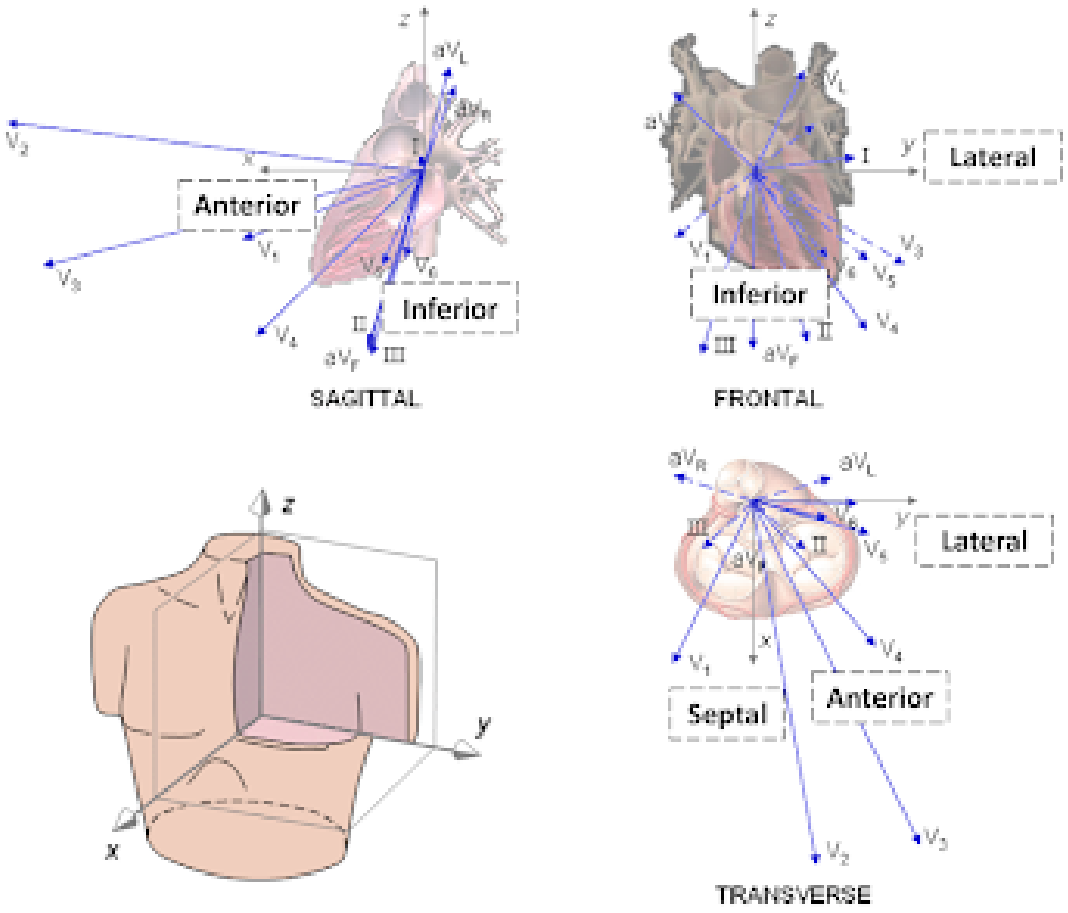

Figure 5.2: The corresponding position relationship between the ECG, VCG, and SPECT MPI polarmap

be used to integrate the latest activating area and latest contacting position. Excluding apical, septal, and scarred segments, there were three levels of recommended segments: (1) the latest contracting viable segments of the SPECT MPI that overlapped with the latest activating area of the VCG; (2) the viable segments adjacent to the latest contracting segments and overlapped with the latest activating area; (3) the latest contracting viable segments in the adjacent area of the latest activating area; (4) the viable segments adjacent to the latest contracting segments and the latest activating area. Figure 5.3 shows the correspondence between the two regions.

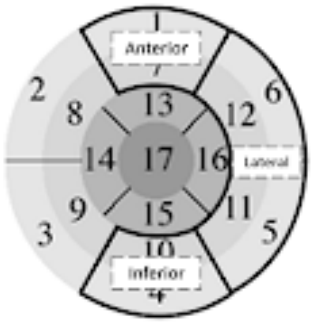

Figure 5.3: The correspondence between the segments of VCG and SPECT MPI polarmap

5.2.6 Identification of LV lead position by CT venography after CRT

Within seven days of CRT implantation, all 71 patients underwent a standard protocol of CT venography. Except for the apex, the LV surface was classified into basal or midsegments in the anteroseptal, anterior, anterolateral, posterolateral, posterior, and posteroseptal walls. CT venography was performed to retrospectively correlate the LV lead position with the recommended segment by SPECT MPI.

5.2.7 Statistic analysis

Differences between the recommended group and non-recommended group were compared by the Student t-test for continuous variables, expressed as mean ± standard

deviation, and Pearson χ^2 test for categorical variables, expressed in number and percentage. The univariate binary logistic regression analysis was applied to estimate potential predictors for CRT response. The multivariable binary logistic regression was performed to analyze the independent predictors of CRT responders and the variables with P $<$ .05 in the univariate analysis were included. Two-sided P-value $<$ .05 was considered to be statistically significant.

5.3 Results

5.3.1 Baseline characteristics

Based on whether the recommended lead position for electromechanical concordance is met or not, patients can be classified into two groups: recommended for CRT and not recommended for CRT, as shown in Table 5.2. Only diabetes and whether the CRT LV lead was on the lateral wall were significantly different between those two groups. Also, as shown in Figure 5.4, the recommended group had a significantly higher CRT response rate than the non-recommended group.

At the 6-month follow-up, the recommended group showed a significant improvement in NYHA (Improvement by $\geq$ 1 class rate is 72% vs. 42.9%), LVESV (P-value: $<$ .0001 vs. .238), LVEDV (P-value: $<$ .001 vs. .269), and LVEF(P-value: $<$ .001 vs.

Table 5.1
Baseline characteristics of the enrolled patients based on electromechanical concordance

Variables	All (n=71)	Recommended (n=50(70.4))	Non-recommended (n=21(29.6))	P value
ACEI/ARB	58 (81.7)	42 (84.0)	16 (76.2)	.660
Age(year)	61.8 ± 12.6	61.1 ± 13.1	63.3 ± 11.6	.504
Male(%)	56 (78.9)	40 (80.0)	16 (76.2)	.968
BMI(kg/m^2)	24.1 ± 4.2	24.2 ± 4.1	24.0 ± 4.6	.850
DM	15 (21.1)	6 (12.0)	9 (42.9.0)	.010
Hypertension	33 (46.5)	20 (40.0)	13 (61.9)	.091
Smoking	30 (42.3)	21 (42.0)	9 (42.9)	.947
NYHA II/III/IV()	25(35.2)/32(45.1)/14(19.7)	20(40.0)/23(46.0)/7(14.0)	5(23.8)/9(42.9)/7(33.3)	.149
Beta blocker(%)	64 (90.1)	46 (92.0)	18 (85.7)	.708
Aldosterone antagonist(%)	61 (85.9)	42 (84.0)	19 (90.5)	.732
Digoxin(%)	14 (19.7)	8 (16.0)	6 (28.6)	.374
Diuretic(%)	61 (85.9)	42 (84.0)	19 (90.5)	.732
QRS duration(ms)	172.0 ± 23.4	174.7 ± 23.6	165.5 ± 22.2	.130
LBBB(%)	57 (80.2)	42 (84.0)	15 (71.4)	.374
LVEF(%)	26.9 ± 5.1	26.6 ± 4.8	27.6 ± 5.7	.462
LVEDV(ml)	286.1 ± 85.2	289.1 ± 86.6	279.0 ± 83.4	.654
LVESV(ml)	211.4 ± 74.5	214.0 ± 74.5	205.3 ± 76.1	.653
Scar burden(%)	26.3 ± 12.1	26.6 ± 12.8	25.5 ± 10.5	.724
LV lead position (Lateral)(%)	57(80.3)	45(90.0)	12(57.1)	.004

Data are expressed as mean ± SD or number (percentage)

.200), which are commonly used indices to assess the effectiveness of CRT, compared to baseline values. Additionally, compared to the non-recommended group, the recommended group demonstrated a significantly better patient therapeutic effect in the improvement of NYHA (P-value: .020), changes/relative changes in LVESV (P-value: .003/.009), LVEDV (P-value: .010/.024), and LVEF (P-value: .007/.005).

5.3.2 Electromechanical dyssynchrony concordance for CRT patient selection

In univariate analysis, DM(OR .27, 95% CI .08-.87), P = .029), QRS< 150ms (OR .03, 95% CI .00-.24, P = .001), LBBB(OR .05, 95% CI .01-.25, $P < .001$), LVEF(OR

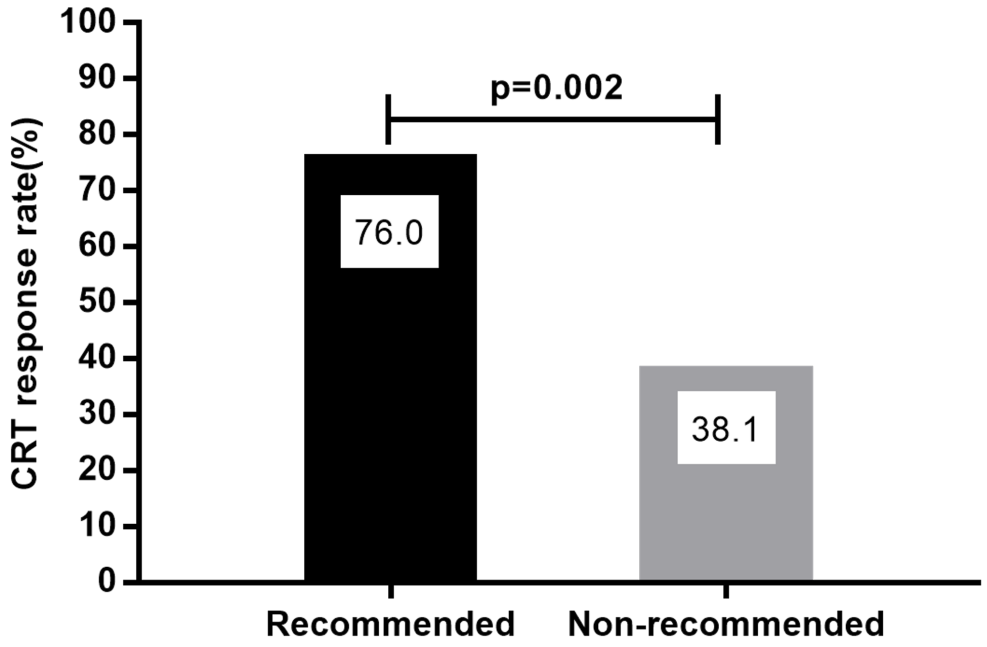

Figure 5.4: Comparison of the results of the recommended and non-recommended groups

1.11, 95% CI 1.01-1.23, P = .04), scar burden(OR .94, 95% CI .89-.98, P = .008), and adherence to recommended lead position based on electromechanical dyssynchrony concordance (OR .19, 95% CI .07-.58, P = .003) were associated with CRT response. In the multivariate analysis, QRS< 150ms(OR .02, 95% CI .00-.29, P = .004), LBBB(OR .06, 95% CI .01-.64, P = .020), scar burden(OR .92, 95% CI .86-.99, P = .025), and adherence to recommended lead position based on electromechanical dyssynchrony concordance (OR .03, 95% CI .00-.31, P = .003) were also independent predictors. The results of the univariate and multivariate analysis are shown in Table 5.3

Table 5.2
Pre- and post-CRT changes in cardiac function

Variables	All (n=71)	Recommended (n=50(70.4))	Non-recommended (n=21(29.6))	P-value
NYHA Class, n(%)				
baseline, II/III/IV	25(35.2)/32(45.1)/14(19.7)	20(40.0)/23(46.0)/7(14.0)	5(23.8)/9(42.9)/7(33.3)	.149
Follow-up, I/II/III/IV	18(25.4)/35(49.3)/8(11.3)/10(14.1)	16(32.0)/26(52.0)/5(10.0)/3(6.0)	2(9.5)/9(42.9)/3(14.3)/7(33.3)	.010
Improvement by ≥ 1 class	45(63.4)	36(72.0)	9(42.9)	.020
LVEDV(ml)				
Baseline	286.1 ± 85.2	289.1 ± 86.6	279.0 ± 83.4	.654
Follow-up	$225.5 \pm 1.1.1$	216.7 ± 99.6	246.4 ± 104.1	.262
Change	60.6 ± 60.3	72.4 ± 62.3	32.6 ± 45.4	.010
Relative change,%	$.225 \pm .200$	$.259 \pm .191$	$.143 \pm .200$	.024
P-value	$< .001$	$< .001$	.269	
LVESV(ml)				
Baseline	211.4 ± 74.5	214.0 ± 74.5	205.3 ± 76.1	.653
Follow-up	150.0 ± 88.4	140.0 ± 85.2	173.8 ± 93.3	.143
Change	61.5 ± 56.2	74.1 ± 56.3	31.5 ± 44.1	.003
Relative change,%	$.317 \pm .259$	$.368 \pm .237$	$.195 \pm .273$	.009
P-value	$< .0001$	$< .0001$	.238	
LVEF(%)				
Baseline	26.9 ± 5.1	26.6 ± 4.8	27.6 ± 5.7	.462
Follow-up	37.5 ± 12.1	39.2 ± 11.9	33.5 ± 11.8	.070
Change	10.6 ± 9.7	12.6 ± 9.6	5.9 ± 8.4	.007
Relative change,%	$.397 \pm .387$	$.480 \pm .398$	$.200 \pm .278$	.005
P-value	$< .0001$	$< .0001$	.200	

Data are expressed as mean ± SD or number (percentage)

Moreover, as shown in Figure 5.5 and Figure 5.6, the electromechanical concordance has improved the CRT response rates for both QRS duration $\geq$ 150ms (76.3% to 860%) and LBBB (77.2% to 85.7%) according to the recommendations on clinical guidelines. In particular, in the case of non-optimal clinical guideline recommendations, the improvement in CRT response rates based on electromechanical concordance recommendations for LV lead placement was substantial (QRS duration $<$ 150ms: 8,3% to 50%, non-LBBB: 14.3% to 53.3%).

Table 5.3
Univariate and multivariate logistic regression analyses

	Univariate analysis		Multivariate analysis	
Variables	**OR(95% CI)**	**P-value**	**OR(95% CI)**	**P-value**
Age	.99(.95-1.03)	.481		
Male	.37(.10-1.53)	.175		
BMI	.96(.86-1.08)	.516		
Hypertension	1.17(.44-3.11)	.758		
DM	.27(.08-.87)	.029	1.59(.14-17.67)	.706
Smoking	1.15(.43-3.11)	.777		
QRS<150	.03(.00-.24)	.001	.02(.00-.29)	**.004**
LBBB	.05(.01-.25)	$<.001$	.06(.01-.64)	**.020**
ACEI/ARB	.50(.12-1.98)	.317		
Beta-blocker	.28(.03-2.45)	.249		
Aldosterone antagonist	0.41(0.08-2.12)	.289		
Digoxin	.67(.20-2.20)	.505		
LVEF	1.11(1.01-1.23)	.04	1.18(.98-1.42)	.075
EDV	1.00(1.00-1.00)	.085		
ESV	.99(.99-1.00)	.067		
PSD	.99(.97-1.02)	.550		
PBW	1.00(.99-1.01)	.966		
Scar burden	.94(.89-.98)	.008	.92(.86-.99)	**.025**
Recommended position	.19(.07-.58)	.003	.03(.00-.31)	**.003**

Underlining indicates that the significant level in the univariate analysis is less than 0.05.
Bold indicates that the significant level in the multivariate analysis is less than 0.05.

5.4 Discussion

The mode of action of CRT is to correct mechanical dyssynchrony by electrical activation to restore the heart's mechanical function and improve cardiac contractility, which seems like an inefficient and circuitous approach [204].

EAM has been used to detect the latest activated region to guide LV and RV lead

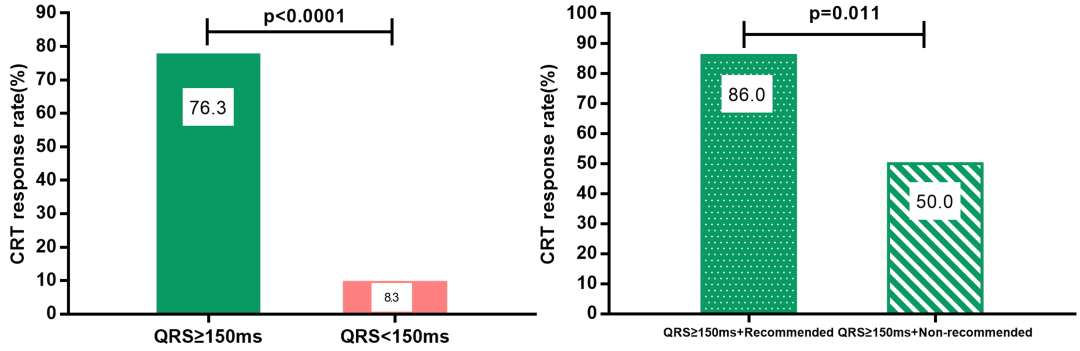

Figure 5.5: The improvement brought by electromechanical dyssynchrnony concordance on the CRT patient selection with QRS duration

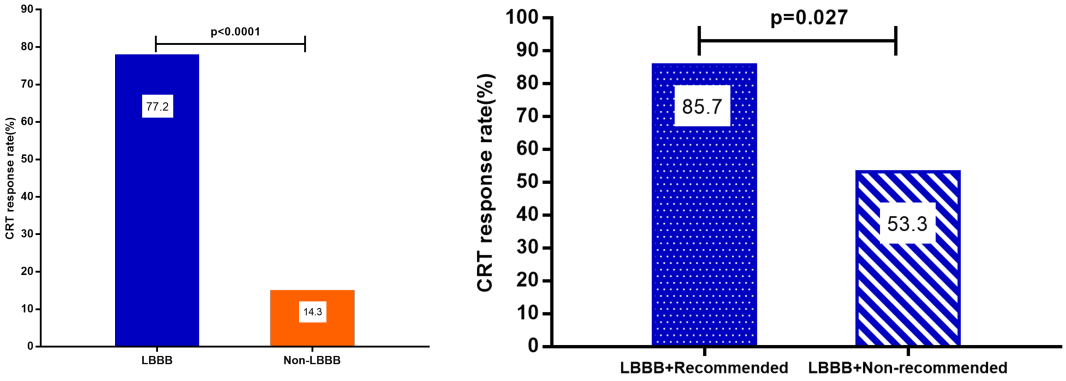

Figure 5.6: The improvement brought by electromechanical dyssynchrnony concordance on the CRT patient selection with LBBB

position during CRT implementation[212, 213]. However, it is an invasive procedure requiring catheter insertion into the heart and can be time-consuming, cumbersome, and may carry some morbidity [205]. Electrocardiographic imaging (ECGi) is a novel and non-invasive modality to measure electrical dyssynchrony [204], but more clinical trial data, training of operators, and widespread availability of equipment are needed.

Using VCG to measure the latest activation site of the heart is an innovative approach to guiding the placement of CRT leads. VCG provides a more comprehensive and accurate assessment of cardiac electrical activity by capturing the direction and magnitude of the cardiac electrical vectors [207]. In [214], The accuracy of ECG and VCG in identifying the site of pre-excitation was compared in 41 patients with Wolff-Parkinson-White syndrome. VCG was found to be a good predictor of the localization of 3 accessory pathways (AP) identified by endo-cavitary electrophysiologic (right free ventricular wall, posterior, or left free ventricular wall) than ECG (Sensitivity 96.5% vs. 77.1%, specificity 90.7% vs. 91.5%, positive predictive values 80% vs. 75%). Moreover, VCG can identify the AP location (anterior right, lateral right, posterior right, posterior left, lateral left, or anterior left ventricle) with better sensitivity (43.6% vs. 39.3%), specificity (92.1% vs. 87.4%), and positive predictive values (51.5% vs. 33.3%) than ECG. Moreover, Rad et al. [215] found that the QRS area measured by VCG can identify delayed left ventricular lateral walls.

Transthoracic echocardiography[44, 216], cardiac MRI [217, 218, 219], cardiac CT [38, 220], and SPECT MPI [4, 14, 42, 73] have all demonstrated effectiveness in assessing mechanical dyssynchrony, identifying the latest contraction position, and placing the lead in the latest contraction position improved CRT response rate and patient survival rate. It should be noted that in none of the randomized trials, the position of the LV lead was studied in various positions and adjusted or optimized intra-individually according to intraprocedural echo parameters [221]. On

the other hand, a study conducted by Badran et al. [222] demonstrated that 3D echocardiography-guided LV lead placement did not provide any clinical advantage compared to conventional techniques. At present, no mechanical dyssynchrony parameter is widely accepted or endorsed by guidelines for identifying CRT responders [50]. This is also evident in the 2016 ESC guidelines for diagnosing and treating acute and chronic heart failure, which do not recommend using echocardiographic dyssynchrony as selection criteria for CRT [24].

Since the ECG indicators in clinical guidelines cannot provide sufficient detailed information to correct mechanical dyssynchrony of the heart, and mechanical dyssynchrony has many unstable outcomes, combining electrical and mechanical dyssynchrony, i.e., electromechanical dyssynchrony, is a rational and reasonable approach. Albatat et al. [223] proposed an electromechanical model that combines cardiac MRI with fiber orientation to obtain a 3D finite element mesh that extracts electrical and mechanical components from the ionic and myofilament model, respectively. However, to save computational time, it is difficult to simulate endocardial scar burden by coarse geometric meshes for cardiac imaging. Bunting et al. [224] proposed a novel electromechanical wave imaging to characterize the electromechanical activation based on ultrasound technology by measuring the transient initiation of myocardial strain. However, the sample size (n=16) is too small, and more data are needed to support this technique.

5.5 Limitation

This was a multicenter, nonrandomized, retrospective study. The small number of patients is the largest limitation of this study. However, this study aimed to demonstrate the feasibility of VCG as a novel technique to characterize electrical dyssynchrony in HF patients and guide optimal LV lead with mechanical dyssynchrony. Moreover, the method of using VCG to locate the direction of the latest activation position in this paper is a crude calculation, but it does help us to further optimize the selection of the LV lead position by choosing based on mechanical dyssynchrony. EAM technique will yield more accurate recommended positions, but the method is invasive, and ECGi may be a better choice for the recommended latest electrical signal position. More experiments are needed in the future.

5.6 Conclusion

The present study introduces a novel approach for determining the latest activation position of the heart using VCG and combining it with the latest contraction position measured by SPECT MPI. This innovative method aims to suggest an optimized position for the placement of the CRT LV lead through electromechanical dyssynchrony concordance.

Chapter 6

Reinforcement learning to improve multi-stage clinical decisions for CRT delivery

6.1 Introduction

The approach of selecting CRT patients based on both mechanical and electrical dyssynchrony lacks clear understanding. The process of clinical decision-making for CRT patient selection involves utilizing available clinical records and examination results to assess the next course of action. This presents a complex sequential problem

that lacks a coherent decision-making strategy for reaching a definitive result step-by-step. Most existing artificial intelligence methods for patient selection are based on a form of machine learning called supervised learning, which entails obtaining all clinical test data and ground truth labels at once and predicting the final definitive outcomes. For physicians, this result is either a "black box" or has a ranking of feature importance that can be used for reference, but there is a lack of a coherent decision-making strategy for how to get to that result step-by-step.

Reinforcement learning (RL) is a subtype of machine learning that encourages an agent to make an optimal decision using a policy when interacting with an unknown environment by maximizing the acquired rewards. The policy is a mapping from obtained inputs to actions that can control the agent's behavior. The agent also never knows the correct answer, i.e., the ground truth, but instead receives an evaluation signal to indicate how well the action is currently performing.

This chapter explores new approaches to the multi-stage classification tasks for CRT patient selection using reinforcement learning. Moreover, we also propose novel reward functions based on clinical experience to evaluate the benefits of CRT to patients.

6.2 Background

Medical diagnosis is a process of mapping information from a patient, such as family history, personal treatment history, current signs, and symptoms, to an accurate diagnosis of a disease. As a complex task requiring thorough medical investigation of the clinical situation, assimilating valid information from multiple complex data sources, and making decisions, it imposes a significant cognitive burden on clinicians. Diagnostic errors are reported to account for 10 percent of hospital deaths and 17 percent of adverse events [225]. The error-prone process in diagnosis and the necessity to assist clinicians in a better and more efficient decision-making urgently call for a significant revolution of the diagnostic process, driven by advanced big data analytics and machine learning technologies that have brought about the era of automated diagnosis [226, 227, 228].

Existing machine learning approaches to clinical diagnosis rely heavily on many annotated samples and are usually formulated as supervised classification problems to infer and predict possible diagnostic outcomes [229, 230, 231]. In addition, these end-to-end approaches have limitations in tapping into the dynamic multi-step decision-making and facing uncertainty in the actual diagnostic process, and only consider a limited number of predictive labels in the immediate future [232].

RL effectively avoids these problems and performs well in various traditional analysis tasks in medical image examination, such as feature extraction, image segmentation, and object detection/localization/tracking [233]. A series of studies by Sahba et al. [234, 235, 236, 237], which deeply improved the RL model and applied it to extract the boundaries of target objects in sequential images. Liu and Jiang [238] used the DRL method, Trusted Region Policy Optimization (TRPO), to optimize joint surgical gesture segmentation and classification by integrating temporal consistency into the action design and reward mechanism of the RL model to reduce over-segmentation errors.

Netto et al. [239] provided an overview of work on RL in medical image applications, detailing specific applications of RL to lung nodule classification. The traditional classification problem is modeled as a sequential decision problem applicable to RL. Where each state is defined as a combination of multiple multi-dimensional feature values, the action is a random transition between states. The ultimate goal is to discover the shortest path from an existing pattern to a known malignant or benign pattern target. Preliminary results show that the Q-learning approach can effectively classify benign and malignant lung nodules directly from CT images of lung lesions [240].

6.3 Reinforcement Learning

RL encourage an agent to learn an effective policy in sequential decision-making task by trial-and-error interactions with its environment[241]. The most general framework to formalize an RL problem is *Markov decision process* (MDP).

6.3.1 Markov decision process

The RL model is a descriptor of the environment that learns and infers how that environment interacts with and provides feedback to the agent. Formally, an MDP can be defined by a 4-tuple $M = (S, A, P, R)$, where S is *state* space, and $s_t \in S$ denotes the state of an agent at time t; A is a set of *actions* for the agent, and $a_t \in A$ denotes the action of an agent performs at time t; $P(s', r|s, a)$ is the Markovian *transition function*, which determines which state is the next (s') under the current state s and action a; *reward function* R is the feedback provided to the agent by the environment in state s, after the agent takes action a.

The transition probability function denotes the probability of transitioning from state s to the next state s' after taking action a and then getting a reward r.

$$P(s', r|s, a) = \mathbb{P}[S_{t+1} = s', R_{t+1} = r|S_t = s, A_t = a]$$

$\mathbb{P}$ is used as a symbol of probability. So, the state-transition function can be defined as a function of $P(s', r|s, a)$:

$$P(s'|s, a) = \mathbb{P}[S_{t+1} = s'|S_t = s, A_t = a] = \sum_{r \in R} P(s', r|s, a)$$

And the reward function R predicts the next reward based on one action a:

$$R(s, a) = \mathbb{E}[R_{t+1}|S_t = s, A_t = a] = \sum_{r \in R} r \sum_{s' \in S} P(s', r|s, a)$$

Policy (π: $S \times A \to [0, 1]$), as the agent's behavior function is a probability distribution that maps an action $a \in A$ to a state $s \in S$. When given an MDP system and a policy π, the expected accumulated reward when starting the state s, the value function $V_\pi(s)$, can be defined as:

$$G_t = R_{t+1} + \gamma R_{t+2} + \gamma^2 R_{t+3} + \cdots = \sum_{k=0}^{\infty} \gamma^k R_{t+k+1} \tag{6.1}$$

where the $\gamma \in [0, 1]$ denotes the discounting factor penalizing the rewards in the future. The *state-value* of a state s is the expected feedback in this state at time t:

$$V_\pi(s) = \mathbb{E}_\pi[G_t|S_t = s]$$

Similarly, the *action-value* (Q-value) of a state-action pair is defined as:

$$Q_\pi(s,a) = \mathbb{E}_\pi[G_t|S_t = s, A_t = a]$$

Moreover, since the RL system follows the target policy π, the probability distribution over possible actions and the Q-values to recover the state-value is:

$$V_\pi(s) = \sum_{a \in A} Q_\pi(s,a)\pi(a|s)$$

6.3.1.1 Bellman Equations

The value function can also be defined recursively using the *Bellman operator* in MDP system:

$$\begin{aligned} V(s) &= \mathbb{E}[G_t|S_t = s] \\ &= \mathbb{E}[R_{t+1} + \gamma R_{t+2} + \gamma^2 R_{t+3} + \cdots |S_t = s] \\ &= \mathbb{E}[R_{t+1} + \gamma(R_{t+2} + \gamma R_{t+3} + \cdots)|S_t = s] \\ &= \mathbb{E}[R_{t+1} + \gamma V(S_{t+1})|S_t = s] \\ &= R(s,\pi(s)) + \gamma \sum_{s' \in S} P(s,a,s')V_\pi(s') \end{aligned} \tag{6.2}$$

Similarly for the Q-value to represent the optimal value of each state-action pair:

$$\begin{aligned} Q(s,a) &= E[R_{t+1} + \gamma V(S_{t+1}) | S_t = s, A_t = a] \\ &= E[R_{t+1} + \gamma \mathbb{E}_{a\ \pi} Q(s_{t+1}, a) | S_t = s, A_t = a] \end{aligned} \tag{6.3}$$

Bellman Expectation Equations

The recursive update process can be further decomposed into equations built on the state-value and action-value functions. Extend V alternatively by following the policy π, the Bellman expectation equations can be defined as:

$$\begin{aligned} V_\pi &= \sum_{a \in A} \pi(a|s) Q_\pi(s,a) \\ Q_{pi}(s,a) &= R(s,a) + \gamma \sum_{s' \in S} P(s'|s,a), V_\pi(s') \\ V_\pi(s) &= \sum_{a \in A} \pi(a|s)(R(s,a) + \gamma \sum_{s' \in S} P(s'|s,a), V_\pi(s')) \\ Q_\pi(s,a) &= R(s,a) + \gamma \sum_{s' \in S} P(s'|s,a), \sum_{a' \in A} \pi(a'|s') Q_\pi(s',a') \end{aligned} \tag{6.4}$$

Bellman Optimality Equations

The goal of the MDP problem is to achieve an *optimal policy* π_* that $V_{\pi_*}(s) \geq V_\pi(s)$ for every policy π and every state $s \in S$. So, the optimal value of each state-action

Algorithm 1 Q-learning

Initialize $t = 0$, Q-function $Q(s, a)$, $\forall s \in S, a \in A$
repeat (for each episode):
    Given state s_t, take action a_t based on Q (e.g., ϵ-greedy)
    $Q(s, a) \leftarrow Q(s, a) + \alpha[R + \gamma \max_a Q(s', a) - Q(s, a)]$
    $s \leftarrow s'$
until s is terminal

pair is:

$$\begin{aligned} V_*(s) &= \max_{a \in A} Q_*(s, a) \\ Q_*(s, a) &= R(s, a) + \gamma \sum_{s' \in S} P(s'|s, a), V_*(s') \\ V_*(s) &= \max_{a \in A} (R(s, a) + \gamma \sum_{s' \in S} P(s'|s, a), V_*(s')) \\ Q_*(s, a) &= R(s, a) + \gamma \sum_{s' \in S} P(s'|s, a), \max_{a' \in A} Q_\pi(s', a') \end{aligned} \tag{6.5}$$

6.3.2 Deep Q-Network

Q-learning[242] is a big breakout in the early days of RL. In each episode, it works as shown in Algorithm 1:

The deep Q-Network [106] aims to greatly improve and stabilize the training procedure of Q-learning through two innovative mechanisms:

1. **Replay buffer**. All episode steps $e_t = (s_t, a_t, r_t, s_{t+1})$ are stored in a replay memory $D_t = e_1, e_2, \cdots, e_t$. The experience in the buffer D_t comes from different policies. During the Q-learning updates, samples are selected from the

buffer randomly, and thus one sample could be used multiple times. This replay buffer method reduces the number of interactions, improves data efficiency, and smooths over changes in the data distribution[106].

2. **Target network**. Instead of updating output Q every step, deep Q-learning introduces a target Q-network $\hat{Q}$, which is cloned and kept frozen, and only periodically updated every C step. This modification makes the training more stable because it overcomes short-term oscillations.

6.3.3 Policy Gradient

The goal of the policy gradient approach is to directly model and optimize the policy. The policy is typically modeled with a parameterized function respect to $\theta, \pi_\theta(a|s)$. The value of the reward function depends on this policy, and various algorithms can then be applied to optimize *theta* for the best reward.

$$J(\theta) = \sum_{s \in S} d_\pi(s) V_\pi(s) = \sum_{s \in S} d_\pi(s) \sum_{a \in A} \pi_\theta(a|s) Q_\pi(s, a)$$

where $d_\pi(s)$ is the stationary distribution of Markov chain of π_θ (on-policy state distribution under π). For simplicity, the parameter θ is omitted when the policy π_θ appears in the subscript of other functions; for example, d_π and Q_π should be d_{π_θ} and Q_{π_θ} if written in full.

Algorithm 2 Actor-Critic

Initialize s, θ, w at random; sample a $\pi_\theta(a|s)$
for $t = 1 \cdots T$: **do**
    Sample reward r_t $R(s, a)$ and next state s' $P(s'|s, a)$
    Sample the next action a' $\pi_\theta(a'|s')$
    $\theta \leftarrow \theta + \alpha_\theta Q_w(s, a) \nabla_\theta \ln \pi_{\theta(a|s)}$
    $\delta_t = r_t + \gamma Q_w(s', a') - Q_w(s, a)$
    $w \leftarrow w + \alpha_w \delta_t \nabla_w Q_w(s, a)$
    $a \leftarrow a'$, $s \leftarrow s'$
end for

6.3.3.1 Actor-Critic

In addition to learning policy, learning the value function is also of great importance because learning the value function can help with policy updates, such as reducing gradient differences in the vanilla policy gradient, which is where the actor-critic approach comes into play.

Actor-Critic is a *temporal difference* version of policy gradient algorithm which consist of two models: **Actor** decides which action should be taken and updates the policy parameters θ for $\pi_\theta(a|s)$, under the suggestion from the critic; **Critic** evaluates the action given by the actor and updates the value function parameters w. The pseudocode of the Actor-Critic is shown in Algorithm 2.

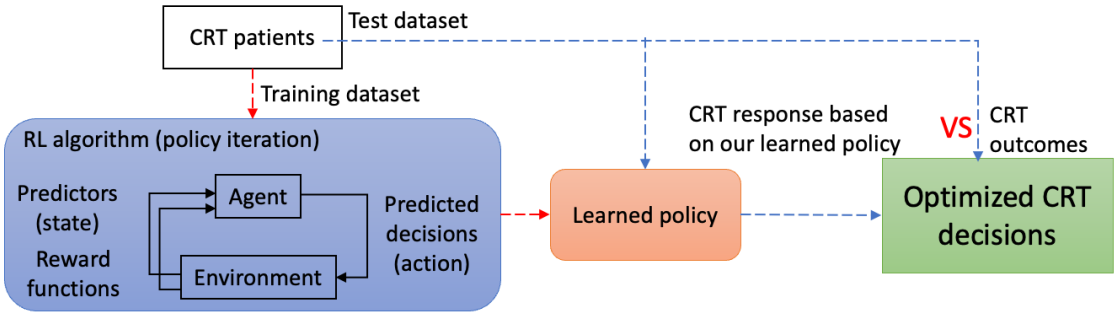

Figure 6.1: Reinforcement learning to optimize CRT decisions

6.4 Problem Formulation

We defined an action space (composed of three decisions yes/no in the first three stages and eight candidate LV pacing sites in the fourth stage) for the medical interventions covering a state space (clinical factors in Figure 1). We will model the action space into sequential decisions. The final output is four variables in the action space.

6.5 Novel reward functions for CRT patient selection

In a general RL setting, the reward function is represented in the form of an evaluative scalar signal, which encodes a single objective for the learning agent. Researchers have combined multiple metrics and tried different weights to find the best reward function

based on the existing clinical guidelines, or the outcome of interest[108]. In this study, an initial reward function based on the volumetric CRT response, illustrated as follows, will be built:

$$\begin{aligned} f_{Reward} = C_1 \times sigmoid(&Outcome\, of\ Primary\ Endpoint) \\ &+ C_2 \times Outcome\, of\ Secondary\ Endpoint \\ &+ C_3 \end{aligned} \tag{6.6}$$

where C_1, C_2(negative if the secondary endpoint occurred; otherwise, positive), C_3 are hyperparameters. Expert knowledge based on the current standard guideline (see [25]) and our experience with the weights of different CRT-related parameters will be used to fine-tune these hyperparameters for the optimal reward function. Similarly, the sigmoid equation here can be replaced by the activation function equations such as tanh, relu, etc. activation function.

6.6 Experiments

6.6.1 Study design and participants

One hundred and fifty-seven CRT patients from nine medical centers in China and one hundred and ninety-nine CRT patients of the multicenter VISION-CRT trial[87]

were enrolled in this experiment. Eligible patients had had at least two encounters with SPECT MPI and had at least one encounter with ECG (QRS duration *geq* 120 ms). Eighty percent of the eligible patients were randomly selected as the training set for training the RL algorithm, and the remaining 20% were used as the test set to evaluate the performance of the RL algorithm. In addition, due to the limited sample of the dataset, we will repeat the cross-validation with 10 folds to ensure the stability of the model.

For each patient, we had access to clinical records, including age, gender, race, and smoking status, as well as ECG data, including QRS duration and LBBB, and SPECT MPI data, including systolic and diastolic lVEF, ESV, EDV, PSD, PBW, phase kurt, phase peak, phase skewness, respectively.

6.6.2 Overview of the reinforcement learning model

RL algorithms model the course of patients' electronic health record (EHR) histories using an MDP with key elements, including state, action, and reward[241, 243]. In this setting, "state" refers to the observed patient characteristics, including age, gender, race, medical records, ECG test results, echo test results, and SPECT test results. "Action" refers to whether CRT is recommended for this patient. The result of an action is a numerical reward that represents an improvement in health

outcomes compared to the previous encounter. In this work, we use the variation of SPECT LVEF as the primary endpoint. Substituting Eq. 6.6, and trying different normalization methods, we obtain the following formulas.

$$rewards = (LVEF_{post} - LVEF_{pre} - c_1) \times c_2 \tag{6.7}$$

$$rewards = sigmoid(LVEF_{post} - LVEF_{pre} - c_1) \tag{6.8}$$

$$rewards = \tan(LVEF_{post} - LVEF_{pre} - c_1) \tag{6.9}$$

where c_1, c_2 are hyperparameters.

6.6.3 Model evaluation

The evaluation of off-policy models is challenging because it is difficult to estimate whether the rollout of a learned policy (used to determine actions at each state) would eventually lead to improved CRT response. Furthermore, directly comparing Q-values on off-policy data, as done in prior applications of RL to healthcare, can provide incorrect performance estimates [243]. In this work, we propose to use the method of Doubly Robust Off-policy Value Evaluation [244] to evaluate policies. We also compute the mean Q-values of chosen actions in real CRT decisions. Using both these estimates, and the predicted vs. real CRT outcomes, we can assess the

potential improvement that our learned policy could bring in terms of an increase in CRT response rate. We will compare these decisions proposed by the learned (optimal) policy with those made by CRT experts to understand what are differences and whether/how these new decisions by the learned policy bring new knowledge to and benefit the CRT clinical practice. Figure 5 illustrates the training, test, and validation process of the proposed RL model. We evaluated the effectiveness of RL-recommended treatments by comparing their actual outcomes with those of CRT. And also compared the effectiveness of patient selection according to clinical guidelines as well as traditional ML classification algorithms.

6.6.4 Feature importance

When analyzing tabular data, local interpretable model-agnostic explanations (LIME)[245], Shapley Additive exPlanations (SHAP)[246], and partial dependence plots (PDP)[247] are all suitable methods for feature interpretation. LIME is often considered the preferred choice for tabular features due to its ability to provide local explanations, which allows for the explanation of predictions of individual instances in the dataset. This is especially advantageous in certain applications, such as CRT decision-making, where interpreting a single instance is important. While SHAP and PDP are also useful for interpreting tabular features, they offer more global explanations compared to LIME. These methods are particularly useful for identifying the

most significant features across the entire dataset and understanding how they interact with each other to influence the model's predictions. However, for this CRT study, we wanted patient-specific decision strategies rather than a generalized analysis of the overall data.

LIME creates locally interpretable explanations for a single data point. LIME creates a linear surrogate model that approximates the local behavior of the predictor for a single prediction. By creating a perturbed dataset made up of local perturbations around the decision in question, the importance of each feature in the black box predictor can be inferred. The output from LIME is a vector of coefficients that suggests how increasing or decreasing variables affect the prediction. As described in Ribeiro et al. [245].

Figure 6.2 shows the attributions of the feature of LIME for the two CRT non-responders. We can see that for the same variable LVEDV, patient A gets a positive contribution to the CRT non-responder due to LVEDV $\leq$ 165.75; patient B gets a contribution to the CRT non-responder due to LVEDV $>$ 322.5; but combining other factors, including ESV, Myocardial mass, PSD, PBW, etc., the model judges both patients as non-responders. Note that the x-axis in the figure represents the degree to which each state contributes to the output of the respective action in the positive or negative direction.

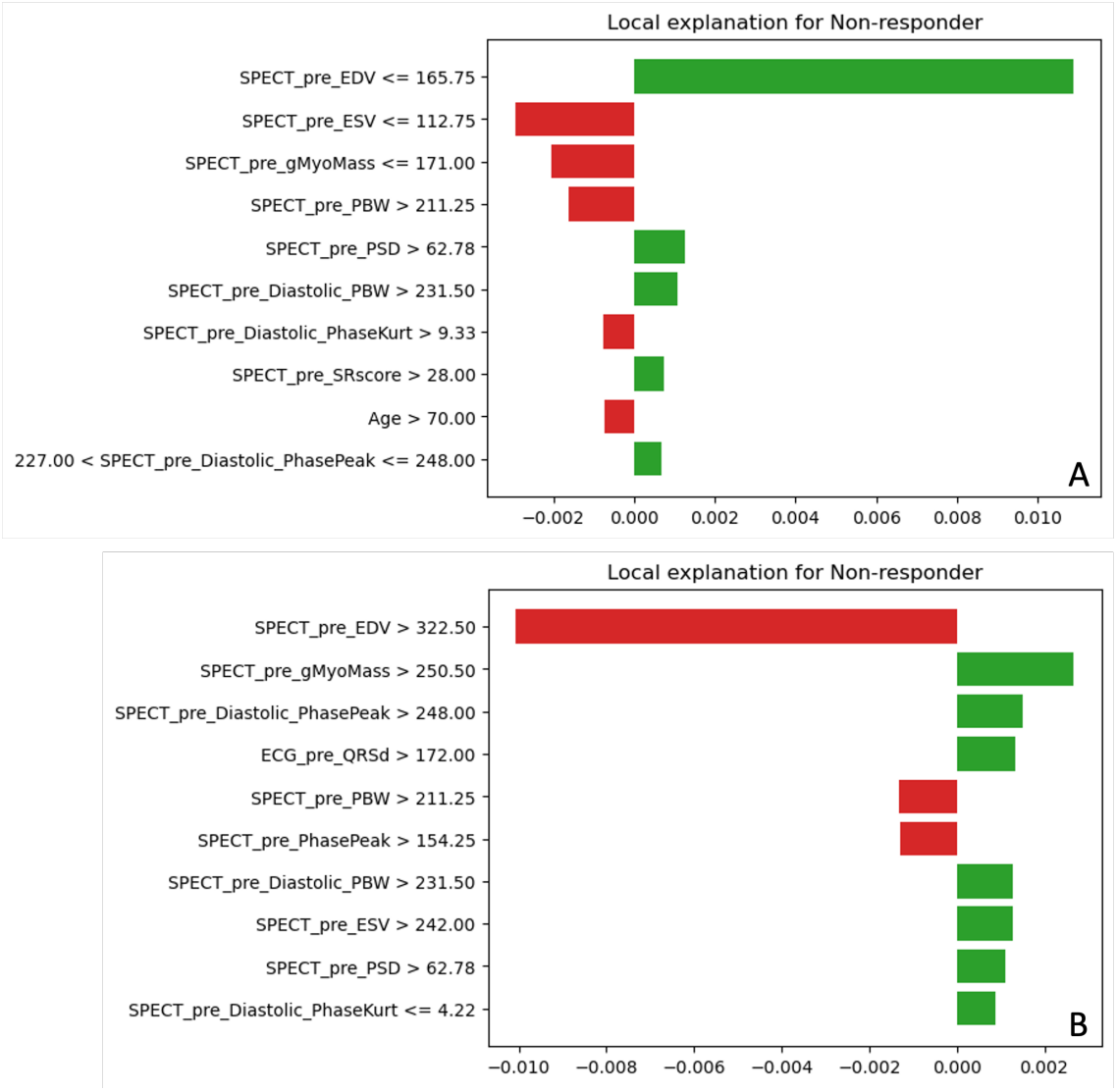

Figure 6.2: Feature attributions for two CRT non-responders by LIME

6.6.5 Results

Complete clinical assessment data, baseline SPECT MPI, and 6-month follow-up SPECT MPI data were obtained in 230 patients. The demographic and clinic characteristics of the analysis dataset are shown in Table 6.1. Overall, patients were 62.2

years of age and comprised 140 males (60.9%). The performance of the RL algorithms on the repeated 20 times of the 10-folds cross-validation is summarized in Table 6.2

6.7 Conclusion

In this study, we utilize deep reinforcement learning to tackle the challenge of determining optimal treatment decisions for patients undergoing CRT. We explore models with a discrete state space and specific action space to identify the most effective treatment policy, improve the reward equation based on the insights of experienced physicians, and leverage Deep Q-learning and PPO networks to approximate the best action value function. These efforts aim to improve the treatment policy utilized by clinicians and provide interpretability. Future research should examine the learned policies for each patient and explore alternative modeling approaches, such as model-based reinforcement learning.

Table 6.1
Baseline characteristics and left-ventricular parameters of the enrolled patients.

Variables	All (n=230)	CRT Responder (n=130, 56.5%)	Non-responder (n=100, 43.5%)	P-value (T-test/χ^2)
Age	62.2 ± 11.9	63.2 ± 11.7	60.9 ± 12.0	0.048
ACEI or ARB	187 (81.3%)	112 (86.2%)	75 (75.0%)	0.048
AE #12	2.9 ± 0.9	2.9 ± 0.9	2.9 ± 0.8	NaN
AE #28	7.3 ± 2.2	7.3 ± 2.3	7.4 ± 2.0	NaN
AE #31	3.3 ± 1.0	3.3 ± 1.1	3.4 ± 0.9	NaN
AE #8	5.8 ± 1.8	5.8 ± 1.9	5.9 ± 1.7	NaN
Age	62.2 ± 11.9	63.2 ± 11.7	60.9 ± 12.0	0.148
CAD	74 (32.2%)	31 (23.8%)	43 (43.0%)	0.003
DM	58 (25.2%)	28 (21.5%)	30 (30.0%)	0.190
QRS duration	159.2 ± 25.0	160.3 ± 23.0	157.8 ± 27.4	0.445
Gender	140 (60.9%)	76 (58.5%)	64 (64.0%)	0.473
LBBB	226 (98.3%)	127 (97.7%)	99 (99.0%)	0.808
NYHA				0.102
II	61 (26.5%)	40 (30.8%)	21 (21.0%)	
III	136 (59.1%)	69 (53.1%)	67 (67.0%)	
IV	33 (14.3%)	21 (16.2%)	12 (12.0%)	
Race				0.001
African	15 (6.5%)	6 (4.6%)	9 (9.0%)	
Asian	86 (37.4%)	63 (48.5%)	23 (23.0%)	
Caucasian	21 (9.1%)	10 (7.7%)	11 (11.0%)	
Hispanic	79 (34.3%)	33 (25.4%)	46 (46.0%)	
Indian	29 (12.6%)	18 (13.8%)	11 (11.0%)	
Diastolic PBW	172.7 ± 80.5	172.6 ± 82.5	172.9 ± 77.9	0.977
Diastolic PSD	53.0 ± 20.6	53.0 ± 21.4	53.0 ± 19.7	0.987
Diastolic Phase Kurt	8.2 ± 6.8	7.8 ± 6.0	8.7 ± 7.7	0.306
Diastolic Phase Peak	220.1 ± 40.3	220.3 ± 44.1	219.7 ± 34.7	0.904
Diastolic Phase Skewness	2.5 ± 0.8	2.5 ± 0.7	2.5 ± 0.8	0.688
EDE	0.6 ± 0.2	0.6 ± 0.1	0.5 ± 0.2	0.004
EDSI	0.8 ± 0.1	0.8 ± 0.1	0.8 ± 0.1	0.007
LVEDV	259.5 ± 118.9	245.0 ± 109.5	278.4 ± 127.6	0.035
ESE	0.6 ± 0.2	0.6 ± 0.1	0.6 ± 0.2	0.000
ESSI	0.8 ± 0.1	0.8 ± 0.1	0.8 ± 0.1	0.001
LVESV	196.6 ± 109.3	187.9 ± 101.9	208.0 ± 117.3	0.167
LVEF	27.2 ± 10.5	26.2 ± 9.9	28.5 ± 11.1	0.108
Systolic PBW	161.1 ± 77.5	161.5 ± 78.7	160.7 ± 75.9	0.940
Systolic PSD	50.7 ± 20.5	50.6 ± 20.5	50.8 ± 20.4	0.961
Systolic Phase Kurt	8.0 ± 7.1	7.1 ± 4.7	9.1 ± 9.2	0.036
Systolic Phase Peak	131.5 ± 37.4	132.4 ± 40.5	130.3 ± 33.0	0.680
Systolic Phase Skew	2.5 ± 0.8	2.4 ± 0.6	2.5 ± 0.9	0.228
Scar Score	18.2 ± 12.0	15.6 ± 11.1	21.6 ± 12.2	0.000
Stroke Volumne	62.9 ± 22.6	57.1 ± 19.6	70.3 ± 24.0	0.000
Myocardial Mass	217.3 ± 58.3	211.5 ± 55.3	224.8 ± 61.1	0.086

Table 6.2
Results of RL algorithms compared to other methods

Model	Accuracy	Sensitivity	Specificity	AUC
Logit	0.72 ± 0.06	0.81 ± 0.06	0.60 ± 0.10	0.71 ± 0.06
Random Forest	0.66 ± 0.06	0.75 ± 0.08	0.54 ± 0.12	0.64 ± 0.07
MLP	0.52 ± 0.08	0.56 ± 0.43	0.45 ± 0.43	0.51 ± 0.06
RL (binary rewards)	0.64 ± 0.06	0.73 ± 0.09	0.50 ± 0.11	0.61 ± 0.06
RL (relu rewards)	0.61 ± 0.11	0.70 ± 0.13	0.51 ± 0.20	0.61 ± 0.11
RL (sigmoid rewards)	0.62 ± 0.08	0.89 ± 0.09	0.28 ± 0.16	0.58 ± 0.08

Chapter 7

Conclusion

This dissertation sequentially discusses mechanical dyssynchrony, electrical dyssynchrony, electromechanical dyssynchrony, and the method of using reinforcement learning to combine multimodal features to guide the selection of CRT patients and find the optimal LV lead position.

In the clinical setting, this work introduces shape index parameters based on statistical methods, as well as group analyses of ICM and DCM, which outperform traditional clinical features recommended by clinical guidelines in the selection of CRT patients. Additionally, an innovative approach is proposed for using three-dimensional spatial VCG information to describe the characteristics of electrical dyssynchrony, locate the latest activation site, and combine it with the latest mechanical contraction sites to

select the optimal LV lead position. In many medical applications, interpretability is necessary, and this work uses a heat map based on weight parameters to emphasize the regions of interest in the heart and provide visual technology to enable physicians to understand the physical meaning of new features and the reasons behind the clinical decisions made by the artificial intelligent model. This was a multicenter, nonrandomized, retrospective study. The small number of patients is the largest limitation of this study.

Technically, an autoencoder technique is innovatively proposed to describe mechanical dyssynchrony as a new medical feature. This feature significantly outperforms traditional statistical features in selecting CRT patients and fills the gap in describing mechanical dyssynchrony in regions. Additionally, the visualization strategy proposed is beneficial for interpreting new features in the clinical setting. STFT technology is used to transform one-dimensional waveforms into two-dimensional frequency-time spectra. And transfer learning is used to leverage the knowledge learned from a large arrhythmia ECG dataset of related medical conditions to improve the treatment of bizarre medical conditions with limited data, such as CRT in this dissertation. This can improve prediction accuracy, reduce the time and resources required to develop machine learning models, overcome the class imbalance problem, and potentially lead to better patient outcomes. Moreover, deep reinforcement learning is applied to the decision-making problem of CRT patients. Discrete state space/specific action space

models are studied to find the optimal treatment strategy, improve the reward function based on the physician's experience, and learn the approximate value of the best action function, which can improve the treatment strategy used by clinical physicians and provide interpretability to a certain extent. As a future step, it is important to examine the learned policies on a patient-by-patient basis and study other modeling strategies.

Several limitations of this study should be acknowledged. Firstly, this study recruited relatively few patients from two multi-center, retrospective clinical trials, which has inherent limitations in the study design. Secondly, in some experiments, the data came from two different clinical trials (Chapters 4-6), and there were certain errors in the collection and processing of the data by the experimenters. Some clinical parameters were unavailable in the VISION-CRT dataset, such as CKD, and the distribution of patient characteristics, such as QRS morphology, QRS duration, PSD, and PWW, significantly differed between the two datasets. While efforts were made to obtain a diverse and representative sample, the dataset may not fully reflect the population and may have certain biases. Additionally, the size of the dataset may be limited, which could affect the generalizability of the results. Another limitation could be the choice of hyperparameters for the models used, as different values could potentially lead to different performance outcomes. Finally, the evaluation metrics used may not fully capture the real-world effectiveness of the proposed approach and could benefit from further refinement.

References

[1] Azizian N, Rastgou F, Ghaedian T, Golabchi A, Bahadorian B, Khanlarzadeh V, et al. LV dyssynchrony assessed with phase analysis on gated myocardial perfusion SPECT can predict response to CRT in patients with end-stage heart failure. Research in Cardiovascular Medicine. 2014;3(4).

[2] Henneman MM, Chen J, Dibbets-Schneider P, Stokkel MP, Bleeker GB, Ypenburg C, et al. Can LV dyssynchrony as assessed with phase analysis on gated myocardial perfusion SPECT predict response to CRT? Journal of Nuclear Medicine. 2007;48(7):1104-11.

[3] Mukherjee A, Patel CD, Naik N, Sharma G, Roy A. Quantitative assessment of cardiac mechanical dyssynchrony and prediction of response to cardiac resynchronization therapy in patients with non-ischaemic dilated cardiomyopathy using equilibrium radionuclide angiography. Europace. 2016;18(6):851-7.

[4] Zhou W, Hou X, Piccinelli M, Tang X, Tang L, Cao K, et al. 3D fusion of LV

venous anatomy on fluoroscopy venograms with epicardial surface on SPECT myocardial perfusion images for guiding CRT LV lead placement. JACC: Cardiovascular Imaging. 2014;7(12):1239-48.

[5] Benjamin EJ, Muntner P, Alonso A, Bittencourt MS, Callaway CW, Carson AP, et al. Heart disease and stroke statistics—2019 update: a report from the American Heart Association. Circulation. 2019;139(10):e56-e528.

[6] Heidenreich PA, Albert NM, Allen LA, Bluemke DA, Butler J, Fonarow GC, et al. Forecasting the impact of heart failure in the United States: a policy statement from the American Heart Association. Circulation: Heart Failure. 2013;6(3):606-19.

[7] for Disease Control C, Prevention. National vital statistics system: Public Use Data File Documentation: Mortality Multiple Cause-of-Dearth; 2020. Available from: `https://www.cdc.gov/nchs/nvss/mortality_public_use_data.htm` [cited 2022-08-25].

[8] Cleland JG, Daubert JC, Erdmann E, Freemantle N, Gras D, Kappenberger L, et al. The effect of cardiac resynchronization on morbidity and mortality in heart failure. New England Journal of Medicine. 2005;352(15):1539-49.

[9] Zhou W, Garcia EV. Nuclear image-guided approaches for cardiac resynchronization therapy (CRT). Current cardiology reports. 2016;18(1):1-11.

[10] Zou J, Hua W, Su Y, Xu G, Zhen L, Liang Y, et al. SPECT-guided lv lead placement for incremental CRT efficacy: validated by a prospective, randomized, controlled study. JACC: Cardiovascular Imaging. 2019;12(12):2580-3.

[11] Wang L, Zhou W, Liang Y, Yang Y, Garcia EV, Chen J, et al. Right ventricular dyssynchrony in pulmonary hypertension: Phase analysis using FDG-PET imaging. Journal of Nuclear Cardiology. 2017;24(1):69-78.

[12] Bax JJ, Bleeker GB, Marwick TH, Molhoek SG, Boersma E, Steendijk P, et al. Left ventricular dyssynchrony predicts response and prognosis after cardiac resynchronization therapy. Journal of the American College of Cardiology. 2004;44(9):1834-40.

[13] Zhou W, Jiang Z, Chen J, Garcia EV, Li D. Development and validation of a phase analysis tool to measure interventricular mechanical dyssynchrony from gated SPECT MPI. Journal of Nuclear Cardiology. 2017;24(5):1680-6.

[14] Tao N, Qiu Y, Tang H, Qian Z, Wu H, Zhu R, et al. Assessment of left ventricular contraction patterns using gated SPECT MPI to predict cardiac resynchronization therapy response. Journal of Nuclear Cardiology. 2018;25:2029-38.

[15] Donal E, de Chillou C, Magnin-Poull I, Leclercq C. Imaging in cardiac resynchronization therapy: what does the clinician need? Europace. 2008;10(suppl_3):iii70-2.

[16] Vernooy K, Van Deursen CJ, Strik M, Prinzen FW. Strategies to improve cardiac resynchronization therapy. Nature Reviews Cardiology. 2014;11(8):481-93.

[17] White JA, Yee R, Yuan X, Krahn A, Skanes A, Parker M, et al. Delayed enhancement magnetic resonance imaging predicts response to cardiac resynchronization therapy in patients with intraventricular dyssynchrony. Journal of the American College of Cardiology. 2006;48(10):1953-60.

[18] Adelstein EC, Saba S. Scar burden by myocardial perfusion imaging predicts echocardiographic response to cardiac resynchronization therapy in ischemic cardiomyopathy. American heart journal. 2007;153(1):105-12.

[19] Bleeker GB, Bax JJ, Fung JWH, van der Wall EE, Zhang Q, Schalij MJ, et al. Clinical versus echocardiographic parameters to assess response to cardiac resynchronization therapy. The American journal of cardiology. 2006;97(2):260-3.

[20] Ypenburg C, van Bommel RJ, Delgado V, Mollema SA, Bleeker GB, Boersma E, et al. Optimal left ventricular lead position predicts reverse remodeling and survival after cardiac resynchronization therapy. Journal of the American College of Cardiology. 2008;52(17):1402-9.

[21] Murphy RT, Sigurdsson G, Mulamalla S, Agler D, Popovic ZB, Starling RC, et al. Tissue synchronization imaging and optimal left ventricular pacing site

in cardiac resynchronization therapy. The American journal of cardiology. 2006;97(11):1615-21.

[22] Barker WH, Mullooly JP, Getchell W. Changing incidence and survival for heart failure in a well-defined older population, 1970–1974 and 1990–1994. Circulation. 2006;113(6):799-805.

[23] Pouleur AC, Knappe D, Shah AM, Uno H, Bourgoun M, Foster E, et al. Relationship between improvement in left ventricular dyssynchrony and contractile function and clinical outcome with cardiac resynchronization therapy: the MADIT-CRT trial. European heart journal. 2011;32(14):1720-9.

[24] UK NAA, Atherton JJ, Bauersachs J, UK AJC, Carerj S, Ceconi C, et al. 2016 ESC guidelines for the diagnosis and treatment of acute and chronic heart failure. European Heart Journal. 2016;37:2129-200.

[25] Tracy CM, Epstein AE, Darbar D, DiMarco JP, Dunbar SB, Estes NM, et al. 2012 ACCF/AHA/HRS focused update of the 2008 guidelines for device-based therapy of cardiac rhythm abnormalities: a report of the American College of Cardiology Foundation/American Heart Association Task Force on Practice Guidelines. Journal of the American College of Cardiology. 2012;60(14):1297-313.

[26] Choi AJ, Thomas SS, Singh JP. Cardiac resynchronization therapy and implantable cardioverter defibrillator therapy in advanced heart failure. Heart Failure Clinics. 2016;12(3):423-36.

[27] Chung ES, Leon AR, Tavazzi L, Sun JP, Nihoyannopoulos P, Merlino J, et al. Results of the Predictors of Response to CRT (PROSPECT) trial. Circulation. 2008;117(20):2608-16.

[28] Kosmala W, Marwick TH. Meta-analysis of effects of optimization of cardiac resynchronization therapy on left ventricular function, exercise capacity, and quality of life in patients with heart failure. The American journal of cardiology. 2014;113(6):988-94.

[29] Steffel J, Robertson M, Singh JP, Abraham WT, Bax JJ, Borer JS, et al. The effect of QRS duration on cardiac resynchronization therapy in patients with a narrow QRS complex: a subgroup analysis of the EchoCRT trial. European heart journal. 2015;36(30):1983-9.

[30] Young JB, Abraham WT, Smith AL, Leon AR, Lieberman R, Wilkoff B, et al. Combined cardiac resynchronization and implantable cardioversion defibrillation in advanced chronic heart failure: the MIRACLE ICD Trial. Jama. 2003;289(20):2685-94.

[31] Van Der Wall E, Schalij M, Bax J. Cardiac resynchronization therapy; evaluation by advanced imaging techniques. The International Journal of Cardiovascular Imaging. 2010;26(2):199-202.

[32] Auricchio A, Prinzen FW. Non-Responders to Cardiac Resynchronization Therapy–The Magnitude of the Problem and the Issues–. Circulation Journal. 2011;75(3):521-7.

[33] Khidir MJ, Delgado V, Marsan NA, Bax JJ. Mechanical dyssynchrony in patients with heart failure and reduced ejection fraction: how to measure? Current Opinion in Cardiology. 2016;31(5):523-30.

[34] Kloosterman M, Damman K, Van Veldhuisen DJ, Rienstra M, Maass AH. The importance of myocardial contractile reserve in predicting response to cardiac resynchronization therapy. European Journal of Heart Failure. 2017;19(7):862-9.

[35] van't Sant J, Ter Horst I, Wijers S, Mast T, Leenders G, Doevendans P, et al. Measurements of electrical and mechanical dyssynchrony are both essential to improve prediction of CRT response. Journal of Electrocardiology. 2015;48(4):601-8.

[36] Auger D, Bleeker GB, Bertini M, Ewe SH, Van Bommel RJ, Witkowski TG, et al. Effect of cardiac resynchronization therapy in patients without left intraventricular dyssynchrony. European heart journal. 2012;33(7):913-20.

[37] Friehling M, Chen J, Saba S, Bazaz R, Schwartzman D, Adelstein EC, et al. A prospective pilot study to evaluate the relationship between acute change in left ventricular synchrony after cardiac resynchronization therapy and patient outcome using a single-injection gated SPECT protocol. Circulation: Cardiovascular Imaging. 2011;4(5):532-9.

[38] Behar JM, Rajani R, Pourmorteza A, Preston R, Razeghi O, Niederer S, et al. Comprehensive use of cardiac computed tomography to guide left ventricular lead placement in cardiac resynchronization therapy. Heart Rhythm. 2017;14(9):1364-72.

[39] Bleeker GB, Kaandorp TA, Lamb HJ, Boersma E, Steendijk P, de Roos A, et al. Effect of posterolateral scar tissue on clinical and echocardiographic improvement after cardiac resynchronization therapy. Circulation. 2006;113(7):969-76.

[40] Huntjens PR, Walmsley J, Ploux S, Bordachar P, Prinzen FW, Delhaas T, et al. Influence of left ventricular lead position relative to scar location on response to cardiac resynchronization therapy: a model study. Europace. 2014;16(suppl_4):iv62-8.

[41] Boogers MJ, Chen J, van Bommel RJ, Borleffs C, Dibbets-Schneider P, van der Hiel B, et al. Optimal left ventricular lead position assessed with phase analysis on gated myocardial perfusion SPECT. European journal of nuclear medicine and molecular imaging. 2011;38(2):230-8.

[42] Lin X, Xu H, Zhao X, Chen J. Sites of latest mechanical activation as assessed by SPECT myocardial perfusion imaging in ischemic and dilated cardiomyopathy patients with LBBB. European journal of nuclear medicine and molecular imaging. 2014;41(6):1232-9.

[43] Zhang X, Qian Z, Tang H, Hua W, Su Y, Xu G, et al. A new method to recommend left ventricular lead positions for improved CRT volumetric response and long-term prognosis. Journal of Nuclear Cardiology. 2021;28(2):672-84.

[44] Khan FZ, Virdee MS, Palmer CR, Pugh PJ, O'Halloran D, Elsik M, et al. Targeted left ventricular lead placement to guide cardiac resynchronization therapy: the TARGET study: a randomized, controlled trial. Journal of the American College of Cardiology. 2012;59(17):1509-18.

[45] Kydd AC, Khan FZ, Watson WD, Pugh PJ, Virdee MS, Dutka DP. Prognostic benefit of optimum left ventricular lead position in cardiac resynchronization therapy: follow-up of the TARGET Study Cohort (Targeted Left Ventricular Lead Placement to guide Cardiac Resynchronization Therapy). JACC: Heart Failure. 2014;2(3):205-12.

[46] Bai R, Di Biase L, Mohanty P, Hesselson AB, De Ruvo E, Gallagher PL, et al. Positioning of left ventricular pacing lead guided by intracardiac echocardiography with vector velocity imaging during cardiac resynchronization therapy procedure. Journal of Cardiovascular Electrophysiology. 2011;22(9):1034-41.

[47] Saba S, Marek J, Schwartzman D, Jain S, Adelstein E, White P, et al. Echocardiography-guided left ventricular lead placement for cardiac resynchronization therapy: results of the Speckle Tracking Assisted Resynchronization Therapy for Electrode Region trial. Circulation: Heart Failure. 2013;6(3):427-34.

[48] Bax JJ, Abraham T, Barold SS, Breithardt OA, Fung JW, Garrigue S, et al. Cardiac resynchronization therapy: part 1—issues before device implantation. Journal of the American College of Cardiology. 2005;46(12):2153-67.

[49] Marechaux S, Menet A, Guyomar Y, Ennezat PV, Guerbaai RA, Graux P, et al. Role of echocardiography before cardiac resynchronization therapy: new advances and current developments. Echocardiography. 2016;33(11):1745-52.

[50] Spartalis M, Tzatzaki E, Spartalis E, Damaskos C, Athanasiou A, Livanis E, et al. The role of echocardiography in the optimization of cardiac resynchronization therapy: current evidence and future perspectives. The Open Cardiovascular Medicine Journal. 2017;11:133.

[51] Yu CM, Sanderson JE, Marwick TH, Oh JK. Tissue Doppler imaging: a new prognosticator for cardiovascular diseases. Journal of the American College of Cardiology. 2007;49(19):1903-14.

[52] Tavard F, Simon A, Leclercq C, Donal E, Hernández AI, Garreau M. Multimodal registration and data fusion for cardiac resynchronization therapy optimization. IEEE Transactions on Medical Imaging. 2014;33(6):1363-72.

[53] Bank AJ, Kaufman CL, Kelly AS, Burns KV, Adler SW, Rector TS, et al. Results of the prospective Minnesota study of ECHO/TDI in cardiac resynchronization therapy (PROMISE-CRT) study. Journal of cardiac failure. 2009;15(5):401-9.

[54] Sassone B, Nucifora G, Mele D, Valzania C, Bisignani G, Boriani G, et al. Role of cardiovascular imaging in cardiac resynchronization therapy: a literature review. Journal of Cardiovascular Medicine. 2018;19(5):211-22.

[55] Truong QA, Szymonifka J, Picard MH, Thai We, Wai B, Cheung JW, et al. Utility of dual-source computed tomography in cardiac resynchronization therapy—DIRECT study. Heart rhythm. 2018;15(8):1206-13.

[56] Casas-Rojo E, Fernandez-Golfin C, Garcia-Martin A, Gorissen W, Zamorano Gomez JL. Fusion between cardiac venous coronary computed tomography and three-dimensional speckle-tracking for selecting the appropriate vein for resynchronization therapy. European Heart Journal-Cardiovascular Imaging. 2016;17(8):947-7.

[57] Fyenbo DB, Sommer A, Kühl JT, Kofoed KF, Nørgaard BL, Kronborg MB, et al. Transmural Myocardial Scar Assessed by Cardiac Computed Tomography:

Predictor of Echocardiographic Versus Clinical Response to Cardiac Resynchronization Therapy? Journal of Computer Assisted Tomography. 2019;43(2):312-6.

[58] Gould J, Behar J, Rajani R, Sieniewicz B, Porter B, Claridge S, et al. P333 Dual energy cardiac computed tomography to guide cardiac resynchronisation therapy: a feasibility study using coronary venous anatomy, scar and strain to guide optimal left ventricular lead placement. EP Europace. 2018;20(suppl_1):i53-4.

[59] Bellenger NG, Davies LC, Francis JM, Coats AJ, Pennell DJ. Reduction in sample size for studies of remodeling in heart failure by the use of cardiovascular magnetic resonance. Journal of Cardiovascular Magnetic Resonance. 2000;2(4):271-8.

[60] Kühl HP, Spuentrup E, Wall A, Franke A, Schröder J, Heussen N, et al. Assessment of myocardial function with interactive non–breath-hold real-time MR imaging: comparison with echocardiography and breath-hold cine MR imaging. Radiology. 2004;231(1):198-207

[61] Chalil S, Stegemann B, Muhyaldeen S, Khadjooi K, Foley P, Smith R, et al. Effect of posterolateral left ventricular scar on mortality and morbidity following cardiac resynchronization therapy. Pacing and Clinical Electrophysiology. 2007;30(10):1201-9.

[62] Chalil S, Stegemann B, Muhyaldeen S, Khadjooi K, Smith RE, Jordan PJ, et al. Intraventricular dyssynchrony predicts mortality and morbidity after cardiac resynchronization therapy: a study using cardiovascular magnetic resonance tissue synchronization imaging. Journal of the American College of Cardiology. 2007;50(3):243-52.

[63] Leyva F. The role of cardiovascular magnetic resonance in cardiac resynchronization therapy. Heart Failure Clinics. 2017;13(1):63-77.

[64] Ypenburg C, Schalij MJ, Bleeker GB, Steendijk P, Boersma E, Dibbets-Schneider P, et al. Impact of viability and scar tissue on response to cardiac resynchronization therapy in ischaemic heart failure patients. European heart journal. 2007;28(1):33-41.

[65] Adelstein EC, Tanaka H, Soman P, Miske G, Haberman SC, Saba SF, et al. Impact of scar burden by single-photon emission computed tomography myocardial perfusion imaging on patient outcomes following cardiac resynchronization therapy. European heart journal. 2011;32(1):93-103.

[66] Xu YZ, Cha YM, Feng D, Powell BD, Wiste HJ, Hua W, et al. Impact of myocardial scarring on outcomes of cardiac resynchronization therapy: extent or location? Journal of Nuclear Medicine. 2012;53(1):47-54.

[67] Bose A, Kandala J, Upadhyay GA, Riedl L, Ahmado I, Padmanabhan R, et al.

Impact of myocardial viability and left ventricular lead location on clinical outcome in cardiac resynchronization therapy recipients with ischemic cardiomyopathy. Journal of cardiovascular electrophysiology. 2014;25(5):507-13.

[68] Rahmim A, Zaidi H. PET versus SPECT: strengths, limitations and challenges. Nuclear medicine communications. 2008;29(3):193-207.

[69] Pazhenkottil AP, Buechel RR, Nkoulou R, Ghadri JR, Herzog BA, Husmann L, et al. Left ventricular dyssynchrony assessment by phase analysis from gated PET-FDG scans. Journal of nuclear cardiology. 2011;18(5):920-5.

[70] Lehner S, Uebleis C, Schüßler F, Haug A, Kääb S, Bartenstein P, et al. The amount of viable and dyssynchronous myocardium is associated with response to cardiac resynchronization therapy: initial clinical results using multiparametric ECG-gated [18F] FDG PET. European journal of nuclear medicine and molecular imaging. 2013;40(12):1876-83.

[71] Uebleis C, Ulbrich M, Tegtmeyer R, Schuessler F, Haserueck N, Siebermair J, et al. Electrocardiogram-gated 18F-FDG PET/CT hybrid imaging in patients with unsatisfactory response to cardiac resynchronization therapy: initial clinical results. Journal of Nuclear Medicine. 2011;52(1):67-71.

[72] Chen J, Garcia EV, Folks RD, Cooke CD, Faber TL, Tauxe EL, et al. Onset of left ventricular mechanical contraction as determined by phase analysis of ECG-gated myocardial perfusion SPECT imaging: development of a diagnostic

tool for assessment of cardiac mechanical dyssynchrony. Journal of nuclear cardiology. 2005;12(6):687-95.

[73] Chen J, Garcia EV, Bax JJ, Iskandrian AE, Borges-Neto S, Soman P. SPECT myocardial perfusion imaging for the assessment of left ventricular mechanical dyssynchrony. Journal of Nuclear Cardiology. 2011;18:685-94.

[74] Chen J, Faber TL, Cooke CD, Garcia EV. Temporal resolution of multiharmonic phase analysis of ECG-gated myocardial perfusion SPECT studies. Journal of nuclear cardiology. 2008;15(3):383-91.

[75] Trimble MA, Velazquez EJ, Adams GL, Honeycutt EF, Pagnanelli RA, Barnhart HX, et al. Repeatability and reproducibility of phase analysis of gated single-photon emission computed tomography myocardial perfusion imaging used to quantify cardiac dyssynchrony. Nuclear medicine communications. 2008;29(4):374.

[76] Lin X, Xu H, Zhao X, Folks RD, Garcia EV, Soman P, et al. Repeatability of left ventricular dyssynchrony and function parameters in serial gated myocardial perfusion SPECT studies. Journal of nuclear cardiology. 2010;17(5):811-6.

[77] Cheung A, Zhou Y, Faber TL, Garcia EV, Zhu L, Chen J. The performance of phase analysis of gated SPECT myocardial perfusion imaging in the presence of perfusion defects: A simulation study. Journal of Nuclear Cardiology. 2012;19(3):500-6.

[78] Zhou W, Hung GU. Left-ventricular mechanical dyssynchrony in the prognosis of dilated cardiomyopathy: Which parameter is more useful? Journal of Nuclear Cardiology. 2018;25(5):1688-91.

[79] Kano N, Okumura T, Isobe S, Sawamura A, Watanabe N, Fukaya K, et al. Left ventricular phase entropy: Novel prognostic predictor in patients with dilated cardiomyopathy and narrow QRS. Journal of Nuclear Cardiology. 2018;25(5):1677-87.

[80] Wang C, Tang H, Zhu F, Jiang Z, Shi J, Zhou Y, et al. Prognostic value of left-ventricular systolic and diastolic dyssynchrony measured from gated SPECT MPI in patients with dilated cardiomyopathy. Journal of Nuclear Cardiology. 2020;27(5):1582-91.

[81] Zhou W, Tao N, Hou X, Wang Y, Folks RD, Cooke DC, et al. Development and validation of an automatic method to detect the latest contracting viable left ventricular segments to assist guide CRT therapy from gated SPECT myocardial perfusion imaging. Journal of Nuclear Cardiology. 2018;25(6):1948-57.

[82] Schuster I, Habib G, Jego C, Thuny F, Avierinos JF, Derumeaux G, et al. Diastolic asynchrony is more frequent than systolic asynchrony in dilated cardiomyopathy and is less improved by cardiac resynchronization therapy. Journal of the American College of Cardiology. 2005;46(12):2250-7.

[83] Sharir T. What is the value of motion and thickening in gated myocardial perfusion SPECT?. Springer; 2018.

[84] Cooke CD, Garcia EV, Cullom SJ, Faber TL, Pettigrew RI. Determining the accuracy of calculating systolic wall thickening using a fast Fourier transform approximation: a simulation study based on canine and patient data. Journal of Nuclear Medicine. 1994;35(7):1185-92.

[85] Nowak B, Stellbrink C, Schaefer WM, Sinha AM, Breithardt OA, Kaiser HJ, et al. Comparison of regional myocardial blood flow and perfusion in dilated cardiomyopathy and left bundle branch block: role of wall thickening. Journal of Nuclear Medicine. 2004;45(3):414-8.

[86] Gendre R, Lairez O, Mondoly P, Duparc A, Carrié D, Galinier M, et al. Research of predictive factors for cardiac resynchronization therapy: a prospective study comparing data from phase-analysis of gated myocardial perfusion single-photon computed tomography and echocardiography. Annals of nuclear medicine. 2017;31(3):218-26.

[87] Peix A, Karthikeyan G, Massardo T, Kalaivani M, Patel C, Pabon LM, et al. Value of intraventricular dyssynchrony assessment by gated-SPECT myocardial perfusion imaging in the management of heart failure patients undergoing cardiac resynchronization therapy (VISION-CRT). Journal of Nuclear Cardiology. 2021;28(1):55-64.

[88] Koos R, Sinha AM, Markus K, Breithardt OA, Mischke K, Zarse M, et al. Comparison of left ventricular lead placement via the coronary venous approach versus lateral thoracotomy in patients receiving cardiac resynchronization therapy. The American journal of cardiology. 2004;94(1):59-63.

[89] Mair H, Sachweh J, Meuris B, Nollert G, Schmoeckel M, Schuetz A, et al. Surgical epicardial left ventricular lead versus coronary sinus lead placement in biventricular pacing. European journal of cardio-thoracic surgery. 2005;27(2):235-42.

[90] Singh JP, Klein HU, Huang DT, Reek S, Kuniss M, Quesada A, et al. Left ventricular lead position and clinical outcome in the Multicenter Automatic Defibrillator Implantation Trial–Cardiac Resynchronization Therapy (MADIT-CRT) trial. Circulation. 2011;123(11):1159-66.

[91] Dekker A, Phelps B, Dijkman B, van Der Nagel T, van Der Veen F, Geskes G, et al. Epicardial left ventricular lead placement for cardiac resynchronization therapy: optimal pace site selection with pressure-volume loops. The Journal of thoracic and cardiovascular surgery. 2004;127(6):1641-7.

[92] Tada T, Osuda K, Nakata T, Muranaka I, Himeno M, Muratsubaki S, et al. A novel approach to the selection of an appropriate pacing position for optimal cardiac resynchronization therapy using CT coronary venography and myocardial perfusion imaging: FIVE STaR method (fusion image using CT coronary

venography and perfusion SPECT applied for cardiac resynchronization therapy). Journal of Nuclear Cardiology. 2021;28(4):1438-45.

[93] Cobb DB, Gold MR. Computer modeling: the future of cardiac resynchronization therapy patient selection?. Am Heart Assoc; 2018.

[94] Garcia EV, Klein JL, Moncayo V, Cooke CD, Del'Aune C, Folks R, et al. Diagnostic performance of an artificial intelligence-driven cardiac-structured reporting system for myocardial perfusion SPECT imaging. Journal of Nuclear Cardiology. 2020;27(5):1652-64.

[95] Haro Alonso D, Wernick MN, Yang Y, Germano G, Berman DS, Slomka P. Prediction of cardiac death after adenosine myocardial perfusion SPECT based on machine learning. Journal of Nuclear Cardiology. 2019;26(5):1746-54.

[96] Motwani M, Dey D, Berman DS, Germano G, Achenbach S, Al-Mallah MH, et al. Machine learning for prediction of all-cause mortality in patients with suspected coronary artery disease: a 5-year multicentre prospective registry analysis. European heart journal. 2017;38(7):500-7.

[97] Arsanjani R, Xu Y, Dey D, Vahistha V, Shalev A, Nakanishi R, et al. Improved accuracy of myocardial perfusion SPECT for detection of coronary artery disease by machine learning in a large population. Journal of Nuclear Cardiology. 2013;20(4):553-62.

[98] Schmitz B, De Maria R, Gatsios D, Chrysanthakopoulou T, Landolina M, Gasparini M, et al. Identification of genetic markers for treatment success in heart failure patients: insight from cardiac resynchronization therapy. Circulation: Cardiovascular Genetics. 2014;7(6):760-70.

[99] Peressutti D, Sinclair M, Bai W, Jackson T, Ruijsink J, Nordsletten D, et al. A framework for combining a motion atlas with non-motion information to learn clinically useful biomarkers: application to cardiac resynchronisation therapy response prediction. Medical image analysis. 2017;35:669-84.

[100] Kalscheur MM, Kipp RT, Tattersall MC, Mei C, Buhr KA, DeMets DL, et al. Machine learning algorithm predicts cardiac resynchronization therapy outcomes: lessons from the COMPANION trial. Circulation: Arrhythmia and Electrophysiology. 2018;11(1):e005499.

[101] Cikes M, Sanchez-Martinez S, Claggett B, Duchateau N, Piella G, Butakoff C, et al. Machine learning-based phenogrouping in heart failure to identify responders to cardiac resynchronization therapy. European journal of heart failure. 2019;21(1):74-85.

[102] Chen XW, Lin X. Big data deep learning: challenges and perspectives. IEEE access. 2014;2:514-25.

[103] Wang T, Lei Y, Tang H, He Z, Castillo R, Wang C, et al. A learning-based automatic segmentation and quantification method on left ventricle in gated

myocardial perfusion SPECT imaging: A feasibility study. Journal of Nuclear Cardiology. 2020;27(3):976-87.

[104] Betancur J, Commandeur F, Motlagh M, Sharir T, Einstein AJ, Bokhari S, et al. Deep learning for prediction of obstructive disease from fast myocardial perfusion SPECT: a multicenter study. JACC: Cardiovascular Imaging. 2018;11(11):1654-63.

[105] Shrestha S, Sengupta PP. Machine learning for nuclear cardiology: The way forward. Springer; 2019.

[106] Mnih V, Kavukcuoglu K, Silver D, Rusu AA, Veness J, Bellemare MG, et al. Human-level control through deep reinforcement learning. nature. 2015;518(7540):529-33.

[107] Littman ML. Reinforcement learning improves behaviour from evaluative feedback. Nature. 2015;521(7553):445-51.

[108] Yu C, Liu J, Nemati S, Yin G. Reinforcement learning in healthcare: A survey. ACM Computing Surveys (CSUR). 2021;55(1):1-36.

[109] Nath S, Korot E, Fu DJ, Zhang G, Mishra K, Lee AY, et al. Reinforcement learning in ophthalmology: potential applications and challenges to implementation. The Lancet Digital Health. 2022.

[110] Weng L. An Overview of Deep Learning for Curious People; 2017.

[111] Van Buuren S. Flexible imputation of missing data. CRC press; 2018.

[112] Josse J, Prost N, Scornet E, Varoquaux G. On the consistency of supervised learning with missing values. arXiv preprint arXiv:190206931. 2019.

[113] Sillanmäki S, Lipponen JA, Tarvainen MP, Laitinen T, Hedman M, Hedman A, et al. Relationships between electrical and mechanical dyssynchrony in patients with left bundle branch block and healthy controls. Journal of Nuclear Cardiology. 2019;26(4):1228-39.

[114] He Z, de Amorim Fernandes F, do Nascimento EA, Garcia EV, Mesquita CT, Zhou W. Incremental value of left ventricular shape parameters measured by gated SPECT MPI in predicting the super-response to CRT. Journal of Nuclear Cardiology. 2022;29(4):1537-46. See Appendix A for a copy of the copyright transfer agreement.

[115] He Z, Li D, Cui C, Qin Hy, Zhao Z, Hou X, et al. Predictive values of left ventricular mechanical dyssynchrony for CRT response in heart failure patients with different pathophysiology. Journal of Nuclear Cardiology. 2021:1-12. See Appendix A for a copy of the copyright transfer agreement.

[116] Burchfield JS, Xie M, Hill JA. Pathological ventricular remodeling: mechanisms: part 1 of 2. Circulation. 2013;128(4):388-400.

[117] Xie M, Burchfield JS, Hill JA. Pathological ventricular remodeling: therapies: part 2 of 2. Circulation. 2013;128(9):1021-30.

[118] Udelson JE, Konstam MA. Ventricular remodeling: fundamental to the progression (and regression) of heart failure. American College of Cardiology Foundation Washington, DC; 2011.

[119] Azevedo PS, Polegato BF, Minicucci MF, Paiva SA, Zornoff LA. Cardiac remodeling: concepts, clinical impact, pathophysiological mechanisms and pharmacologic treatment. Arquivos brasileiros de cardiologia. 2015;106:62-9.

[120] Knap B, Južnič G, Bren A, Drzewiecki G, Noordergraaf A. Elongation as a new shape index for the left ventricle. The International Journal of Cardiovascular Imaging. 2002;18(6):421-30.

[121] Cohn JN, Ferrari R, Sharpe N, an International Forum on Cardiac Remodeling. Cardiac remodeling—concepts and clinical implications: a consensus paper from an international forum on cardiac remodeling. Journal of the American College of Cardiology. 2000;35(3):569-82.

[122] Nappi C, Gaudieri V, Acampa W, Assante R, Zampella E, Mainolfi CG, et al. Comparison of left ventricular shape by gated SPECT imaging in diabetic and nondiabetic patients with normal myocardial perfusion: a propensity score analysis. Journal of Nuclear Cardiology. 2018;25(2):394-403.

[123] Nitta K, Kurisu S, Erasta R, Sumimoto Y, Ikenaga H, Ishibashi K, et al. Associations of left ventricular shape with left ventricular volumes and functions

assessed by ECG-gated SPECT in patients without significant perfusion abnormality. Heart and Vessels. 2020;35(1):86-91.

[124] Gimelli A, Liga R, Clemente A, Marras G, Kusch A, Marzullo P. Left ventricular eccentricity index measured with SPECT myocardial perfusion imaging: An additional parameter of adverse cardiac remodeling. Journal of Nuclear Cardiology. 2020;27(1):71-9.

[125] Gimelli A, Liga R, Giorgetti A, Casagranda M, Marzullo P. Stress-induced alteration of left ventricular eccentricity: An additional marker of multivessel CAD. Journal of Nuclear Cardiology. 2019;26(1):227-32.

[126] Germano G, Slomka PJ. Assessing LV remodeling in nuclear cardiology. Springer; 2019.

[127] Abidov A, Slomka PJ, Nishina H, Hayes SW, Kang X, Yoda S, et al. Left ventricular shape index assessed by gated stress myocardial perfusion SPECT: initial description of a new variable. Journal of nuclear cardiology. 2006;13(5):652-9.

[128] Alexanderson-Rosas E, Espinola-Zavaleta N, Garcia EV, Peix A, Massardo T, Pabon LM, et al. Diastolic dyssynchrony assessment by gated myocardial perfusion-SPECT in subjects who underwent cardiac resynchronization therapy. Journal of Nuclear Cardiology. 2021;28(4):1413-21.

[129] Antonio N, Teixeira R, Coelho L, Lourenço C, Monteiro P, Ventura M, et al. Identification of 'super-responders' to cardiac resynchronization therapy: the

importance of symptom duration and left ventricular geometry. Europace. 2009;11(3):343-9.

[130] Gasparini M, Regoli F, Ceriotti C, Galimberti P, Bragato R, De Vita S, et al. Remission of left ventricular systolic dysfunction and of heart failure symptoms after cardiac resynchronization therapy: temporal pattern and clinical predictors. American heart journal. 2008;155(3):507-14.

[131] Jimenez-Heffernan A, Butt S, Mesquita CT, Massardo T, Peix A, Kumar A, et al. Technical aspects of gated SPECT MPI assessment of left ventricular dyssynchrony used in the VISION-CRT study. Journal of Nuclear Cardiology. 2021;28(3):1165-71.

[132] Seabold S, Perktold J. Statsmodels: Econometric and statistical modeling with python. In: Proceedings of the 9th Python in Science Conference. vol. 57. Austin, TX; 2010. p. 10-25080.

[133] Zecchin M, Proclemer A, Magnani S, Vitali-Serdoz L, Facchin D, Muser D, et al. Long-term outcome of 'super-responder'patients to cardiac resynchronization therapy. Europace. 2014;16(3):363-71.

[134] Ambale-Venkatesh B, Yoneyama K, Sharma RK, Ohyama Y, Wu CO, Burke GL, et al. Left ventricular shape predicts different types of cardiovascular events in the general population. Heart. 2017;103(7):499-507.

[135] Levine YC, Matos J, Rosenberg MA, Manning WJ, Josephson ME, Buxton AE. Left ventricular sphericity independently predicts appropriate implantable cardioverter-defibrillator therapy. Heart Rhythm. 2016;13(2):490-7.

[136] St John Sutton M, Pfeffer MA, Plappert T, Rouleau JL, Moyé LA, Dagenais GR, et al. Quantitative two-dimensional echocardiographic measurements are major predictors of adverse cardiovascular events after acute myocardial infarction. The protective effects of captopril. Circulation. 1994;89(1):68-75.

[137] Bulava A, Lukl J, Škvařilová M, Marek D. Dramatically improved left ventricular function after biventricular pacemaker implantation—a case report. European journal of heart failure. 2005;7(2):231-3.

[138] Rickard J, Kumbhani DJ, Popovic Z, Verhaert D, Manne M, Sraow D, et al. Characterization of super-response to cardiac resynchronization therapy. Heart Rhythm. 2010;7(7):885-9.

[139] Killu AM, Grupper A, Friedman PA, Powell BD, Asirvatham SJ, Espinosa RE, et al. Predictors and outcomes of "super-response" to cardiac resynchronization therapy. Journal of cardiac failure. 2014;20(6):379-86.

[140] Ypenburg C, van Bommel RJ, Borleffs CJW, Bleeker GB, Boersma E, Schalij MJ, et al. Long-term prognosis after cardiac resynchronization therapy is related to the extent of left ventricular reverse remodeling at midterm follow-up. Journal of the American College of Cardiology. 2009;53(6):483-90.

[141] Fei L, Keeling P, Gill J, Bashir Y, Statters D, Poloniecki J, et al. Heart rate variability and its relation to ventricular arrhythmias in congestive heart failure. Heart. 1994;71(4):322-8.

[142] Fornwalt BK, Sprague WW, BeDell P, Suever JD, Gerritse B, Merlino JD, et al. Agreement is poor among current criteria used to define response to cardiac resynchronization therapy. Circulation. 2010;121(18):1985-91.

[143] Tsai SC, Chang YC, Chiang KF, Lin WY, Huang JL, Hung GU, et al. LV dyssynchrony is helpful in predicting ventricular arrhythmia in ischemic cardiomyopathy after cardiac resynchronization therapy: A preliminary study. Medicine. 2016;95(7).

[144] Pazhenkottil AP, Buechel RR, Husmann L, Nkoulou RN, Wolfrum M, Ghadri JR, et al. Long-term prognostic value of left ventricular dyssynchrony assessment by phase analysis from myocardial perfusion imaging. Heart. 2011;97(1):33-7.

[145] Wang L, Yang MF, Cai M, Zhao SH, He ZX, Wang YT. Prognostic significance of left ventricular dyssynchrony by phase analysis of gated SPECT in medically treated patients with dilated cardiomyopathy. Clinical nuclear medicine. 2013;38(7):510-5.

[146] Wang C, Shi J, Ge J, Tang H, He Z, Liu Y, et al. Left ventricular systolic and diastolic dyssynchrony to improve cardiac resynchronization therapy response

in heart failure patients with dilated cardiomyopathy. Journal of Nuclear Cardiology. 2021;28(3):1023-36.

[147] Elliott P, Andersson B, Arbustini E, Bilinska Z, Cecchi F, Charron P, et al. Classification of the cardiomyopathies: a position statement from the European Society Of Cardiology Working Group on Myocardial and Pericardial Diseases. European heart journal. 2008;29(2):270-6.

[148] Chen J, Kalogeropoulos AP, Verdes L, Butler J, Garcia EV. Left-ventricular systolic and diastolic dyssynchrony as assessed by multi-harmonic phase analysis of gated SPECT myocardial perfusion imaging in patients with end-stage renal disease and normal LVEF. Journal of Nuclear Cardiology. 2011;18(2):299-308.

[149] Goldberg AS, Alraies MC, Cerqueira MD, Jaber WA, AlJaroudi WA. Prognostic value of left ventricular mechanical dyssynchrony by phase analysis in patients with non-ischemic cardiomyopathy with ejection fraction 35-50% and QRS¡ 150 ms. Journal of Nuclear Cardiology. 2014;21(1):57-66.

[150] Peix A, Padrón K, Cabrera LO, Castañeda O, Milán D, Castro J, et al. Intraventricular synchronism assessment by gated-SPECT myocardial perfusion imaging in cardiac resynchronization therapy. Does cardiomyopathy type influence results? EJNMMI research. 2020;10(1):1-11.

[151] Ludwig DR, Friehling M, Schelbert EB, Schwartzman D. Impact of scar on SPECT assay of left ventricular contraction dyssynchrony. European journal of nuclear medicine and molecular imaging. 2014;41(3):529-35.

[152] Yokoshiki H, Mitsuyama H, Watanabe M, Mitsuhashi T, Shimizu A. Cardiac resynchronization therapy in ischemic and non-ischemic cardiomyopathy. Journal of arrhythmia. 2017;33(5):410-6.

[153] AlJaroudi W, Alraies MC, Menon V, Brunken RC, Cerqueira MD, Jaber WA. Predictors and incremental prognostic value of left ventricular mechanical dyssynchrony response during stress-gated positron emission tomography in patients with ischemic cardiomyopathy. Journal of Nuclear Cardiology. 2012;19(5):958-69.

[154] O'Connell JW, Schreck C, Moles M, Badwar N, DeMarco T, Olgin J, et al. A unique method by which to quantitate synchrony with equilibrium radionuclide angiography. Journal of Nuclear Cardiology. 2005;12(4):441-50.

[155] Van Kriekinge SD, Nishina H, Ohba M, Berman DS, Germano G. Automatic global and regional phase analysis from gated myocardial perfusion SPECT imaging: application to the characterization of ventricular contraction in patients with left bundle branch block. Journal of Nuclear Medicine. 2008;49(11):1790-7.

[156] Nakajima K, Okuda K, Matsuo S, Kiso K, Kinuya S, Garcia EV. Comparison of phase dyssynchrony analysis using gated myocardial perfusion imaging with four software programs: Based on the Japanese Society of Nuclear Medicine working group normal database. Journal of Nuclear Cardiology. 2017;24(2):611-21.

[157] Tajik AJ. Machine learning for echocardiographic imaging: embarking on another incredible journey. American College of Cardiology Foundation Washington, DC; 2016.

[158] Bengio Y, Courville A, Vincent P. Representation learning: A review and new perspectives. IEEE transactions on pattern analysis and machine intelligence. 2013;35(8):1798-828.

[159] Betancur J, Rubeaux M, Fuchs TA, Otaki Y, Arnson Y, Slipczuk L, et al. Automatic valve plane localization in myocardial perfusion SPECT/CT by machine learning: Anatomic and clinical validation. Journal of Nuclear Medicine. 2017;58(6):961-7.

[160] LeCun Y, Bengio Y, Hinton G, et al. Deep learning. nature, 521 (7553), 436-444. Google Scholar Google Scholar Cross Ref Cross Ref. 2015.

[161] Esteva A, Kuprel B, Novoa RA, Ko J, Swetter SM, Blau HM, et al. Dermatologist-level classification of skin cancer with deep neural networks. nature. 2017;542(7639):115-8.

[162] Xu Y, Mo T, Feng Q, Zhong P, Lai M, Eric I, et al. Deep learning of feature representation with multiple instance learning for medical image analysis. In: 2014 IEEE international conference on acoustics, speech and signal processing (ICASSP). IEEE; 2014. p. 1626-30.

[163] Bax JJ, Marwick TH, Molhoek SG, Bleeker GB, Van Erven L, Boersma E, et al. Left ventricular dyssynchrony predicts benefit of cardiac resynchronization therapy in patients with end-stage heart failure before pacemaker implantation. The American journal of cardiology. 2003;92(10):1238-40.

[164] Henzlova MJ, Cerqueira MD, Hansen CL, Taillefer R, Yao S. ASNC imaging guidelines for nuclear cardiology procedures: stress protocols and tracers. J Nucl Cardiol. 2009;16(2):331.

[165] Goodfellow I, Bengio Y, Courville A. Deep learning. MIT press; 2016.

[166] Zhang Y, Chen W, Yeo CK, Lau CT, Lee BS. Detecting rumors on online social networks using multi-layer autoencoder. In: 2017 IEEE Technology & Engineering Management Conference (TEMSCON). IEEE; 2017. p. 437-41.

[167] Paszke A, Gross S, Massa F, Lerer A, Bradbury J, Chanan G, et al. Pytorch: An imperative style, high-performance deep learning library. Advances in neural information processing systems. 2019;32.

[168] Nakamura K, Takami M, Shimabukuro M, Maesato A, Chinen I, Ishigaki S, et al. Effective prediction of response to cardiac resynchronization therapy

using a novel program of gated myocardial perfusion single photon emission computed tomography. Europace. 2011;13(12):1731-7.

[169] Spicker P. The real dependent variable problem: The limitations of quantitative analysis in comparative policy studies. Social Policy & Administration. 2018;52(1):216-28.

[170] Chen M, Shi X, Zhang Y, Wu D, Guizani M. Deep feature learning for medical image analysis with convolutional autoencoder neural network. IEEE Transactions on Big Data. 2017;7(4):750-8.

[171] Petch J, Di S, Nelson W. Opening the black box: the promise and limitations of explainable machine learning in cardiology. Canadian Journal of Cardiology. 2021.

[172] Guidi JL, Clark K, Upton MT, Faust H, Umscheid CA, Lane-Fall MB, et al. Clinician perception of the effectiveness of an automated early warning and response system for sepsis in an academic medical center. Annals of the American Thoracic Society. 2015;12(10):1514-9.

[173] Becker M, Altiok E, Ocklenburg C, Krings R, Adams D, Lysansky M, et al. Analysis of LV lead position in cardiac resynchronization therapy using different imaging modalities. JACC: Cardiovascular Imaging. 2010;3(5):472-81.

[174] Mizunobu M, Sakai J, Sasao H, Murai H, Fujiwara H. Assessment of Left

Ventricular Systolic and Diastolic Function Using ECG-Gated Technetium-99m Tetrofosmin Myocardial Perfusion SPECT Comparison With Ultrasound Echocardiography. International heart journal. 2013;54(4):212-5.

[175] Garg N, Dresser T, Aggarwal K, Gupta V, Mittal MK, Alpert MA. Comparison of left ventricular ejection fraction values obtained using invasive contrast left ventriculography, two-dimensional echocardiography, and gated single-photon emission computed tomography. SAGE Open Medicine. 2016;4:2050312116655940.

[176] Gimelli A, Landi P, Marraccini P, Sicari R, Frumento P, L'Abbate A, et al. Left ventricular ejection fraction measurements: accuracy and prognostic implications in a large population of patients with known or suspected ischemic heart disease. The International Journal of Cardiovascular Imaging. 2008;24(8):793-801.

[177] Shojaeifard M, Ghaedian T, Yaghoobi N, Malek H, Firoozabadi H, Bitarafan-Rajabi A, et al. Comparison of gated SPECT myocardial perfusion imaging with echocardiography for the measurement of left ventricular volumes and ejection fraction in patients with severe heart failure. Research in cardiovascular medicine. 2016;5(1).

[178] Engels EB, Mafi-Rad M, van Stipdonk AM, Vernooy K, Prinzen FW. Why QRS duration should be replaced by better measures of electrical activation

to improve patient selection for cardiac resynchronization therapy. Journal of Cardiovascular Translational Research. 2016;9(4):257-65.

[179] Carità P, Corrado E, Pontone G, Curnis A, Bontempi L, Novo G, et al. Non-responders to cardiac resynchronization therapy: Insights from multimodality imaging and electrocardiography. A brief review. International Journal of Cardiology. 2016;225:402-7.

[180] Hawkins NM, Petrie MC, MacDonald MR, Hogg KJ, McMurray JJ. Selecting patients for cardiac resynchronization therapy: electrical or mechanical dyssynchrony? European heart journal. 2006;27(11):1270-81.

[181] Delgado V, Bax JJ. Assessment of systolic dyssynchrony for cardiac resynchronization therapy is clinically useful. Circulation. 2011;123(6):640-55.

[182] Jia P, Ramanathan C, Ghanem RN, Ryu K, Varma N, Rudy Y. Electrocardiographic imaging of cardiac resynchronization therapy in heart failure: observation of variable electrophysiologic responses. Heart rhythm. 2006;3(3):296-310.

[183] Vatasescu R, Berruezo A, Mont L, Tamborero D, Sitges M, Silva E, et al. Midterm 'super-response'to cardiac resynchronization therapy by biventricular pacing with fusion: insights from electro-anatomical mapping. Europace. 2009;11(12):1675-82.

[184] Moody GB, Mark RG. The impact of the MIT-BIH arrhythmia database. IEEE Engineering in Medicine and Biology Magazine. 2001;20(3):45-50.

[185] Goldberger AL, Amaral LA, Glass L, Hausdorff JM, Ivanov PC, Mark RG, et al. PhysioBank, PhysioToolkit, and PhysioNet: components of a new research resource for complex physiologic signals. circulation. 2000;101(23):e215-20.

[186] Beela AS, Ünlü S, Duchenne J, Ciarka A, Daraban AM, Kotrc M, et al. Assessment of mechanical dyssynchrony can improve the prognostic value of guideline-based patient selection for cardiac resynchronization therapy. European Heart Journal-Cardiovascular Imaging. 2019;20(1):66-74.

[187] Engelse WA, Zeelenberg C. A single scan algorithm for QRS-detection and feature extraction. Computers in cardiology. 1979;6(1979):37-42.

[188] Elgendi M, Eskofier B, Dokos S, Abbott D. Revisiting QRS detection methodologies for portable, wearable, battery-operated, and wireless ECG systems. PloS one. 2014;9(1):e84018.

[189] Allen J. Short term spectral analysis, synthesis, and modification by discrete Fourier transform. IEEE Transactions on Acoustics, Speech, and Signal Processing. 1977;25(3):235-8.

[190] Smith III JO. Spectral audio signal processing. (No Title). 2011.

[191] Haykin S, Veen B. Signals and Systems, John Willey & Sons. Inc New York. 1999.

[192] Huang J, Chen B, Yao B, He W. ECG arrhythmia classification using STFT-based spectrogram and convolutional neural network. IEEE access. 2019;7:92871-80.

[193] Virtanen P, Gommers R, Oliphant TE, Haberland M, Reddy T, Cournapeau D, et al. SciPy 1.0: fundamental algorithms for scientific computing in Python. Nature methods. 2020;17(3):261-72.

[194] He K, Zhang X, Ren S, Sun J. Deep residual learning for image recognition. In: Proceedings of the IEEE conference on computer vision and pattern recognition; 2016. p. 770-8.

[195] Attia ZI, Kapa S, Lopez-Jimenez F, McKie PM, Ladewig DJ, Satam G, et al. Screening for cardiac contractile dysfunction using an artificial intelligence–enabled electrocardiogram. Nature medicine. 2019;25(1):70-4.

[196] Hua X, Han J, Zhao C, Tang H, He Z, Chen Q, et al. A novel method for ECG signal classification via one-dimensional convolutional neural network. Multimedia Systems. 2020:1-13.

[197] Baeßler B, Mannil M, Maintz D, Alkadhi H, Manka R. Texture analysis and machine learning of non-contrast T1-weighted MR images in patients with hypertrophic cardiomyopathy—preliminary results. European journal of radiology. 2018;102:61-7.

[198] Van Steenkiste G, van Loon G, Crevecoeur G. Transfer learning in ECG classification from human to horse using a novel parallel neural network architecture. Scientific Reports. 2020;10(1):186.

[199] Weimann K, Conrad TO. Transfer learning for ECG classification. Scientific reports. 2021;11(1):1-12.

[200] Abdeldayem SS, Bourlai T. ECG-based human authentication using high-level spectro-temporal signal features. In: 2018 IEEE international conference on big data (big data). IEEE; 2018. p. 4984-93.

[201] Gupta V, Mittal M. QRS complex detection using STFT, chaos analysis, and PCA in standard and real-time ECG databases. Journal of The Institution of Engineers (India): Series B. 2019;100(5):489-97.

[202] Ponikowski P, Voors AA, Anker SD, Bueno H, Cleland JG, Coats AJ, et al. 2016 ESC Guidelines for the diagnosis and treatment of acute and chronic heart failure. Kardiologia Polska (Polish Heart Journal). 2016;74(10):1037-147.

[203] Abraham WT, Fisher WG, Smith AL, Delurgio DB, Leon AR, Loh E, et al. Cardiac resynchronization in chronic heart failure. New England Journal of Medicine. 2002;346(24):1845-53.

[204] Sieniewicz BJ, Gould J, Porter B, Sidhu BS, Behar JM, Claridge S, et al. Optimal site selection and image fusion guidance technology to facilitate cardiac resynchronization therapy. Expert review of medical devices. 2018;15(8):555-70.

[205] Regoli F, Auricchio A. The role of invasive mapping in the electrophysiology laboratory. Europace. 2009;11(suppl_5):v40-5.

[206] Boogers MM, Van Kriekinge SD, Henneman MM, Ypenburg C, Van Bommel RJ, Boersma E, et al. Quantitative gated SPECT–derived phase analysis on gated myocardial perfusion SPECT detects left ventricular dyssynchrony and predicts response to cardiac resynchronization therapy. Journal of Nuclear Medicine. 2009;50(5):718-25.

[207] Riera ARP, Uchida AH, Ferreira Filho C, Meneghini A, Ferreira C, Schapacknik E, et al. Significance of vectorcardiogram in the cardiological diagnosis of the 21st century. Clinical cardiology. 2007;30(7):319.

[208] Man S, Maan AC, Schalij MJ, Swenne CA. Vectorcardiographic diagnostic & prognostic information derived from the 12-lead electrocardiogram: Historical review and clinical perspective. Journal of electrocardiology. 2015;48(4):463-75.

[209] Kors J, Van Herpen G, Sittig A, Van Bemmel J. Reconstruction of the Frank vectorcardiogram from standard electrocardiographic leads: diagnostic comparison of different methods. European heart journal. 1990;11(12):1083-92.

[210] Edenbrandt L, Pahlm O. Vectorcardiogram synthesized from a 12-lead ECG: superiority of the inverse Dower matrix. Journal of electrocardiology. 1988;21(4):361-7.

[211] Jaros R, Martinek R, Danys L. Comparison of different electrocardiography with vectorcardiography transformations. Sensors. 2019;19(14):3072.

[212] Mafi Rad M, Blaauw Y, Dinh T, Pison L, Crijns HJ, Prinzen FW, et al. Left ventricular lead placement in the latest activated region guided by coronary venous electroanatomic mapping. Ep Europace. 2015;17(1):84-93.

[213] Mafi Rad M, Blaauw Y, Dinh T, Pison L, Crijns HJ, Prinzen FW, et al. Different regions of latest electrical activation during left bundle-branch block and right ventricular pacing in cardiac resynchronization therapy patients determined by coronary venous electro-anatomic mapping. European journal of heart failure. 2014;16(11):1214-22.

[214] Giorgi C, Nadeau R, Primeau R, Campa M, Cardinal R, Shenasa M, et al. Comparative accuracy of the vectorcardiogram and electrocardiogram in the localization of the accessory pathway in patients with Wolff-Parkinson-White syndrome: validation of a new vectorcardiographic algorithm by intraoperative epicardial mapping and electrophysiologic studies. American Heart Journal. 1990;119(3):592-8.

[215] Rad MM, Wijntjens GW, Engels EB, Blaauw Y, Luermans JG, Pison L, et al. Vectorcardiographic QRS area identifies delayed left ventricular lateral wall activation determined by electroanatomic mapping in candidates for cardiac resynchronization therapy. Heart Rhythm. 2016;13(1):217-25.

[216] Adelstein E, Alam MB, Schwartzman D, Jain S, Marek J, Gorcsan J, et al. Effect of echocardiography-guided left ventricular lead placement for cardiac resynchronization therapy on mortality and risk of defibrillator therapy for ventricular arrhythmias in heart failure patients (from the Speckle Tracking Assisted Resynchronization Therapy for Electrode Region [STARTER] trial). The American Journal of Cardiology. 2014;113(9):1518-22.

[217] Kočková R, Sedláček K, Wichterle D, Šikula V, Tintěra J, Jansová H, et al. Cardiac resynchronization therapy guided by cardiac magnetic resonance imaging: A prospective, single-centre randomized study (CMR-CRT). International Journal of Cardiology. 2018;270:325-30.

[218] Bilchick KC, Dimaano V, Wu KC, Helm RH, Weiss RG, Lima JA, et al. Cardiac magnetic resonance assessment of dyssynchrony and myocardial scar predicts function class improvement following cardiac resynchronization therapy. JACC: Cardiovascular Imaging. 2008;1(5):561-8.

[219] Panayiotou M, Mountney P, Brost A, Toth D, Jackson T, Behar JM, et al. Dynamic mapping of ventricular function from cardiovascular magnetic resonance imaging. In: 2016 38th Annual International Conference of the IEEE Engineering in Medicine and Biology Society (EMBC). IEEE; 2016. p. 4137-40.

[220] Pourmorteza A, Schuleri KH, Herzka DA, Lardo AC, McVeigh ER. A new method for cardiac computed tomography regional function assessment: stretch

quantifier for endocardial engraved zones (SQUEEZ). Circulation: Cardiovascular Imaging. 2012;5(2):243-50.

[221] Butter C, Georgi C, Stockburger M. Optimal CRT Implantation—Where and How To Place the Left-Ventricular Lead? Current Heart Failure Reports. 2021:1-16.

[222] Badran HA, Kamel JZ, Mohamed TR, Abdelhamid MA. Using three-dimensional echocardiography to guide left ventricle lead position in cardiac resynchronization therapy: does it make any difference. Journal of Interventional Cardiac Electrophysiology. 2017;48:299-306.

[223] Albatat M, King DR, Unger LA, Arevalo H, Wall S, Sundnes J, et al. Electromechanical model to predict cardiac resynchronization therapy. In: 2018 40th Annual International Conference of the IEEE Engineering in Medicine and Biology Society (EMBC). IEEE; 2018. p. 5446-59.

[224] Bunting E, Lambrakos L, Kemper P, Whang W, Garan H, Konofagou E. Imaging the propagation of the electromechanical wave in heart failure patients with cardiac resynchronization therapy. Pacing and Clinical Electrophysiology. 2017;40(1):35-45.

[225] National Academies of Sciences E, Medicine, et al. Improving diagnosis in health care. National Academies Press; 2015.

[226] Rai SK, Sowmya K. A Review on Use of Machine Learning Techniques in Diagnostic Health-Care. Artificial Intelligent Systems and Machine Learning. 2018;10(4):102-7.

[227] Fatima M, Pasha M, et al. Survey of machine learning algorithms for disease diagnostic. Journal of Intelligent Learning Systems and Applications. 2017;9(01):1.

[228] Chui KT, Alhalabi W, Pang SSH, Pablos POd, Liu RW, Zhao M. Disease diagnosis in smart healthcare: Innovation, technologies and applications. Sustainability. 2017;9(12):2309.

[229] Lipton ZC, Kale DC, Elkan C, Wetzel R. Learning to diagnose with LSTM recurrent neural networks. arXiv preprint arXiv:151103677. 2015.

[230] Choi E, Bahadori MT, Sun J, Kulas J, Schuetz A, Stewart W. Retain: An interpretable predictive model for healthcare using reverse time attention mechanism. Advances in neural information processing systems. 2016;29.

[231] Goodwin TR, Harabagiu SM. Medical question answering for clinical decision support. In: Proceedings of the 25th ACM international on conference on information and knowledge management; 2016. p. 297-306.

[232] Ling Y, Hasan SA, Datla V, Qadir A, Lee K, Liu J, et al. Diagnostic inferencing via improving clinical concept extraction with deep reinforcement learning: A

preliminary study. In: Machine Learning for Healthcare Conference. PMLR; 2017. p. 271-85.

[233] Taylor GW. A reinforcement learning framework for parameter control in computer vision applications. In: First Canadian Conference on Computer and Robot Vision, 2004. Proceedings. IEEE; 2004. p. 496-503.

[234] Sahba F, Tizhoosh HR, Salama MM. A reinforcement learning framework for medical image segmentation. In: The 2006 IEEE international joint conference on neural network proceedings. IEEE; 2006. p. 511-7.

[235] Sahba F, Tizhoosh HR, Salama MM. Application of opposition-based reinforcement learning in image segmentation. In: 2007 IEEE symposium on computational intelligence in image and signal processing. IEEE; 2007. p. 246-51.

[236] Sahba F, Tizhoosh HR, Salama M. Application of reinforcement learning for segmentation of transrectal ultrasound images. BMC medical imaging. 2008;8(1):1-10.

[237] Sahba F. Object segmentation in image sequences using reinforcement learning. In: 2016 International Conference on Computational Science and Computational Intelligence (CSCI). IEEE; 2016. p. 1416-7.

[238] Liu D, Jiang T. Deep reinforcement learning for surgical gesture segmentation and classification. In: International conference on medical image computing and computer-assisted intervention. Springer; 2018. p. 247-55.

[239] Netto SMB, Leite VRC, Silva AC, de Paiva AC, de Almeida Neto A. Application on reinforcement learning for diagnosis based on medical image. Reinforcement learning. 2008;379.

[240] Lv E, Liu W, Wen P, Kang X. Classification of Benign and Malignant Lung Nodules Based on Deep Convolutional Network Feature Extraction. Journal of Healthcare Engineering. 2021;2021:1-11.

[241] Sutton RS, Barto AG. Reinforcement learning: An introduction. MIT press; 2018.

[242] Tsitsiklis JN. Asynchronous stochastic approximation and Q-learning. Machine learning. 1994;16(3):185-202.

[243] Komorowski M, Celi LA, Badawi O, Gordon AC, Faisal AA. The artificial intelligence clinician learns optimal treatment strategies for sepsis in intensive care. Nature medicine. 2018;24(11):1716-20.

[244] Jiang N, Li L. Doubly robust off-policy value evaluation for reinforcement learning. In: International Conference on Machine Learning. PMLR; 2016. p. 652-61.

[245] Ribeiro MT, Singh S, Guestrin C. " Why should i trust you?" Explaining the predictions of any classifier. In: Proceedings of the 22nd ACM SIGKDD international conference on knowledge discovery and data mining; 2016. p. 1135-44.

[246] Lundberg SM, Lee SI. A unified approach to interpreting model predictions. Advances in neural information processing systems. 2017;30.

[247] Friedman JH. Greedy function approximation: a gradient boosting machine. Annals of statistics. 2001:1189-232.

[248] Becker M, Franke A, Breithardt OA, Ocklenburg C, Kaminski T, Kramann R, et al. Impact of left ventricular lead position on the efficacy of cardiac resynchronisation therapy: a two-dimensional strain echocardiography study. Heart. 2007;93(10):1197-203.

[249] Becker M, Hoffmann R, Schmitz F, Hundemer A, Kühl H, Schauerte P, et al. Relation of optimal lead positioning as defined by three-dimensional echocardiography to long-term benefit of cardiac resynchronization. The American Journal of Cardiology. 2007;100(11):1671-6.

[250] Kapetanakis S, Bhan A, Murgatroyd F, Kearney MT, Gall N, Zhang Q, et al. Real-time 3D echo in patient selection for cardiac resynchronization therapy. JACC: Cardiovascular Imaging. 2011;4(1):16-26.

[251] Mele D, Toselli T, Capasso F, Stabile G, Piacenti M, Piepoli M, et al. Comparison of myocardial deformation and velocity dyssynchrony for identification of responders to cardiac resynchronization therapy. European journal of heart failure. 2009;11(4):391-9.

[252] Suffoletto MS, Dohi K, Cannesson M, Saba S, Gorcsan III J. Novel speckle-tracking radial strain from routine black-and-white echocardiographic images to quantify dyssynchrony and predict response to cardiac resynchronization therapy. Circulation. 2006;113(7):960-8.

[253] Tamborero D, Vidal B, Tolosana JM, Sitges M, Berruezo A, Silva E, et al. Electrocardiographic versus echocardiographic optimization of the interventricular pacing delay in patients undergoing cardiac resynchronization therapy. Journal of Cardiovascular Electrophysiology. 2011;22(10):1129-34.

[254] Steenkiste GV, van Loon G, Crevecoeur G. Transfer Learning in ECG Classification from Human to Horse Using a Novel Parallel Neural Network Architecture. Scientific Reports. 2020 jan;10(1). Available from: https://doi.org/10.1038%2Fs41598-019-57025-2.

[255] Inc TM. MATLAB version: 9.13.0 (R2022b). Natick, Massachusetts, United States: The MathWorks Inc.; 2022. Available from: https://www.mathworks.com.

[256] Zhang Y, Li J, Wei S, Zhou F, Li D. Heartbeats classification using hybrid time-frequency analysis and transfer learning based on ResNet. IEEE Journal of Biomedical and Health Informatics. 2021;25(11):4175-84.

[257] Ahuja S, Panigrahi BK, Dey N, Rajinikanth V, Gandhi TK. Deep transfer

learning-based automated detection of COVID-19 from lung CT scan slices. Applied Intelligence. 2021;51:571-85.

[258] He Z, Garcia EV, Zhou W. Nuclear Image-Guided Methods for Cardiac Resynchronization Therapy. Nuclear Cardiology: Basic and Advanced Concepts in Clinical Practice. 2021:587-608. See Appendix A for a copy of the copyright transfer agreement.

[259] He Z, Zhang X, Zhao C, Ling X, Malhotra S, Qian Z, et al. A method using deep learning to discover new predictors from left-ventricular mechanical dyssynchrony for CRT response. Journal of Nuclear Cardiology. 2022:1-13. See Appendix A for a copy of the copyright transfer agreement.

[260] Alansary A, Oktay O, Li Y, Le Folgoc L, Hou B, Vaillant G, et al. Evaluating reinforcement learning agents for anatomical landmark detection. Medical image analysis. 2019;53:156-64.

[261] Etcheverry M, Georgescu B, Odry B, Re TJ, Kaushik S, Geiger B, et al. Nonlinear adaptively learned optimization for object localization in 3D medical images. In: Deep Learning in Medical Image Analysis and Multimodal Learning for Clinical Decision Support. Springer; 2018. p. 254-62.

[262] Jiang F, Jiang Y, Zhi H, Dong Y, Li H, Ma S, et al. Artificial intelligence in healthcare: past, present and future. Stroke and vascular neurology. 2017;2(4).

[263] Wei Z, Liu Q, Peng B, Tou H, Chen T, Huang XJ, et al. Task-oriented dialogue system for automatic diagnosis. In: Proceedings of the 56th Annual Meeting of the Association for Computational Linguistics (Volume 2: Short Papers); 2018. p. 201-7.

[264] Tang F, Lin K, Uchendu I, Dodge HH, Zhou J. Improving mild cognitive impairment prediction via reinforcement learning and dialogue simulation. arXiv preprint arXiv:180206428. 2018.

[265] Ghesu FC, Georgescu B, Mansi T, Neumann D, Hornegger J, Comaniciu D. An artificial agent for anatomical landmark detection in medical images. In: International conference on medical image computing and computer-assisted intervention. Springer; 2016. p. 229-37.

[266] Coronato A, Naeem M, De Pietro G, Paragliola G. Reinforcement learning for intelligent healthcare applications: A survey. Artificial Intelligence in Medicine. 2020;109:101964.

[267] Ghesu FC, Georgescu B, Grbic S, Maier A, Hornegger J, Comaniciu D. Towards intelligent robust detection of anatomical structures in incomplete volumetric data. Medical image analysis. 2018;48:203-13.

[268] Ghesu FC, Georgescu B, Zheng Y, Grbic S, Maier A, Hornegger J, et al. Multi-scale deep reinforcement learning for real-time 3D-landmark detection

in CT scans. IEEE transactions on pattern analysis and machine intelligence. 2017;41(1):176-89.

[269] De Chazal P, O'Dwyer M, Reilly RB. Automatic classification of heartbeats using ECG morphology and heartbeat interval features. IEEE transactions on biomedical engineering. 2004;51(7):1196-206.

[270] Wiering MA, Van Otterlo M. Reinforcement learning. Adaptation, learning, and optimization. 2012;12(3):729.

[271] Nguyen T, Li Z, Spiegler V, Ieromonachou P, Lin Y. Big data analytics in supply chain management: A state-of-the-art literature review. Computers & Operations Research. 2018;98:254-64.

[272] Tian Y, Zhang P, Li X, Gao Y, Zhu T, Wang L, et al. True complete left bundle branch block morphology strongly predicts good response to cardiac resynchronization therapy. Europace. 2013;15(10):1499-506.

[273] Zareba W, Klein H, Cygankiewicz I, Hall WJ, McNitt S, Brown M, et al. Effectiveness of cardiac resynchronization therapy by QRS morphology in the multicenter automatic defibrillator implantation trial–cardiac resynchronization therapy (MADIT-CRT). Circulation. 2011;123(10):1061-72.

[274] Cleland JG, Abraham WT, Linde C, Gold MR, Young JB, Claude Daubert J,

et al. An individual patient meta-analysis of five randomized trials assessing the effects of cardiac resynchronization therapy on morbidity and mortality in patients with symptomatic heart failure. European heart journal. 2013;34(46):3547-56.

[275] Healey JS, Hohnloser SH, Exner DV, Birnie DH, Parkash R, Connolly SJ, et al. Cardiac resynchronization therapy in patients with permanent atrial fibrillation: results from the Resynchronization for Ambulatory Heart Failure Trial (RAFT). Circulation: Heart Failure. 2012;5(5):566-70.

[276] Gold MR, Thébault C, Linde C, Abraham WT, Gerritse B, Ghio S, et al. Effect of QRS duration and morphology on cardiac resynchronization therapy outcomes in mild heart failure: results from the Resynchronization Reverses Remodeling in Systolic Left Ventricular Dysfunction (REVERSE) study. Circulation. 2012;126(7):822-9.

[277] Cleland J, Daubert J, Erdmann E, Freemantle N, Gras D, Kappenberger L, et al. The CARE-HF study (CArdiac REsynchronisation in Heart Failure study): rationale, design and end-points. European journal of heart failure. 2001;3(4):481-9.

[278] Hannun AY, Rajpurkar P, Haghpanahi M, Tison GH, Bourn C, Turakhia MP, et al. Cardiologist-level arrhythmia detection and classification in ambulatory electrocardiograms using a deep neural network. Nature medicine.

2019;25(1):65-9.

[279] van Deursen CJ, Vernooy K, Dudink E, Bergfeldt L, Crijns HJ, Prinzen FW, et al. Vectorcardiographic QRS area as a novel predictor of response to cardiac resynchronization therapy. Journal of Electrocardiology. 2015;48(1):45-52.

[280] Hsu TH, Huang WS, Chen CC, Hung GU, Chen TC, Kao CH, et al. Left ventricular systolic and diastolic dyssynchrony assessed by phase analysis of gated SPECT myocardial perfusion imaging: a comparison with speckle tracking echocardiography. Annals of nuclear medicine. 2013;27(8):764-71.

[281] Sweeney MO, van Bommel RJ, Schalij MJ, Borleffs CJW, Hellkamp AS, Bax JJ. Analysis of ventricular activation using surface electrocardiography to predict left ventricular reverse volumetric remodeling during cardiac resynchronization therapy. Circulation. 2010;121(5):626-34.

[282] van Stipdonk AM, Ter Horst I, Kloosterman M, Engels EB, Rienstra M, Crijns HJ, et al. QRS area is a strong determinant of outcome in cardiac resynchronization therapy. Circulation: Arrhythmia and Electrophysiology. 2018;11(12):e006497.

[283] Zweerink A, Wu L, De Roest G, Nijveldt R, De Cock C, Van Rossum A, et al. Improved patient selection for cardiac resynchronization therapy by normalization of QRS duration to left ventricular dimension. In: EUROPEAN HEART

JOURNAL. vol. 37. OXFORD UNIV PRESS GREAT CLARENDON ST, OXFORD OX2 6DP, ENGLAND; 2016. p. 1294-5.

[284] Wang C, Ma Y, Liu Y, Li L, Cui C, Qin H, et al. Texture analysis of SPECT myocardial perfusion provides prognostic value for dilated cardiomyopathy. Journal of Nuclear Cardiology. 2022:1-12.

[285] ;.

[286] Watkins CJ, Dayan P. Q-learning. Machine learning. 1992;8(3):279-92.

[287] Behar JM, Claridge S, Jackson T, Sieniewicz B, Porter B, Webb J, et al. The role of multi modality imaging in selecting patients and guiding lead placement for the delivery of cardiac resynchronization therapy. Expert review of cardiovascular therapy. 2017;15(2):93-107.

[288] Group JJW, et al. Guidelines for diagnosis and treatment of patients with vasospastic angina (coronary spastic angina)(JCS 2008)–digest version–. Circulation Journal. 2010;74(8):1745-62.

[289] Magro M, Nauta S, Simsek C, Onuma Y, Garg S, van der Heide E, et al. Value of the SYNTAX score in patients treated by primary percutaneous coronary intervention for acute ST-elevation myocardial infarction: The MI SYNTAXscore study. American heart journal. 2011;161(4):771-81.

Appendix A

Letters of Permission

SPRINGER NATURE LICENSE TERMS AND CONDITIONS

Mar 09, 2023

This Agreement between Zhuo He ("You") and Springer Nature ("Springer Nature") consists of your license details and the terms and conditions provided by Springer Nature and Copyright Clearance Center.

License Number	5504801306487
License date	Mar 09, 2023
Licensed Content Publisher	Springer Nature
Licensed Content Publication	Springer eBook
Licensed Content Title	Nuclear Image-Guided Methods for Cardiac Resynchronization Therapy
Licensed Content Author	Zhuo He, Ernest V. Garcia, Weihua Zhou
Licensed Content Date	Jan 1, 2021
Type of Use	Thesis/Dissertation
Requestor type	academic/university or research institute
Format	print and electronic
Portion	full article/chapter
Will you be translating?	no
Circulation/distribution	1 - 29
Author of this Springer Nature content	yes
Title	Knowledge discovery on the integrative analysis of electrical and mechanical dyssynchrony to improve cardiac resynchronization therapy
Institution name	Michigan Technological University
Expected presentation date	Apr 2023
Requestor Location	Zhuo He 1809 Woodmar Dr HOUGHTON, MI 49931 United States Attn: Zhuo He
Billing Type	Invoice
Billing Address	Zhuo He 1809 Woodmar Dr HOUGHTON, MI 49931 United States Attn: Zhuo He
Total	**0.00 USD**

Terms and Conditions

Springer Nature Customer Service Centre GmbH Terms and Conditions

The following terms and conditions ("Terms and Conditions") together with the terms specified in your [RightsLink] constitute the License ("License") between you as Licensee and Springer Nature Customer Service Centre GmbH as Licensor. By clicking 'accept' and completing the transaction for your use of the material ("Licensed Material"), you confirm your acceptance of and obligation to be bound by these Terms and Conditions.

1. Grant and Scope of License

1. 1. The Licensor grants you a personal, non-exclusive, non-transferable, non-sublicensable, revocable, world-wide License to reproduce, distribute, communicate to the public, make available, broadcast, electronically transmit or create derivative works using the Licensed Material for the purpose(s) specified in your RightsLink Licence Details only. Licenses are granted for the specific use requested in the order and for no other use, subject to these Terms and Conditions. You acknowledge and agree that the rights granted to you under this License do not include the right to modify, edit, translate, include in collective works, or create derivative works of the Licensed Material in whole or in part unless expressly stated in your RightsLink Licence Details. You may use the Licensed Material only as permitted under this Agreement and will not reproduce, distribute, display, perform, or otherwise use or exploit any Licensed Material in any way, in whole or in part, except as expressly permitted by this License.

1. 2. You may only use the Licensed Content in the manner and to the extent permitted by these Terms and Conditions, by your RightsLink Licence Details and by any applicable laws.

1. 3. A separate license may be required for any additional use of the Licensed Material, e.g. where a license has been purchased for print use only, separate permission must be obtained for electronic re-use. Similarly, a License is only valid in the language selected and does not apply for editions in other languages unless additional translation rights have been granted separately in the License.

1. 4. Any content within the Licensed Material that is owned by third parties is expressly excluded from the License.

1. 5. Rights for additional reuses such as custom editions, computer/mobile applications, film or TV reuses and/or any other derivative rights requests require additional permission and may be subject to an additional fee. Please apply to journalpermissions@springernature.com or bookpermissions@springernature.com for these rights.

2. Reservation of Rights

Licensor reserves all rights not expressly granted to you under this License. You acknowledge and agree that nothing in this License limits or restricts Licensor's rights in or use of the Licensed Material in any way. Neither this License, nor any act, omission, or statement by Licensor or you, conveys any ownership right to you in any Licensed Material, or to any element or portion thereof. As between Licensor and you, Licensor owns and retains all right, title, and interest in and to the Licensed Material subject to the license granted in Section 1.1. Your permission to use the Licensed Material is expressly conditioned on you not impairing Licensor's or the applicable copyright owner's rights in the Licensed Material in any way.

3. Restrictions on use

3. 1. Minor editing privileges are allowed for adaptations for stylistic purposes or formatting purposes provided such alterations do not alter the original meaning or intention of the Licensed Material and the new figure(s) are still accurate and representative of the Licensed Material. Any other changes including but not limited to, cropping, adapting, and/or omitting material that affect the meaning, intention or moral rights of the author(s) are strictly prohibited.

3. 2. You must not use any Licensed Material as part of any design or trademark.

3. 3. Licensed Material may be used in Open Access Publications (OAP), but any such reuse must include a clear acknowledgment of this permission visible at the same time as the figures/tables/illustration or abstract and which must indicate that the Licensed Material is not part of the governing OA license but has been reproduced with permission. This may be indicated according to any standard referencing system but must include at a minimum 'Book/Journal title, Author, Journal Name (if applicable), Volume (if applicable), Publisher, Year, reproduced with permission from SNCSC'.

4. STM Permission Guidelines

4. 1. An alternative scope of license may apply to signatories of the STM Permissions Guidelines ("STM PG") as amended from time to time and made available at https://www.stm-assoc.org/intellectual-property/permissions/permissions-guidelines/.

4. 2. For content reuse requests that qualify for permission under the STM PG, and which may be updated from time to time, the STM PG supersede the terms and conditions contained in this License.

4. 3. If a License has been granted under the STM PG, but the STM PG no longer apply at the time of publication, further permission must be sought from the Rightsholder. Contact journalpermissions@springernature.com or

bookpermissions@springernature.com for these rights.

5. Duration of License

5. 1. Unless otherwise indicated on your License, a License is valid from the date of purchase ("License Date") until the end of the relevant period in the below table:

Reuse in a medical communications project	Reuse up to distribution or time period indicated in License
Reuse in a dissertation/thesis	Lifetime of thesis
Reuse in a journal/magazine	Lifetime of journal/magazine
Reuse in a book/textbook	Lifetime of edition
Reuse on a website	1 year unless otherwise specified in the License
Reuse in a presentation/slide kit/poster	Lifetime of presentation/slide kit/poster. Note: publication whether electronic or in print of presentation/slide kit/poster may require further permission.
Reuse in conference proceedings	Lifetime of conference proceedings
Reuse in an annual report	Lifetime of annual report
Reuse in training/CME materials	Reuse up to distribution or time period indicated in License
Reuse in newsmedia	Lifetime of newsmedia
Reuse in coursepack/classroom materials	Reuse up to distribution and/or time period indicated in license

6. Acknowledgement

6. 1. The Licensor's permission must be acknowledged next to the Licensed Material in print. In electronic form, this acknowledgement must be visible at the same time as the figures/tables/illustrations or abstract and must be hyperlinked to the journal/book's homepage.

6. 2. Acknowledgement may be provided according to any standard referencing system and at a minimum should include "Author, Article/Book Title, Journal name/Book imprint, volume, page number, year, Springer Nature".

7. Reuse in a dissertation or thesis

7. 1. Where 'reuse in a dissertation/thesis' has been selected, the following terms apply: Print rights of the Version of Record are provided for; electronic rights for use only on institutional repository as defined by the Sherpa guideline (www.sherpa.ac.uk/romeo/) and only up to what is required by the awarding institution.

7. 2. For theses published under an ISBN or ISSN, separate permission is required. Please contact journalpermissions@springernature.com or bookpermissions@springernature.com for these rights.

7. 3. Authors must properly cite the published manuscript in their thesis according to current citation standards and include the following acknowledgement: '*Reproduced with permission from Springer Nature*'.

8. License Fee

You must pay the fee set forth in the License Agreement (the "License Fees"). All amounts payable by you under this License are exclusive of any sales, use, withholding, value added or similar taxes, government fees or levies or other assessments. Collection and/or remittance of such taxes to the relevant tax authority shall be the responsibility of the party who has the legal obligation to do so.

9. Warranty

9. 1. The Licensor warrants that it has, to the best of its knowledge, the rights to license reuse of the Licensed Material. **You are solely responsible for ensuring that the material you wish to license is original to the Licensor and does not carry the copyright of another entity or third party (as credited in the published version).** If the credit line on

any part of the Licensed Material indicates that it was reprinted or adapted with permission from another source, then you should seek additional permission from that source to reuse the material.

9. 2. EXCEPT FOR THE EXPRESS WARRANTY STATED HEREIN AND TO THE EXTENT PERMITTED BY APPLICABLE LAW, LICENSOR PROVIDES THE LICENSED MATERIAL "AS IS" AND MAKES NO OTHER REPRESENTATION OR WARRANTY. LICENSOR EXPRESSLY DISCLAIMS ANY LIABILITY FOR ANY CLAIM ARISING FROM OR OUT OF THE CONTENT, INCLUDING BUT NOT LIMITED TO ANY ERRORS, INACCURACIES, OMISSIONS, OR DEFECTS CONTAINED THEREIN, AND ANY IMPLIED OR EXPRESS WARRANTY AS TO MERCHANTABILITY OR FITNESS FOR A PARTICULAR PURPOSE. IN NO EVENT SHALL LICENSOR BE LIABLE TO YOU OR ANY OTHER PARTY OR ANY OTHER PERSON OR FOR ANY SPECIAL, CONSEQUENTIAL, INCIDENTAL, INDIRECT, PUNITIVE, OR EXEMPLARY DAMAGES, HOWEVER CAUSED, ARISING OUT OF OR IN CONNECTION WITH THE DOWNLOADING, VIEWING OR USE OF THE LICENSED MATERIAL REGARDLESS OF THE FORM OF ACTION, WHETHER FOR BREACH OF CONTRACT, BREACH OF WARRANTY, TORT, NEGLIGENCE, INFRINGEMENT OR OTHERWISE (INCLUDING, WITHOUT LIMITATION, DAMAGES BASED ON LOSS OF PROFITS, DATA, FILES, USE, BUSINESS OPPORTUNITY OR CLAIMS OF THIRD PARTIES), AND WHETHER OR NOT THE PARTY HAS BEEN ADVISED OF THE POSSIBILITY OF SUCH DAMAGES. THIS LIMITATION APPLIES NOTWITHSTANDING ANY FAILURE OF ESSENTIAL PURPOSE OF ANY LIMITED REMEDY PROVIDED HEREIN.

10. Termination and Cancellation

10. 1. The License and all rights granted hereunder will continue until the end of the applicable period shown in Clause 5.1 above. Thereafter, this license will be terminated and all rights granted hereunder will cease.

10. 2. Licensor reserves the right to terminate the License in the event that payment is not received in full or if you breach the terms of this License.

11. General

11. 1. The License and the rights and obligations of the parties hereto shall be construed, interpreted and determined in accordance with the laws of the Federal Republic of Germany without reference to the stipulations of the CISG (United Nations Convention on Contracts for the International Sale of Goods) or to Germany´s choice-of-law principle.

11. 2. The parties acknowledge and agree that any controversies and disputes arising out of this License shall be decided exclusively by the courts of or having jurisdiction for Heidelberg, Germany, as far as legally permissible.

11. 3. This License is solely for Licensor's and Licensee's benefit. It is not for the benefit of any other person or entity.

Questions? For questions on Copyright Clearance Center accounts or website issues please contact springernaturesupport@copyright.com or +1-855-239-3415 (toll free in the US) or +1-978-646-2777. For questions on Springer Nature licensing please visit https://www.springernature.com/gp/partners/rights-permissions-third-party-distribution

Other Conditions:

Version 1.4 - Dec 2022

Questions? E-mail us at customercare@copyright.com.

SPRINGER NATURE LICENSE TERMS AND CONDITIONS

Mar 08, 2023

This Agreement between Zhuo He ("You") and Springer Nature ("Springer Nature") consists of your license details and the terms and conditions provided by Springer Nature and Copyright Clearance Center.

License Number	5504331115027
License date	Mar 08, 2023
Licensed Content Publisher	Springer Nature
Licensed Content Publication	Journal of Nuclear Cardiology
Licensed Content Title	Incremental value of left ventricular shape parameters measured by gated SPECT MPI in predicting the super-response to CRT
Licensed Content Author	Zhuo He BS et al
Licensed Content Date	Jan 27, 2021
Type of Use	Thesis/Dissertation
Requestor type	academic/university or research institute
Format	print and electronic
Portion	full article/chapter
Will you be translating?	no
Circulation/distribution	1 - 29
Author of this Springer Nature content	yes
Title	Knowledge discovery on the integrative analysis of electrical and mechanical dyssynchrony to improve cardiac resynchronization therapy
Institution name	Michigan Technological University
Expected presentation date	Apr 2023
Requestor Location	Zhuo He 1809 Woodmar Dr HOUGHTON, MI 49931 United States Attn: Zhuo He
Total	**0.00 USD**

Terms and Conditions

Springer Nature Customer Service Centre GmbH Terms and Conditions

The following terms and conditions ("Terms and Conditions") together with the terms specified in your [RightsLink] constitute the License ("License") between you as Licensee and Springer Nature Customer Service Centre GmbH as Licensor. By clicking 'accept' and completing the transaction for your use of the material ("Licensed Material"), you confirm your acceptance of and obligation to be bound by these Terms and Conditions.

1. Grant and Scope of License

1. 1. The Licensor grants you a personal, non-exclusive, non-transferable, non-sublicensable, revocable, world-wide License to reproduce, distribute, communicate to the public, make available, broadcast, electronically transmit or create derivative works using the Licensed Material for the purpose(s) specified in your RightsLink Licence Details only. Licenses are granted for the specific use requested in the order and for no other use, subject to these Terms and Conditions. You acknowledge and agree that the rights granted to you under this License do not include the right to modify, edit, translate, include in collective works, or create derivative works of the Licensed Material in whole or in part unless expressly stated in your RightsLink Licence Details. You may use the Licensed Material only as permitted under this Agreement and will not reproduce, distribute, display, perform, or otherwise use or exploit any Licensed Material in any way, in whole or in part, except as expressly permitted by this License.

1. 2. You may only use the Licensed Content in the manner and to the extent permitted by these Terms and Conditions, by your RightsLink Licence Details and by any applicable laws.

1. 3. A separate license may be required for any additional use of the Licensed Material, e.g. where a license has been purchased for print use only, separate permission must be obtained for electronic re-use. Similarly, a License is only valid in the language selected and does not apply for editions in other languages unless additional translation rights have been granted separately in the License.

1. 4. Any content within the Licensed Material that is owned by third parties is expressly excluded from the License.

1. 5. Rights for additional reuses such as custom editions, computer/mobile applications, film or TV reuses and/or any other derivative rights requests require additional permission and may be subject to an additional fee. Please apply to journalpermissions@springernature.com or bookpermissions@springernature.com for these rights.

2. Reservation of Rights

Licensor reserves all rights not expressly granted to you under this License. You acknowledge and agree that nothing in this License limits or restricts Licensor's rights in or use of the Licensed Material in any way. Neither this License, nor any act, omission, or statement by Licensor or you, conveys any ownership right to you in any Licensed Material, or to any element or portion thereof. As between Licensor and you, Licensor owns and retains all right, title, and interest in and to the Licensed Material subject to the license granted in Section 1.1. Your permission to use the Licensed Material is expressly conditioned on you not impairing Licensor's or the applicable copyright owner's rights in the Licensed Material in any way.

3. Restrictions on use

3. 1. Minor editing privileges are allowed for adaptations for stylistic purposes or formatting purposes provided such alterations do not alter the original meaning or intention of the Licensed Material and the new figure(s) are still accurate and representative of the Licensed Material. Any other changes including but not limited to, cropping, adapting, and/or omitting material that affect the meaning, intention or moral rights of the author(s) are strictly prohibited.

3. 2. You must not use any Licensed Material as part of any design or trademark.

3. 3. Licensed Material may be used in Open Access Publications (OAP), but any such reuse must include a clear acknowledgment of this permission visible at the same time as the figures/tables/illustration or abstract and which must indicate that the Licensed Material is not part of the governing OA license but has been reproduced with permission. This may be indicated according to any standard referencing system but must include at a minimum 'Book/Journal title, Author, Journal Name (if applicable), Volume (if applicable), Publisher, Year, reproduced with permission from SNCSC'.

4. STM Permission Guidelines

4. 1. An alternative scope of license may apply to signatories of the STM Permissions Guidelines ("STM PG") as amended from time to time and made available at https://www.stm-assoc.org/intellectual-property/permissions/permissions-guidelines/.

4. 2. For content reuse requests that qualify for permission under the STM PG, and which may be updated from time to time, the STM PG supersede the terms and conditions contained in this License.

4. 3. If a License has been granted under the STM PG, but the STM PG no longer apply at the time of publication, further permission must be sought from the Rightsholder. Contact journalpermissions@springernature.com or bookpermissions@springernature.com for these rights.

5. Duration of License

5. 1. Unless otherwise indicated on your License, a License is valid from the date of purchase ("License Date") until the end of the relevant period in the below table:

Reuse in a medical communications project	Reuse up to distribution or time period indicated in License
Reuse in a dissertation/thesis	Lifetime of thesis
Reuse in a journal/magazine	Lifetime of journal/magazine
Reuse in a book/textbook	Lifetime of edition
Reuse on a website	1 year unless otherwise specified in the License
Reuse in a presentation/slide kit/poster	Lifetime of presentation/slide kit/poster. Note: publication whether electronic or in print of presentation/slide kit/poster may require further permission.
Reuse in conference proceedings	Lifetime of conference proceedings
Reuse in an annual report	Lifetime of annual report
Reuse in training/CME materials	Reuse up to distribution or time period indicated in License
Reuse in newsmedia	Lifetime of newsmedia
Reuse in coursepack/classroom materials	Reuse up to distribution and/or time period indicated in license

6. Acknowledgement

6. 1. The Licensor's permission must be acknowledged next to the Licensed Material in print. In electronic form, this acknowledgement must be visible at the same time as the figures/tables/illustrations or abstract and must be hyperlinked to the journal/book's homepage.

6. 2. Acknowledgement may be provided according to any standard referencing system and at a minimum should include "Author, Article/Book Title, Journal name/Book imprint, volume, page number, year, Springer Nature".

7. Reuse in a dissertation or thesis

7. 1. Where 'reuse in a dissertation/thesis' has been selected, the following terms apply: Print rights of the Version of Record are provided for; electronic rights for use only on institutional repository as defined by the Sherpa guideline (www.sherpa.ac.uk/romeo/) and only up to what is required by the awarding institution.

7. 2. For theses published under an ISBN or ISSN, separate permission is required. Please contact journalpermissions@springernature.com or bookpermissions@springernature.com for these rights.

7. 3. Authors must properly cite the published manuscript in their thesis according to current citation standards and include the following acknowledgement: '*Reproduced with permission from Springer Nature*'.

8. License Fee

You must pay the fee set forth in the License Agreement (the "License Fees"). All amounts payable by you under this License are exclusive of any sales, use, withholding, value added or similar taxes, government fees or levies or other assessments. Collection and/or remittance of such taxes to the relevant tax authority shall be the responsibility of the party who has the legal obligation to do so.

9. Warranty

9. 1. The Licensor warrants that it has, to the best of its knowledge, the rights to license reuse of the Licensed Material. **You are solely responsible for ensuring that the material you wish to license is original to the Licensor and does not carry the copyright of another entity or third party (as credited in the published version).** If the credit line on any part of the Licensed Material indicates that it was reprinted or adapted with permission from another source, then you should seek additional permission from that source to reuse the material.

9. 2. EXCEPT FOR THE EXPRESS WARRANTY STATED HEREIN AND TO THE EXTENT PERMITTED BY APPLICABLE LAW, LICENSOR PROVIDES THE LICENSED MATERIAL "AS IS" AND MAKES NO OTHER REPRESENTATION OR WARRANTY. LICENSOR EXPRESSLY DISCLAIMS ANY LIABILITY FOR ANY CLAIM ARISING FROM OR OUT OF THE CONTENT, INCLUDING BUT NOT LIMITED TO ANY ERRORS, INACCURACIES, OMISSIONS, OR DEFECTS CONTAINED THEREIN, AND ANY IMPLIED OR EXPRESS WARRANTY AS TO MERCHANTABILITY OR FITNESS FOR A PARTICULAR PURPOSE. IN NO EVENT SHALL LICENSOR BE LIABLE TO YOU OR ANY OTHER PARTY OR ANY OTHER PERSON OR FOR ANY SPECIAL, CONSEQUENTIAL, INCIDENTAL, INDIRECT, PUNITIVE, OR EXEMPLARY DAMAGES, HOWEVER CAUSED, ARISING OUT OF OR IN CONNECTION WITH THE DOWNLOADING, VIEWING OR USE OF THE LICENSED MATERIAL REGARDLESS OF THE FORM OF ACTION, WHETHER FOR BREACH OF CONTRACT, BREACH OF WARRANTY, TORT, NEGLIGENCE, INFRINGEMENT OR OTHERWISE (INCLUDING, WITHOUT LIMITATION, DAMAGES BASED ON LOSS OF PROFITS, DATA, FILES, USE, BUSINESS OPPORTUNITY OR CLAIMS OF THIRD PARTIES), AND WHETHER OR NOT THE PARTY HAS BEEN ADVISED OF THE POSSIBILITY OF SUCH DAMAGES. THIS LIMITATION APPLIES NOTWITHSTANDING ANY FAILURE OF ESSENTIAL PURPOSE OF ANY LIMITED REMEDY PROVIDED HEREIN.

10. Termination and Cancellation

10. 1. The License and all rights granted hereunder will continue until the end of the applicable period shown in Clause 5.1 above. Thereafter, this license will be terminated and all rights granted hereunder will cease.

10. 2. Licensor reserves the right to terminate the License in the event that payment is not received in full or if you breach the terms of this License.

11. General

11. 1. The License and the rights and obligations of the parties hereto shall be construed, interpreted and determined in accordance with the laws of the Federal Republic of Germany without reference to the stipulations of the CISG (United Nations Convention on Contracts for the International Sale of Goods) or to Germany´s choice-of-law principle.

11. 2. The parties acknowledge and agree that any controversies and disputes arising out of this License shall be decided exclusively by the courts of or having jurisdiction for Heidelberg, Germany, as far as legally permissible.

11. 3. This License is solely for Licensor's and Licensee's benefit. It is not for the benefit of any other person or entity.

Questions? For questions on Copyright Clearance Center accounts or website issues please contact springernaturesupport@copyright.com or +1-855-239-3415 (toll free in the US) or +1-978-646-2777. For questions on Springer Nature licensing please visit https://www.springernature.com/gp/partners/rights-permissions-third-party-distribution

Other Conditions:

Version 1.4 - Dec 2022

Questions? E-mail us at customercare@copyright.com.

SPRINGER NATURE LICENSE
TERMS AND CONDITIONS

Mar 08, 2023

This Agreement between Zhuo He ("You") and Springer Nature ("Springer Nature") consists of your license details and the terms and conditions provided by Springer Nature and Copyright Clearance Center.

License Number	5504380860364
License date	Mar 08, 2023
Licensed Content Publisher	Springer Nature
Licensed Content Publication	Journal of Nuclear Cardiology
Licensed Content Title	Predictive values of left ventricular mechanical dyssynchrony for CRT response in heart failure patients with different pathophysiology
Licensed Content Author	Zhuo He BS et al
Licensed Content Date	Sep 17, 2021
Type of Use	Thesis/Dissertation
Requestor type	academic/university or research institute
Format	print and electronic
Portion	full article/chapter
Will you be translating?	no

Circulation/distribution	1 - 29
Author of this Springer Nature content	yes
Title	Knowledge discovery on the integrative analysis of electrical and mechanical dyssynchrony to improve cardiac resynchronization therapy
Institution name	Michigan Technological University
Expected presentation date	Apr 2023
Requestor Location	Zhuo He 1400 Townsend Dr HOUGHTON, MI 49931 United States Attn: Zhuo He
Total	0.00 USD

Terms and Conditions

Springer Nature Customer Service Centre GmbH Terms and Conditions

The following terms and conditions ("Terms and Conditions") together with the terms specified in your [RightsLink] constitute the License ("License") between you as Licensee and Springer Nature Customer Service Centre GmbH as Licensor. By clicking 'accept' and completing the transaction for your use of the material ("Licensed Material"), you confirm your acceptance of and obligation to be bound by these Terms and Conditions.

1. Grant and Scope of License

1. 1. The Licensor grants you a personal, non-exclusive, non-transferable, non-sublicensable, revocable, world-wide License to reproduce, distribute, communicate to the public, make available, broadcast, electronically transmit or create derivative works using the Licensed Material for the purpose(s) specified in your RightsLink Licence Details only. Licenses are granted for the specific use requested in the order and for no other use, subject to these Terms and Conditions. You acknowledge and agree that the rights granted to you under this License do not include the right to modify, edit, translate, include in collective works, or create derivative works of the Licensed Material in whole or in part unless expressly stated in your RightsLink

Licence Details. You may use the Licensed Material only as permitted under this Agreement and will not reproduce, distribute, display, perform, or otherwise use or exploit any Licensed Material in any way, in whole or in part, except as expressly permitted by this License.

1. 2. You may only use the Licensed Content in the manner and to the extent permitted by these Terms and Conditions, by your RightsLink Licence Details and by any applicable laws.

1. 3. A separate license may be required for any additional use of the Licensed Material, e.g. where a license has been purchased for print use only, separate permission must be obtained for electronic re-use. Similarly, a License is only valid in the language selected and does not apply for editions in other languages unless additional translation rights have been granted separately in the License.

1. 4. Any content within the Licensed Material that is owned by third parties is expressly excluded from the License.

1. 5. Rights for additional reuses such as custom editions, computer/mobile applications, film or TV reuses and/or any other derivative rights requests require additional permission and may be subject to an additional fee. Please apply to journalpermissions@springernature.com or bookpermissions@springernature.com for these rights.

2. Reservation of Rights

Licensor reserves all rights not expressly granted to you under this License. You acknowledge and agree that nothing in this License limits or restricts Licensor's rights in or use of the Licensed Material in any way. Neither this License, nor any act, omission, or statement by Licensor or you, conveys any ownership right to you in any Licensed Material, or to any element or portion thereof. As between Licensor and you, Licensor owns and retains all right, title, and interest in and to the Licensed Material subject to the license granted in Section 1.1. Your permission to use the Licensed Material is expressly conditioned on you not impairing Licensor's or the applicable copyright owner's rights in the Licensed Material in any way.

3. Restrictions on use

3. 1. Minor editing privileges are allowed for adaptations for stylistic purposes or formatting purposes provided such alterations do not alter the original meaning or intention of the Licensed Material and the new figure(s) are still accurate and representative of the Licensed Material. Any other changes including but not limited to, cropping, adapting, and/or omitting material that affect the meaning, intention or moral rights of the author(s) are strictly prohibited.

3. 2. You must not use any Licensed Material as part of any design or trademark.

3. 3. Licensed Material may be used in Open Access Publications (OAP), but any such reuse must include a clear acknowledgment of this permission visible at the same time as the figures/tables/illustration or abstract and which must indicate that the Licensed Material is not part of the governing OA license but has been reproduced with permission. This may be indicated according to any standard referencing system but must include at a minimum 'Book/Journal title, Author, Journal Name (if applicable),

Volume (if applicable), Publisher, Year, reproduced with permission from SNCSC'.

4. STM Permission Guidelines

4. 1. An alternative scope of license may apply to signatories of the STM Permissions Guidelines ("STM PG") as amended from time to time and made available at https://www.stm-assoc.org/intellectual-property/permissions/permissions-guidelines/.

4. 2. For content reuse requests that qualify for permission under the STM PG, and which may be updated from time to time, the STM PG supersede the terms and conditions contained in this License.

4. 3. If a License has been granted under the STM PG, but the STM PG no longer apply at the time of publication, further permission must be sought from the Rightsholder. Contact journalpermissions@springernature.com or bookpermissions@springernature.com for these rights.

5. Duration of License

5. 1. Unless otherwise indicated on your License, a License is valid from the date of purchase ("License Date") until the end of the relevant period in the below table:

Reuse in a medical communications project	Reuse up to distribution or time period indicated in License
Reuse in a dissertation/thesis	Lifetime of thesis
Reuse in a journal/magazine	Lifetime of journal/magazine
Reuse in a book/textbook	Lifetime of edition
Reuse on a website	1 year unless otherwise specified in the License
Reuse in a presentation/slide kit/poster	Lifetime of presentation/slide kit/poster. Note: publication whether electronic or in print of presentation/slide kit/poster may require further permission.
Reuse in conference proceedings	Lifetime of conference proceedings
Reuse in an annual report	Lifetime of annual report
Reuse in training/CME materials	Reuse up to distribution or time period indicated in License
Reuse in newsmedia	Lifetime of newsmedia
Reuse in coursepack/classroom materials	Reuse up to distribution and/or time period indicated in license

6. Acknowledgement

6. 1. The Licensor's permission must be acknowledged next to the Licensed Material in print. In electronic form, this acknowledgement must be visible at the same time as the figures/tables/illustrations or abstract and must be hyperlinked to the journal/book's homepage.

6. 2. Acknowledgement may be provided according to any standard referencing system and at a minimum should include "Author, Article/Book Title, Journal name/Book imprint, volume, page number, year, Springer Nature".

7. Reuse in a dissertation or thesis

7. 1. Where 'reuse in a dissertation/thesis' has been selected, the following terms apply: Print rights of the Version of Record are provided for; electronic rights for use only on institutional repository as defined by the Sherpa guideline (www.sherpa.ac.uk/romeo/) and only up to what is required by the awarding institution.

7. 2. For theses published under an ISBN or ISSN, separate permission is required. Please contact journalpermissions@springernature.com or bookpermissions@springernature.com for these rights.

7. 3. Authors must properly cite the published manuscript in their thesis according to current citation standards and include the following acknowledgement: '*Reproduced with permission from Springer Nature*'.

8. License Fee

You must pay the fee set forth in the License Agreement (the "License Fees"). All amounts payable by you under this License are exclusive of any sales, use, withholding, value added or similar taxes, government fees or levies or other assessments. Collection and/or remittance of such taxes to the relevant tax authority shall be the responsibility of the party who has the legal obligation to do so.

9. Warranty

9. 1. The Licensor warrants that it has, to the best of its knowledge, the rights to license reuse of the Licensed Material. **You are solely responsible for ensuring that the material you wish to license is original to the Licensor and does not carry the copyright of another entity or third party (as credited in the published version).** If the credit line on any part of the Licensed Material indicates that it was reprinted or adapted with permission from another source, then you should seek additional permission from that source to reuse the material.

9. 2. EXCEPT FOR THE EXPRESS WARRANTY STATED HEREIN AND TO THE EXTENT PERMITTED BY APPLICABLE LAW, LICENSOR PROVIDES THE LICENSED MATERIAL "AS IS" AND MAKES NO OTHER REPRESENTATION OR WARRANTY. LICENSOR EXPRESSLY DISCLAIMS ANY LIABILITY FOR ANY CLAIM ARISING FROM OR OUT OF THE CONTENT, INCLUDING BUT NOT LIMITED TO ANY ERRORS, INACCURACIES, OMISSIONS, OR DEFECTS CONTAINED THEREIN, AND ANY IMPLIED OR EXPRESS WARRANTY AS TO MERCHANTABILITY OR FITNESS FOR A PARTICULAR PURPOSE. IN NO EVENT SHALL LICENSOR BE LIABLE TO YOU OR ANY OTHER PARTY OR ANY OTHER PERSON OR FOR ANY SPECIAL, CONSEQUENTIAL, INCIDENTAL, INDIRECT, PUNITIVE, OR EXEMPLARY DAMAGES, HOWEVER CAUSED, ARISING OUT OF OR IN CONNECTION WITH THE DOWNLOADING, VIEWING OR USE OF THE LICENSED MATERIAL REGARDLESS OF THE FORM OF ACTION, WHETHER FOR BREACH OF CONTRACT, BREACH OF WARRANTY, TORT, NEGLIGENCE, INFRINGEMENT OR OTHERWISE (INCLUDING, WITHOUT LIMITATION,

DAMAGES BASED ON LOSS OF PROFITS, DATA, FILES, USE, BUSINESS OPPORTUNITY OR CLAIMS OF THIRD PARTIES), AND WHETHER OR NOT THE PARTY HAS BEEN ADVISED OF THE POSSIBILITY OF SUCH DAMAGES. THIS LIMITATION APPLIES NOTWITHSTANDING ANY FAILURE OF ESSENTIAL PURPOSE OF ANY LIMITED REMEDY PROVIDED HEREIN.

10. Termination and Cancellation

10. 1. The License and all rights granted hereunder will continue until the end of the applicable period shown in Clause 5.1 above. Thereafter, this license will be terminated and all rights granted hereunder will cease.

10. 2. Licensor reserves the right to terminate the License in the event that payment is not received in full or if you breach the terms of this License.

11. General

11. 1. The License and the rights and obligations of the parties hereto shall be construed, interpreted and determined in accordance with the laws of the Federal Republic of Germany without reference to the stipulations of the CISG (United Nations Convention on Contracts for the International Sale of Goods) or to Germany's choice-of-law principle.

11. 2. The parties acknowledge and agree that any controversies and disputes arising out of this License shall be decided exclusively by the courts of or having jurisdiction for Heidelberg, Germany, as far as legally permissible.

11. 3. This License is solely for Licensor's and Licensee's benefit. It is not for the benefit of any other person or entity.

Questions? For questions on Copyright Clearance Center accounts or website issues please contact springernaturesupport@copyright.com or +1-855-239-3415 (toll free in the US) or +1-978-646-2777. For questions on Springer Nature licensing please visit https://www.springernature.com/gp/partners/rights-permissions-third-party-distribution

Other Conditions:

Version 1.4 - Dec 2022

Questions? customercare@copyright.com.

SPRINGER NATURE LICENSE
TERMS AND CONDITIONS

Mar 08, 2023

This Agreement between Zhuo He ("You") and Springer Nature ("Springer Nature") consists of your license details and the terms and conditions provided by Springer Nature and Copyright Clearance Center.

License Number	5504380913281
License date	Mar 08, 2023
Licensed Content Publisher	Springer Nature
Licensed Content Publication	Journal of Nuclear Cardiology
Licensed Content Title	A method using deep learning to discover new predictors from left-ventricular mechanical dyssynchrony for CRT response
Licensed Content Author	Zhuo He BS et al
Licensed Content Date	Aug 1, 2022
Type of Use	Thesis/Dissertation
Requestor type	academic/university or research institute
Format	print and electronic
Portion	full article/chapter
Will you be translating?	no

Circulation/distribution	1 - 29
Author of this Springer Nature content	yes
Title	Knowledge discovery on the integrative analysis of electrical and mechanical dyssynchrony to improve cardiac resynchronization therapy
Institution name	Michigan Technological University
Expected presentation date	Apr 2023
Requestor Location	Zhuo He 1400 Townsend Dr HOUGHTON, MI 49931 United States Attn: Zhuo He
Total	0.00 USD

Terms and Conditions

Springer Nature Customer Service Centre GmbH Terms and Conditions

The following terms and conditions ("Terms and Conditions") together with the terms specified in your [RightsLink] constitute the License ("License") between you as Licensee and Springer Nature Customer Service Centre GmbH as Licensor. By clicking 'accept' and completing the transaction for your use of the material ("Licensed Material"), you confirm your acceptance of and obligation to be bound by these Terms and Conditions.

1. Grant and Scope of License

1. 1. The Licensor grants you a personal, non-exclusive, non-transferable, non-sublicensable, revocable, world-wide License to reproduce, distribute, communicate to the public, make available, broadcast, electronically transmit or create derivative works using the Licensed Material for the purpose(s) specified in your RightsLink Licence Details only. Licenses are granted for the specific use requested in the order and for no other use, subject to these Terms and Conditions. You acknowledge and agree that the rights granted to you under this License do not include the right to modify, edit, translate, include in collective works, or create derivative works of the Licensed Material in whole or in part unless expressly stated in your RightsLink

Licence Details. You may use the Licensed Material only as permitted under this Agreement and will not reproduce, distribute, display, perform, or otherwise use or exploit any Licensed Material in any way, in whole or in part, except as expressly permitted by this License.

1. 2. You may only use the Licensed Content in the manner and to the extent permitted by these Terms and Conditions, by your RightsLink Licence Details and by any applicable laws.

1. 3. A separate license may be required for any additional use of the Licensed Material, e.g. where a license has been purchased for print use only, separate permission must be obtained for electronic re-use. Similarly, a License is only valid in the language selected and does not apply for editions in other languages unless additional translation rights have been granted separately in the License.

1. 4. Any content within the Licensed Material that is owned by third parties is expressly excluded from the License.

1. 5. Rights for additional reuses such as custom editions, computer/mobile applications, film or TV reuses and/or any other derivative rights requests require additional permission and may be subject to an additional fee. Please apply to journalpermissions@springernature.com or bookpermissions@springernature.com for these rights.

2. Reservation of Rights

Licensor reserves all rights not expressly granted to you under this License. You acknowledge and agree that nothing in this License limits or restricts Licensor's rights in or use of the Licensed Material in any way. Neither this License, nor any act, omission, or statement by Licensor or you, conveys any ownership right to you in any Licensed Material, or to any element or portion thereof. As between Licensor and you, Licensor owns and retains all right, title, and interest in and to the Licensed Material subject to the license granted in Section 1.1. Your permission to use the Licensed Material is expressly conditioned on you not impairing Licensor's or the applicable copyright owner's rights in the Licensed Material in any way.

3. Restrictions on use

3. 1. Minor editing privileges are allowed for adaptations for stylistic purposes or formatting purposes provided such alterations do not alter the original meaning or intention of the Licensed Material and the new figure(s) are still accurate and representative of the Licensed Material. Any other changes including but not limited to, cropping, adapting, and/or omitting material that affect the meaning, intention or moral rights of the author(s) are strictly prohibited.

3. 2. You must not use any Licensed Material as part of any design or trademark.

3. 3. Licensed Material may be used in Open Access Publications (OAP), but any such reuse must include a clear acknowledgment of this permission visible at the same time as the figures/tables/illustration or abstract and which must indicate that the Licensed Material is not part of the governing OA license but has been reproduced with permission. This may be indicated according to any standard referencing system but must include at a minimum 'Book/Journal title, Author, Journal Name (if applicable),

Volume (if applicable), Publisher, Year, reproduced with permission from SNCSC'.

4. STM Permission Guidelines

4. 1. An alternative scope of license may apply to signatories of the STM Permissions Guidelines ("STM PG") as amended from time to time and made available at https://www.stm-assoc.org/intellectual-property/permissions/permissions-guidelines/.

4. 2. For content reuse requests that qualify for permission under the STM PG, and which may be updated from time to time, the STM PG supersede the terms and conditions contained in this License.

4. 3. If a License has been granted under the STM PG, but the STM PG no longer apply at the time of publication, further permission must be sought from the Rightsholder. Contact journalpermissions@springernature.com or bookpermissions@springernature.com for these rights.

5. Duration of License

5. 1. Unless otherwise indicated on your License, a License is valid from the date of purchase ("License Date") until the end of the relevant period in the below table:

Reuse in a medical communications project	Reuse up to distribution or time period indicated in License
Reuse in a dissertation/thesis	Lifetime of thesis
Reuse in a journal/magazine	Lifetime of journal/magazine
Reuse in a book/textbook	Lifetime of edition
Reuse on a website	1 year unless otherwise specified in the License
Reuse in a presentation/slide kit/poster	Lifetime of presentation/slide kit/poster. Note: publication whether electronic or in print of presentation/slide kit/poster may require further permission.
Reuse in conference proceedings	Lifetime of conference proceedings
Reuse in an annual report	Lifetime of annual report
Reuse in training/CME materials	Reuse up to distribution or time period indicated in License
Reuse in newsmedia	Lifetime of newsmedia
Reuse in coursepack/classroom materials	Reuse up to distribution and/or time period indicated in license

6. Acknowledgement

6. 1. The Licensor's permission must be acknowledged next to the Licensed Material in print. In electronic form, this acknowledgement must be visible at the same time as the figures/tables/illustrations or abstract and must be hyperlinked to the journal/book's homepage.

6. 2. Acknowledgement may be provided according to any standard referencing system and at a minimum should include "Author, Article/Book Title, Journal name/Book imprint, volume, page number, year, Springer Nature".

7. Reuse in a dissertation or thesis

7. 1. Where 'reuse in a dissertation/thesis' has been selected, the following terms apply: Print rights of the Version of Record are provided for; electronic rights for use only on institutional repository as defined by the Sherpa guideline (www.sherpa.ac.uk/romeo/) and only up to what is required by the awarding institution.

7. 2. For theses published under an ISBN or ISSN, separate permission is required. Please contact journalpermissions@springernature.com or bookpermissions@springernature.com for these rights.

7. 3. Authors must properly cite the published manuscript in their thesis according to current citation standards and include the following acknowledgement: '*Reproduced with permission from Springer Nature*'.

8. License Fee

You must pay the fee set forth in the License Agreement (the "License Fees"). All amounts payable by you under this License are exclusive of any sales, use, withholding, value added or similar taxes, government fees or levies or other assessments. Collection and/or remittance of such taxes to the relevant tax authority shall be the responsibility of the party who has the legal obligation to do so.

9. Warranty

9. 1. The Licensor warrants that it has, to the best of its knowledge, the rights to license reuse of the Licensed Material. **You are solely responsible for ensuring that the material you wish to license is original to the Licensor and does not carry the copyright of another entity or third party (as credited in the published version).** If the credit line on any part of the Licensed Material indicates that it was reprinted or adapted with permission from another source, then you should seek additional permission from that source to reuse the material.

9. 2. EXCEPT FOR THE EXPRESS WARRANTY STATED HEREIN AND TO THE EXTENT PERMITTED BY APPLICABLE LAW, LICENSOR PROVIDES THE LICENSED MATERIAL "AS IS" AND MAKES NO OTHER REPRESENTATION OR WARRANTY. LICENSOR EXPRESSLY DISCLAIMS ANY LIABILITY FOR ANY CLAIM ARISING FROM OR OUT OF THE CONTENT, INCLUDING BUT NOT LIMITED TO ANY ERRORS, INACCURACIES, OMISSIONS, OR DEFECTS CONTAINED THEREIN, AND ANY IMPLIED OR EXPRESS WARRANTY AS TO MERCHANTABILITY OR FITNESS FOR A PARTICULAR PURPOSE. IN NO EVENT SHALL LICENSOR BE LIABLE TO YOU OR ANY OTHER PARTY OR ANY OTHER PERSON OR FOR ANY SPECIAL, CONSEQUENTIAL, INCIDENTAL, INDIRECT, PUNITIVE, OR EXEMPLARY DAMAGES, HOWEVER CAUSED, ARISING OUT OF OR IN CONNECTION WITH THE DOWNLOADING, VIEWING OR USE OF THE LICENSED MATERIAL REGARDLESS OF THE FORM OF ACTION, WHETHER FOR BREACH OF CONTRACT, BREACH OF WARRANTY, TORT, NEGLIGENCE, INFRINGEMENT OR OTHERWISE (INCLUDING, WITHOUT LIMITATION,

DAMAGES BASED ON LOSS OF PROFITS, DATA, FILES, USE, BUSINESS OPPORTUNITY OR CLAIMS OF THIRD PARTIES), AND WHETHER OR NOT THE PARTY HAS BEEN ADVISED OF THE POSSIBILITY OF SUCH DAMAGES. THIS LIMITATION APPLIES NOTWITHSTANDING ANY FAILURE OF ESSENTIAL PURPOSE OF ANY LIMITED REMEDY PROVIDED HEREIN.

10. Termination and Cancellation

10. 1. The License and all rights granted hereunder will continue until the end of the applicable period shown in Clause 5.1 above. Thereafter, this license will be terminated and all rights granted hereunder will cease.

10. 2. Licensor reserves the right to terminate the License in the event that payment is not received in full or if you breach the terms of this License.

11. General

11. 1. The License and the rights and obligations of the parties hereto shall be construed, interpreted and determined in accordance with the laws of the Federal Republic of Germany without reference to the stipulations of the CISG (United Nations Convention on Contracts for the International Sale of Goods) or to Germany's choice-of-law principle.

11. 2. The parties acknowledge and agree that any controversies and disputes arising out of this License shall be decided exclusively by the courts of or having jurisdiction for Heidelberg, Germany, as far as legally permissible.

11. 3. This License is solely for Licensor's and Licensee's benefit. It is not for the benefit of any other person or entity.

Questions? For questions on Copyright Clearance Center accounts or website issues please contact springernaturesupport@copyright.com or +1-855-239-3415 (toll free in the US) or +1-978-646-2777. For questions on Springer Nature licensing please visit https://www.springernature.com/gp/partners/rights-permissions-third-party-distribution

Other Conditions:

Version 1.4 - Dec 2022

Questions? customercare@copyright.com.